FLEXURAL STRENGTHENING OF TIMBER BRIDGE BEAMS USING FRP

by

Christopher J. Gentile

A Thesis
Submitted to the Faculty of Graduate Studies
In Partial Fulfillment of the
Requirements for the Degree of

MASTER OF SCIENCE

Structural Engineering Division
Department of Civil & Geological Engineering
University of Manitoba
Winnipeg, Manitoba
Canada

National Library
of Canada

Acquisitions and
Bibliographic Services

395 Wellington Street
Ottawa ON K1A 0N4
Canada

Bibliothèque nationale
du Canada

Acquisitions et
services bibliographiques

395, rue Wellington
Ottawa ON K1A 0N4
Canada

Your file Votre référence

Our file Notre référence

0-612-51711-X

Canada

THE UNIVERSITY OF MANITOBA

FACULTY OF GRADUATE STUDIES

*****

COPYRIGHT PERMISSION PAGE

Flexural Strengthening of Timber Bridge Beams Using FRP

BY

Christopher J. Gentile

A Thesis/Practicum submitted to the Faculty of Graduate Studies of The University of Manitoba in partial fulfillment of the requirements of the degree

of

Master of Science

ABSTRACT

Repair and rehabilitation of infrastructure is becoming increasingly important for bridges due to material deterioration and limited capacity to accommodate modern load levels. The demand for using increasingly heavier truck loads is forcing bridge owners to upgrade existing structures. The Province of Manitoba has an inventory of approximately 2000 timber bridges that require strengthening to support the current maximum design loads.

An experimental program was undertaken at the University of Manitoba to study the flexural behaviour of creosote-treated sawn Douglas Fir timber beams strengthened by glass fibre reinforced polymer (GFRP) bars. Twenty-two half-scale beams and four full-scale timber stringers were tested to failure using three GFRP reinforcement ratios between 0.27 and 0.82 percent and plain timber beams as control beams. The flexural behaviour is examined in terms of mode of failure, load-deflection, strain distribution, and ultimate strength. Based on the experimental results, an analytical model is proposed to predict the flexural capacity of plain and reinforced timber. The proposed strengthening technique has shown that the failure mode will change from brittle tension to a more ductile compression-initiated failure and that the flexural strength may be increased by 18 to 46 percent. The GFRP bars bridged local defects in the timber and allowed the timber to support higher nominal stresses before failure.

ACKNOWLEDGEMENTS

The author would like to express his sincere gratitude and appreciation to Dr. Sami Rizkalla. His continual encouragement, enthusiasm, and generosity in terms of time, resources, and opportunity have made this work possible. The author is extremely grateful for the opportunity to work with and learn from Dr. Rizkalla.

The support provided by the Natural Sciences and Engineering Research Council of Canada and the ISIS Canada Network of Centres of Excellence on Intelligent Sensing for Innovative Structures is gratefully acknowledged. Sincere thanks are extended to the Manitoba Department of Highways and Government Services and Concrete Restoration Services, Ltd. for their support.

The author would like to express his appreciation to Dr. Dagmar Svecova, Mr. Walter Saltzberg, and Dr. Ken Johns for their experience and knowledge during the research. Special thanks is extended to Mr. Moray McVey for his invaluable technical assistance and during the experimental work. The assistance of Ms. Carolina Madrid and Mr. Mina Dawood is also gratefully acknowledged.

Finally, the author wishes to thank his parents and sister for their continual and unconditional support.

TABLE OF CONTENTS

CHAPTER 3 EXPERIMENTAL PROGRAM

CHAPTER 4 EXPERIMENTAL RESULTS AND ANALYSIS

CHAPTER 5 ANALYTICAL MODELS FOR BENDING STRENGTH OF PLAIN AND REINFORCED TIMBER

LIST OF TABLES

CHAPTER 3

CHAPTER 4

CHAPTER 5

LIST OF FIGURES

CHAPTER 2

CHAPTER 3

CHAPTER 4

CHAPTER 5

LIST OF SYMBOLS

a	distance from the support to point of applied load
a_1	distance between symmetrically placed loads
A_{GF}	cross-sectional area of GFRP
b	width of section
c	distance from extreme tension fibre to neutral axis as a ratio of the depth d
d	depth of section
E	modulus of elasticity
E_{GF}	modulus of elasticity of GFRP
E_w	modulus of elasticity of timber
EI	bending stiffness
f_c	extreme fibre compressive stress
f_{cu}	maximum compression strength
f_m	extreme fibre tensile strength in bending
f_t	extreme fibre tensile stress
f_{tu}	ultimate tensile strength
I_g	moment of inertia of gross cross-section
I_T	moment of inertia of transformed section
k	shape parameter in Weibull distribution
k_1	length effect parameter
k_2	depth effect parameter
k_3	stress distribution parameter
L	span of the beam

L_e equivalent stressed length

m ratio of slope of descending branch of stress-strain curve to E_w

m_1 scale parameter in Weibull distribution

M_F bending moment at failure

MOE modulus of elasticity

MOR modulus of rupture

P total applied load

s distance from extreme tension fibre to centroid of FRP reinforcement as a fraction of the depth d

S_g section modulus of gross cross-section

UCS ultimate compression strength from CWC data

UTS ultimate tensile strength from CWC data

x strength in Weibull distribution

x_0 location parameter or minimum strength in Weibull distribution

α_m modification factor for extreme fibre tensile strength in bending

Δ deflection at mid-span

ε_c strain at extreme compression fibre

ε_{GF} strain in GFRP reinforcement

ε_t strain at extreme tension fibre

ε_y strain corresponding to maximum compressive strength f_{cu}

ρ_{GF} reinforcement ratio of GFRP

CHAPTER 1

INTRODUCTION

1.1 GENERAL

Repair and rehabilitation of infrastructure is becoming increasingly important for bridges due to material deterioration and limited capacity to accommodate modern load levels. The demand for using increasingly heavier truck loads is forcing bridge owners to upgrade existing structures. In recent years, there has been considerable research into the use of fibre-reinforced polymers (FRP) for the strengthening and repair of bridges. The advantages of FRP are its high strength-to-weight ratio and corrosion resistance, which make it an attractive replacement for steel in reinforced concrete structures. FRP has also been used to strengthen timber by adding a lamination of FRP into glue-laminated timber beams. The Province of Manitoba has an inventory of approximately 2000 timber bridges, many which have been in service for 40 plus years and require strengthening to support the current maximum design loads.

Due to a lack of information on the use of FRP for flexural strengthening of sawn timber beams, an experimental program has been undertaken at the University of Manitoba, to test scale models and actual timber bridge stringers strengthened with glass fibre-

reinforced polymer (GFRP) bars. Twenty-two half-scale beams and four full-scale timber stringers were tested to failure to determine the feasibility of the strengthening scheme. The effect of three different reinforcement ratios on the behaviour of the beams has been evaluated.

1.2 OBJECTIVES

The main objective of this research program is to propose a feasible solution for strengthening timber bridges. The experimental program was designed to investigate a specific flexural strengthening solution for timber bridges in the Province of Manitoba. The specific objectives of this investigation are:

1. To increase the flexural capacity of the timber stringers by at least 25 percent to support the current maximum legal truck loads specified by the Transportation Association of Canada (TAC).

2. To determine the effect of different reinforcement ratios of GFRP on the general behaviour and flexural capacity of reinforced timber beams.

3. To develop an analytical model to predict the flexural capacity of the reinforced timber.

1.3 SCOPE AND CONTENTS

This study consists of an experimental investigation and analytical modeling of sawn timber bridge stringers strengthened with GFRP bars installed in grooves cut into the timber. The study investigates the flexural behaviour of timber beams under static loading conditions. Investigation of shear behaviour and response to dynamic and impact loading is beyond the scope of this work. Fatigue performance of the reinforced beams and material durability of the GFRP are not included. Based on the results of half-scale and full-scale beam tests and analysis, an analytical model is proposed to predict the flexural capacity of plain and reinforced timber beams. The following is brief discussion of each phase of the study:

Experimental Investigation

Twenty-two beams were prepared that were a 1:2 scale model of typical timber bridge stringers. Seven of the half-scale beams were used as control beams and fifteen half-scale beams were reinforced with GFRP bars using three different reinforcement ratios. The beams were tested to failure to examine their behaviour and to determine the most efficient reinforcement ratio. In order to extend the applicability of the experimental results to typical timber bridge stringers, three full-scale stringers, taken from an old timber bridge, were reinforced using GFRP bars. A fourth full-scale stringer was used as an unreinforced control beam. All of the beams were tested to failure to determine the efficiency of the strengthening technique. Prior to the half-scale and full-scale beam tests, six small timber beams were reinforced with GFRP bars to qualitatively assess the performance of the bond between the creosote-treated timber, epoxy resin, and GFRP bars.

Analytical Modeling

This component of the study includes an analytical approach to predict the flexural capacity of plain and GFRP-reinforced timber beams. A bending strength model is calibrated using the results of the half-scale unreinforced timber beam tests. Based on the half-scale reinforced beam test results, the bending strength model is modified to account for the effect of the GFRP reinforcement. The proposed bending strength model is used to examine the effect of varying the GFRP reinforcement ratio.

An overview of the contents of the thesis is provided in the following:

Chapter 2 – The characteristics of FRP reinforcement, the structural behaviour of timber and a review of published studies of strengthening of timber structures are presented.

Chapter 3 – Details of the experimental program, which includes six bond specimens, twenty-two half-scale beam tests, and four full-scale beam tests, are provided.

Chapter 4 – Test results for the bond specimens and both sets of beam tests are presented. The behaviour of the beams is described in terms of mode of failure, load-deflection, strain distribution, and ultimate strength.

Chapter 5 – An analytical model for bending strength is calibrated for plain timber using the results from the half-scale beam tests. The model is modified to predict the strength

of the reinforced beams and the modified model is then used to examine the effect of varying the GFRP reinforcement ratio.

Chapter 6 – This chapter summarizes the research program, provides conclusions resulting from this study, and provides recommendations for further research.

CHAPTER 2

LITERATURE REVIEW

2.1 OVERVIEW

This chapter presents the general properties and applications of fibre-reinforced polymers (FRP) for timber bridges. The structural behaviour of timber is discussed with emphasis on the stress-strain relationship and size effects. The chapter concludes with a review of published studies of strengthening of timber structures.

2.2 FRP MATERIALS

FRP materials are a group of advanced composites consisting of high strength and high modulus fibres embedded in a matrix with distinct interface characteristics. Both fibres and matrix retain their physical and chemical identities, yet they produce distinct properties that cannot be achieved by either constituent acting alone. The matrix is the binder material of the composite and plays a significant role in transmitting the applied load to the fibres. The most common type of matrix is polymeric material, including epoxies and polyesters. Several types of fibres such as glass and carbon have been used

in structural applications. A more detailed discussion of fibre types is given in the next section.

2.2.1 Fibre Types

The three most common fibres used in structural applications are glass, aramid, and carbon. Glass fibres have high tensile strength combined with good mechanical properties, high chemical resistance, and excellent insulating properties. Some disadvantages of glass are low tensile modulus, sensitivity to abrasion, and reduced tensile strength in the presence of water and sustained loads due to creep rupture characteristics. The types of glass fibre commonly found in structural applications are E (electrical) and S (high strength).

Aramid fibres have the lowest specific gravity and the highest tensile strength-to-weight ratio of the main fibre types. In bending, aramid fibres exhibit a high degree of yielding on the compression side that is not observed in other fibres. This non-catastrophic failure mode gives aramid fibre composites superior damage tolerance to dynamic and impact loading. Some disadvantages of aramid are low compressive strength, difficulty in machining, and sensitivity to ultra-violet radiation. Aramid fibres are sold commercially under the trade names Kevlar and Twaron.

Carbon fibres have very high tensile strength, high elastic modulus, and high fatigue strength. The main advantages of carbon fibres are their high strength-to-weight ratios, excellent durability, and low relaxation under sustained load. Some disadvantages include low impact resistance and high cost. Due to their high cost, carbon fibres have

been used for very specific applications such as prestressing of structural members and flexural reinforcement of concrete structures.

2.2.2 Applications

In the past, the high cost of FRP materials had restricted their applications to areas where weight reduction was more important than cost, such as the aerospace and sporting goods industries. More recently, the need to upgrade and repair infrastructure has led to increased research and use of FRP materials in structural engineering applications. Neale and Labossière (1997) reviewed the state-of-the-art in Canada on strengthening existing structures using FRP materials and Triantafillou (1998) reviewed the basic concepts and applications of FRP materials for the strengthening of civil engineering structures, with emphasis on reinforced concrete structures. For the repair of existing structures, FRP laminates (approximately 1 to 2-mm thickness) have been bonded to the tension surface of beams and slabs. FRP sheets and fabrics have been wrapped around circular columns to improve ductility and strength and have been wrapped around the webs of beams to enhance the shear strength.

The non-corrosive characteristics and high strength of FRP has made it an attractive replacement for steel reinforcement in concrete structures. FRP in the form of bars and cables has been used as both regular and prestressed reinforcement and as stirrups in new concrete structures (Rizkalla, 1997). The applications of FRP for timber structures are discussed at the end of this chapter.

2.3 STRUCTURAL BEHAVIOUR OF TIMBER

Timber is a unique engineering material because it is a defect-filled natural composite. A distinction must be made between timber and wood. Madsen (1992) defines timber as a *useful construction material produced from logs of trees* and wood as *defect-free wood.* Timber and wood, in the sense of clear wood, are two very different materials. Failure in clear wood beams in bending is initiated by wrinkles in the compression zone, while failure in timber is initiated by cracking in the tension zone. The cracking in the tension zone is created by tension perpendicular to the grain stresses where the fibres have been disturbed in the vicinity of defects such as knots or other localized slope of grain. The presence of defects in timber causes different behaviour in bending and tension than in compression. Defects also cause the strength to vary with the length and depth of the member. The stress-strain behaviour of timber and size effects are discussed below.

2.3.1 Stress-Strain Behaviour

The general stress-strain relationship for wood and timber is similar, but with different relative values of compression and tension strength. Typical stress-strain relationships for wood are shown in Figure 2.1. When wood or timber are tested to failure in axial tension, the stress-strain relationship is fairly linear up to maximum load, and the wood fails in brittle tension. The tensile strength of timber is less than that for wood due to the presence of knots and other defects. In axial compression, wood and timber are much more ductile materials, exhibiting a linear stress-strain relationship up to a proportional limit, beyond which ductile yielding takes place. Yielding often produces a long decreasing plateau. For modeling purposes, the shape of the entire stress-strain relationship must be known.

2.3.2 Size Effects

It is well known that the strength of timber varies with the length and depth of a member. Bohannan (1966) used the brittle fracture theory proposed by Weibull (1939) to study the effect of size on bending strength of wood members. Brittle fracture theory assumes that there is a greater probability that a region of low strength will occur in a member of large volume than in a member of small volume. Thus, the strength of a member will decrease with increasing length and depth. Each member is assumed to consist of a large number of brittle elements selected at random from a parent population of elements with a cumulative distribution function of strength given by a Weibull distribution

$$F(x) = 1 - \exp\left\{-\left(\frac{x - x_0}{m_1}\right)^k\right\} \tag{2.1}$$

where
x = the strength
x_0 = the location parameter or minimum strength
m_1 = the scale parameter (same units as x)
k = a dimensionless shape parameter

The strength of the member is assumed to be controlled by the region of lowest strength. The shape parameter, k, reflects both the skewness and spread of the distribution and can be calculated by regressing the logarithm of strength against logarithm of volume or other appropriate scale factors. Bohannan (1966) used experimental tests and brittle fracture theory to derive

$$\left(\frac{x_1}{x_2}\right)=\left(\frac{d_2}{d_1}\right)^{1/9} \tag{2.2}$$

where x_1 = strength of member of depth d_1
x_2 = strength of member of depth d_2

For geometrically similar beams, the size effect shown in Equation (2.2) was the result of a depth effect and length effect of equal importance. The experimental tests did not show evidence of a width effect.

2.4 PREVIOUS STUDIES OF TIMBER STRENGTHENING

2.4.1 General

Over the years, the number of trees capable of providing quality structural timber have been declining, necessitating a more efficient use of the resource. Many opportunities exist for the strengthening of timber members, both for new construction and the rehabilitation of existing structures. Techniques for strengthening timber can be used to reduce the size of beams and allow the utilization of weaker species of timber, creating a more efficient use of the timber supply. The same strengthening techniques may be used to increase the load-carrying capacity of existing timber elements to support higher loads than the original design of the structure, saving the cost and material of a replacement structure. The following sections describe previous studies into the strengthening of timber elements using metallic materials and, more recently, FRP materials.

2.4.2 Metallic Materials

Some of the early investigations of reinforcing timber considered metals for reinforcement. Mark (1961) bonded aluminum plates to the top and bottom surface of wood cores and observed that failure occurred mostly due to separation and buckling of the aluminum plates. Sliker (1962) used aluminum plates between laminations of glulam beams both horizontally and vertically. Failure occurred by buckling of the plates under concentrated loads, and delamination of the plates over time was observed with dimensional changes in the wood.

Bohannan (1962) used stranded steel cable and Peterson (1965) used steel plates bonded to the tension surface to prestress laminated timber beams. Both studies reported an increase in strength for the prestressed beams and Peterson also reported an increase in stiffness. The beams tested by Bohannan did not show an increase in stiffness due to the unbonded prestressing. Lantos (1970) used steel rebar embedded in the laminations near the top and bottom of glulam beams. The strength and stiffness of the beams increased in proportion to the reinforcement. Bulleit et al. (1989) used a special lamination of flakeboard and steel rebar to reinforce glulam beams and also observed an increase in the strength and stiffness. In all of the studies, the variability in strength was less for the reinforced beams than for the unreinforced beams. None of these reinforcement techniques has reached full commercialization since they appear time consuming, require complicated steps, and have little long-term performance data to establish reliability.

2.4.3 FRP Materials

In recent years, the increased availability and reduced cost of FRP materials has stimulated increased research into reinforced timber. Plevris and Triantafillou (1992) developed a computer program to predict the behaviour of wood beams reinforced with FRP sheets bonded to the tension surface. Triantafillou and Deskovic (1992) conducted similar work using prestressed FRP sheets as reinforcement. The programs showed that small amounts of FRP reinforcement could produced significant gains in strength and stiffness. Both studies confirmed the computer predictions with experimental tests, but the work was restricted to small samples of clear wood.

Many researchers have investigated the use of FRP for reinforcing timber beams. FRP sheets (Sonti et al., 1996), CFRP strips (Chajes et al., 1996 and Bakoss et al., 1999), and GFRP strips (Dorey and Cheng, 1996 and Hernandez et al., 1997) have all been used as external reinforcement for timber. Each of these studies reported an increase in the strength and stiffness of the beams. Dorey and Cheng (1996), Hernandez et al. (1997) and Bakoss et al. (1999) all reported two events that occurred simultaneously at failure. A tensile failure in one of the bottom laminations was accompanied by partial or total delamination of the FRP strip.

Reinforcement has also been included between laminations of glulam beams. Galloway et al. (1996) used prestressed kevlar tape between the outer two laminations of glulam beams. Researchers at the University of Maine are performing detailed investigations into the behaviour of FRP-reinforced glulam beams in order to develop design specifications (Dagher and Lindyberg, 2000). Tingley and Gai (1998) present a case

study of the first highway bridge constructed with FRP-reinforced glulam. All of the above studies used glulam or laminated veneer lumber (LVL). Glulam and LVL are engineered timber products constructed by bonding together multiple laminations of smaller timber beams. The laminations are selected to reduce the presence and effects of knots, producing less variability in strength than for sawn lumber.

Work using sawn timber beams is less common in the literature. Johns and Lacroix (2000) used CFRP and GFRP sheets to reinforce "2x4" commercial lumber. They performed tests using matched samples of 25 pairs for each reinforcement type. An analysis using basic strength of materials, the design strength of the timber, and a CFRP reinforcement ratio of 0.27 percent predicted a strength increase of 10 percent for the reinforced beams compared to the unreinforced beams. The experimental results showed an increase in strength of 40 to 100 percent for the weakest beams as shown in Figure 2.2. The design strength corresponded to the strength of the weakest plain timber beams indicating large errors in the analytical predictions. It was concluded that the layer of FRP provided bridging and local confinement to the adjacent timber and caused an increase in the effective tensile strength of the timber.

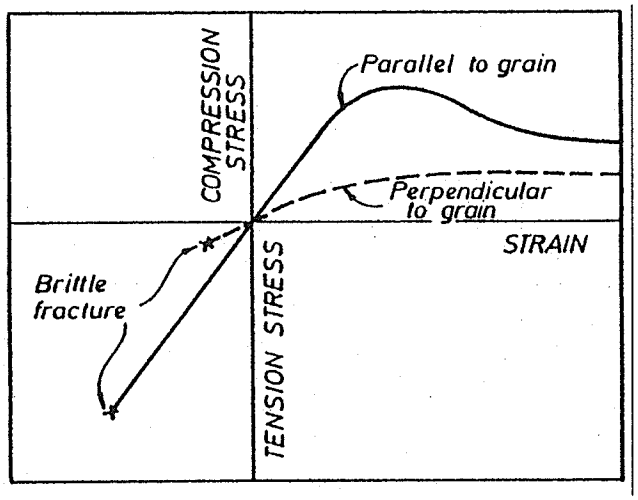

Figure 2.1 – Stress-strain relationship for wood from Buchanan (1990)

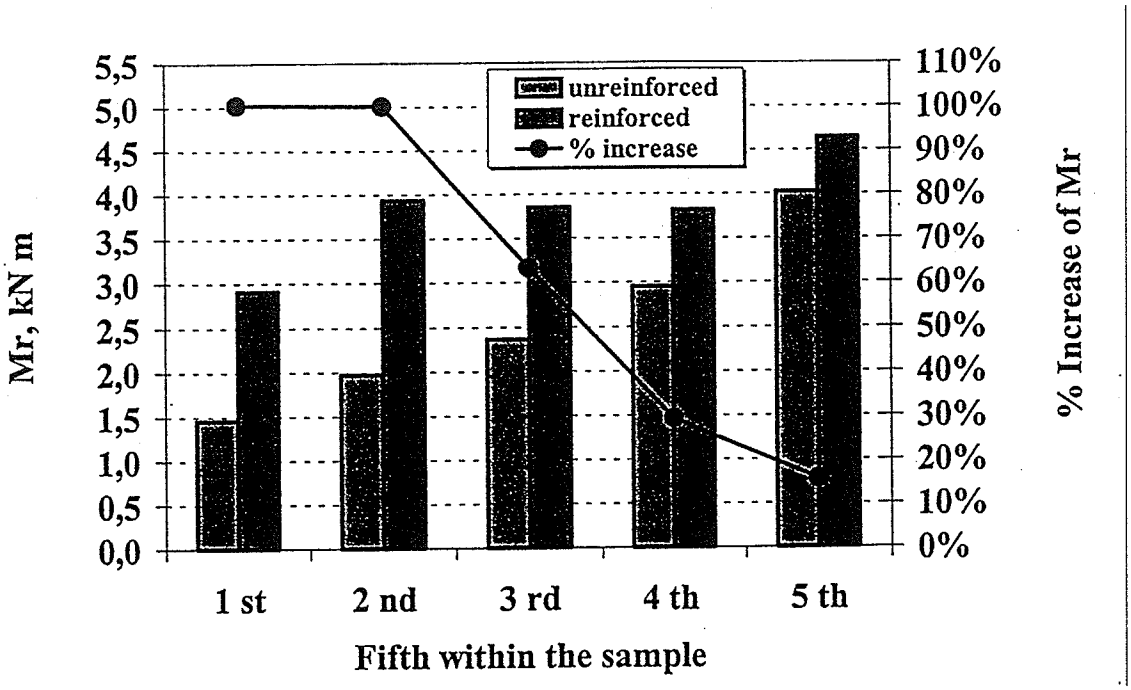

Figure 2.2 – Increases in strength by fifth of population from Johns and Lacroix (2000)

CHAPTER 3

EXPERIMENTAL PROGRAM

3.1 GENERAL

The objective of this experimental program was to investigate the use of GFRP bars for the flexural strengthening of timber bridge stringers. Three different types of specimens were used in the experimental program: bond specimens, half-scale beams, and full-scale bridge stringers. Small bond specimens were prepared to qualitatively assess the performance of the bond between the GFRP bars, epoxy, and creosote-treated timber. Twenty-two beams that were 1:2 scale models of actual timber bridge stringers were prepared and tested to failure to determine the effect of varying the reinforcement ratio. The half-scale beam specimens included seven plain timber beams and fifteen beams reinforced using three different reinforcement ratios. Four full-scale bridge stringers, including one plain timber and three reinforced timber beams, were tested to failure to confirm the results of the half-scale beams and to demonstrate the applicability of the strengthening technique to the full-scale stringers.

This chapter provides details of the timber and GFRP materials, and the specimen fabrication, test set-up and instrumentation of the three different test specimens.

3.2 MATERIALS

3.2.1 Timber

The timber material was supplied by the Manitoba Department of Highways and Government Services. All of the timber was select structural grade Douglas Fir and was pressure treated with creosote. The depth of creosote penetration averaged 50-mm along the perimeter of the cross-section on the inside of the beams. Deeper penetration occurred at locations of cracks and weak planes in the timber. The half-scale beams were prepared from new timber, while the full-scale beams were taken from an old timber bridge that had been in service for over 40 years. AASHTO (1996) specifies an allowable bending stress of 11.0 MPa (1600 psi) for Douglas Fir select structural grade timber.

3.2.2 FRP

Two different types of GFRP bars were used for flexural strengthening of the test beams. The half-scale beams were reinforced with Rotaflex Rod, produced by Rotafix (Northern) Ltd, UK. Rotaflex Rod is composed of 80 percent uni-directional E-glass fibres by weight and 20 percent thermoset epoxy resin. The rod has a deformed resin fibrous surface, which makes it highly compatible with epoxy resins. The rods used in the experimental program had 5-mm diameter, tensile strength of 1800 MPa, and modulus of elasticity of 56 GPa.

The full-scale beams were reinforced with C-BAR™, produced by Marshall Industries Composites Inc., Lima, Ohio, USA. C-BAR™ is composed of 70 percent uni-directional E-glass fibres by weight embedded in recycled PET resin. The core of the bars is

covered with a deformed surface made from urethane modified vinyl ester. The bars used in the experimental program had diameters of 10-mm and 13-mm, tensile strength of 700 MPa, and modulus of elasticity of 42 GPa. The stress-strain relationships for the two GFRP bars are shown in Figure 3.1.

3.2.3 Epoxy Resin

The GFRP bars were bonded to the timber using the Resiwood® CB10T Slow Set epoxy resin system produced by Rotafix (Northern) Ltd, UK. CB10T Slow Set is a two-part epoxy resin system that has been specially designed for timber applications. The resin has a long open time, typically 4 to 6 hours at 18°C. Initial chemical cure commences 36 hours after mixing and final cure occurs 72 hours after mixing at 18°C. The resin has a guaranteed compressive strength of 55 MPa after 5 days.

3.3 BOND SPECIMENS

3.3.1 Design and Fabrication of Specimens

Six small timber beams were prepared to qualitatively evaluate the performance of the bond between the creosote-treated timber, epoxy resin, and GFRP bars. The beams had a width of 100-mm, a depth of 130-mm, and a length of 1500-mm. Two beams were reinforced with Rotaflex Rod and four beams were reinforced with 10-mm C-BAR™. Two of the beams used C-BAR™ that had the vinyl ester coating removed by sandblasting. Table 3.1 summarizes the reinforcement used in the small beams. The cross-sections of the beams using the two different GFRP bars are shown in Figure 3.2.

The two beams reinforced with Rotaflex Rod were notched at mid-span as shown in Figure 3.3 to allow instrumentation of the GFRP rods.

CB10T Slow Set epoxy resin was used to bond the GFRP bars to the timber. A bead of epoxy was placed into grooves that had been cut into the bottom of the beams. The grooves had a depth of 15-mm and a width of 8-mm for Rotaflex Rod and 15-mm for C-BAR™. The GFRP rods were placed into the grooves and rotated to ensure a complete coating of epoxy. Additional epoxy was added to ensure complete filling of the grooves.

3.3.2 Test Set-up

Testing was conducted at the W.R. McQuade Laboratories, University of Manitoba. All beams were tested on a simply supported span of 1200-mm. The two beams reinforced with Rotaflex Rod were subjected to two symmetric point loads, with a load span of 300-mm, as shown in Figures 3.3 and 3.4, while the beams reinforced with C-BAR™ were subjected to a single point load. The monotonic static load was applied using a Riehle 60-kip testing machine under stroke control.

3.3.3 Beam Instrumentation

The strain in the GFRP bars was monitored for each beam. An extensometer with a 50-mm gauge length was used to monitor strain in the Rotaflex Rod. The strain the C-BAR was monitored using electric resistance strain gauges with a 5-mm gauge length. The applied load was measured from the output of the testing machine.

3.4 HALF-SCALE BEAMS

3.4.1 Design and Fabrication of Specimens

A total of 22 beams, including 7 plain timber and 15 reinforced timber beams, were prepared that were 1:2 scale models of full-scale timber bridge stringers. The half-scale beam specimens were cut from larger timbers with a cross-section of 300x300-mm. Each large timber yielded two half-scale beam specimens with a cross-section of 100x300-mm as shown in the detailed cutting arrangement in Figure 3.5. The reinforced timber beams were prepared with three different reinforcement ratios, ρ_{GF}, defined by

$$\rho_{GF} = \frac{A_{GF}}{bd} \tag{3.1}$$

where A_{GF} = total area of GFRP reinforcement
b = width of timber cross-section
d = depth of timber cross-section

Table 3.2 summarizes the reinforcement ratios and number of specimens tested in this part of the experimental program.

The Rotaflex Rod reinforcement was installed in grooves that were cut 30-mm above the bottom fibres into the sides of the beams as shown in Figure 3.6. The grooves had a depth of 25-mm and a width that varied from 10 to 20-mm depending on the number of rods in each groove. CB10T Slow Set epoxy resin was used to bond the GFRP rods to the timber. A bead of epoxy was placed into the grooves and then the GFRP rods were pushed into the epoxy. Additional epoxy was added to ensure complete coating of the

rods and filling of the grooves. The epoxy was allowed to cure for five days before testing. Multiple rods were used in each groove to achieve the reinforcement ratios given in Table 3.2.

3.4.2 Test Set-up

Testing was conducted at the W.R. McQuade Laboratories, University of Manitoba. All of the beams were tested in bending in accordance to ASTM D198 (1992). The beams were simply supported on rollers and tested under four-point bending with a load span of 600-mm and a support span of 4.0-m. The monotonic static load was applied using a servohydraulic MTS 1000 kN testing machine at a stroke controlled rate of 3-mm/minute. Plaster was used to distribute the load evenly at the loading points and at the supports. Lateral bracing was provided in the middle of each shear span to prevent lateral-torsional instability of the beams. A schematic of the test configuration is shown in Figure 3.7 and the typical testing of one of the beams is shown in Figure 3.8.

3.4.3 Beam Instrumentation

Deflections were measured, from the top surface of the beam, using linear variable differential transducers (LVDTs) at the mid-span of the beam, the load points, and the middle of each shear span. Strains were recorded at four locations throughout the depth at mid-span of each beam using eight 200-mm pi-gauge transducers. The strain in the GFRP reinforcement was measured using two electric resistance strain gauges bonded to the GFRP bars. Readings from all LVDTs, pi-gauges, strain gauges, and machine load and stroke were recorded by a computerized data acquisition system. When possible, loading was continued beyond peak load to obtain data in the post-failure region. All

data was recorded for the duration of the test at a rate of one sample every second. Detail of the instrumentation of the beams is shown in Figures 3.9 and 3.10.

3.5 FULL-SCALE BEAMS

3.5.1 Design and Fabrication of Specimens

The four full-scale timber beams were taken from an old bridge that had been in service for over 40 years. One of the beams was tested as a control beam while the remaining three beams were strengthened using C-BAR™. The reinforcement ratios for each beam are summarized in Table 3.3. All of the beams were reinforced by placing the bars in grooves cut into the timber. Two of the beams had grooves cut into the bottom surface of the beams and one of the beams had grooves cut into the sides of the beam in the tension zone as shown in Figure 3.11. The grooves had a depth and width of 20x20-mm, 15x15-mm, and 40x20-mm for Beams FS-1, FS-2, and FS-3, respectively. Due to the available length of C-BAR™, only the central 6.0-m of each beam was reinforced.

The C-BAR™ reinforcement had the vinyl ester coating removed by sandblasting and was installed following the same procedure that was used for the half-scale beams. CB10T Slow Set epoxy resin was used to bond the GFRP rods to the timber. After the grooves had been cut into the beams, shown in Figure 3.12(a), a bead of epoxy was placed into the grooves as shown in Figure 3.12(b). The GFRP bars were pushed into the epoxy, shown in Figure 3.12(c), and additional epoxy was added to ensure complete coating of the rods and filling of the grooves as shown in Figure 3.12(d). Staples were

used to hold the bars for the two beams with grooves on the bottom. The epoxy was allowed to cure for five days before testing.

3.5.2 Test Set-up

Testing was conducted at the W.R. McQuade Laboratories, University of Manitoba. All of the beams were tested in bending in accordance to ASTM D198 (1992). The beams were simply supported on rollers and tested under four-point bending with a load span of 1200-mm and a support span of 10.0-m. The monotonic static load was applied using a servohydraulic MTS 5000 kN testing machine at a stroke controlled rate of 9-mm/minute. For the control beam, Beam FS-4, the load was applied at a stroke controlled rate of 1-mm/minute. Plaster was used to distribute the load evenly at the loading points and at the supports. Lateral bracing was provided at the load points to prevent lateral-torsional instability of the beams. A schematic of the test configuration is shown in Figure 3.13 and the typical testing of one of the beams is shown in Figure 3.14.

3.5.3 Beam Instrumentation

Deflections were measured, from the top surface of the beam, using LVDTs at five locations along the length of the beam. Strains were recorded at three locations throughout the depth at mid-span of each beam using six 200-mm pi-gauge transducers. The strain in the GFRP reinforcement was measured using two electric resistance strain gauges bonded to the GFRP bars. Readings from all LVDTs, pi-gauges, strain gauges, and machine load and stroke were recorded by a computerized data acquisition system. When possible, loading was continued beyond peak load to obtain data in the post-failure

region. All data was recorded for the duration of the test at a rate of one sample every second. Detail of the instrumentation of the beams is shown in Figures 3.15 and 3.16.

Table 3.1 – Reinforcement for Bond Specimens

No. of Specimens	Reinforcement Type
2	2 5-mm Rotaflex Rods
2	10-mm C-BAR™ (coated)
2	10-mm C-BAR™ (sandblasted)

Table 3.2 – Reinforcement Ratios for Half-Scale Beams

ρ_{GF} (%)	No. of Beams
0	7
0.27	3
0.41	6
0.82	6
Total	22

Table 3.3 – Reinforcement Ratios for Full-Scale Beams

Beam ID	ρ_{GF} (%)	Reinforcement Configuration
FS-1	0.42	Bottom
FS-2	0.26	Bottom
FS-3	0.42	Side
FS-4	0	None

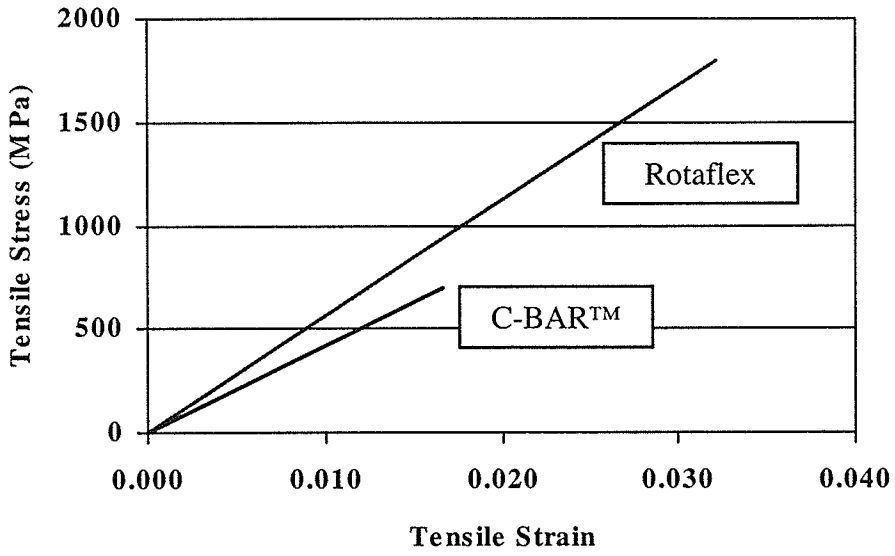

Figure 3.1 – Tensile stress-strain relationships for GFRP

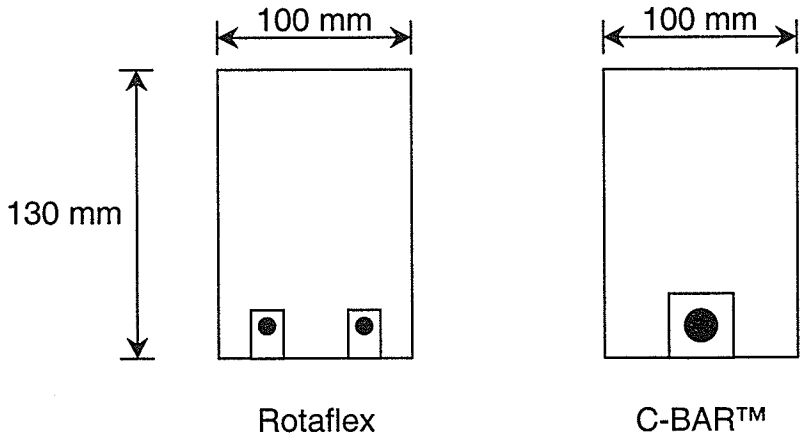

Figure 3.2 – Cross-section of bond specimens

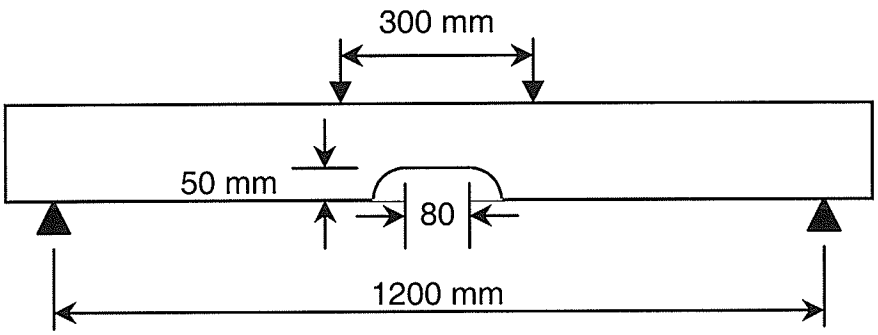

Figure 3.3 – Bond specimen using Rotaflex Rod

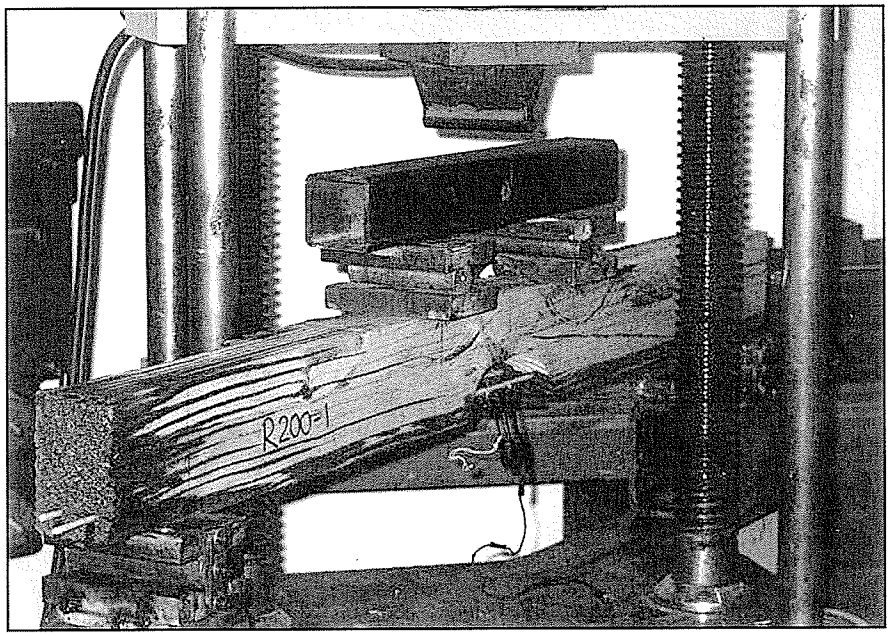

Figure 3.4 – Test set-up for bond specimens

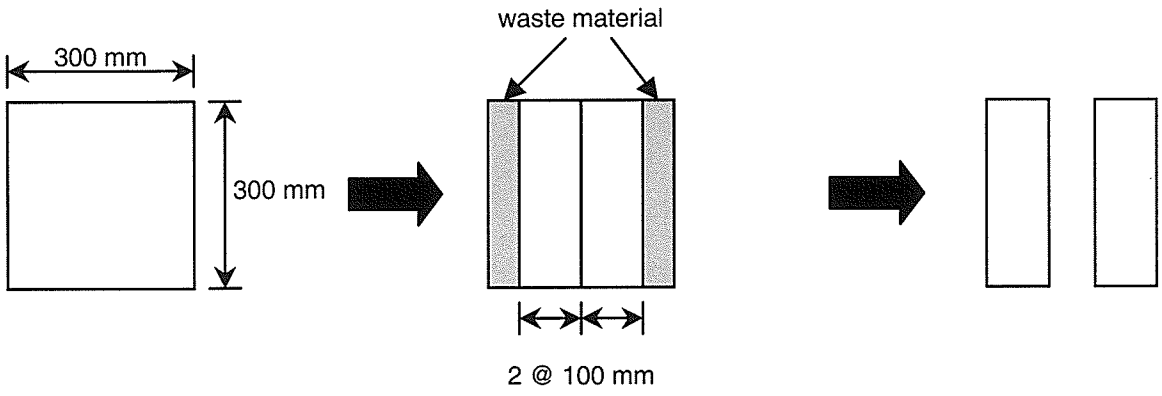

Figure 3.5 – Cutting arrangement to produce two half-scale beams

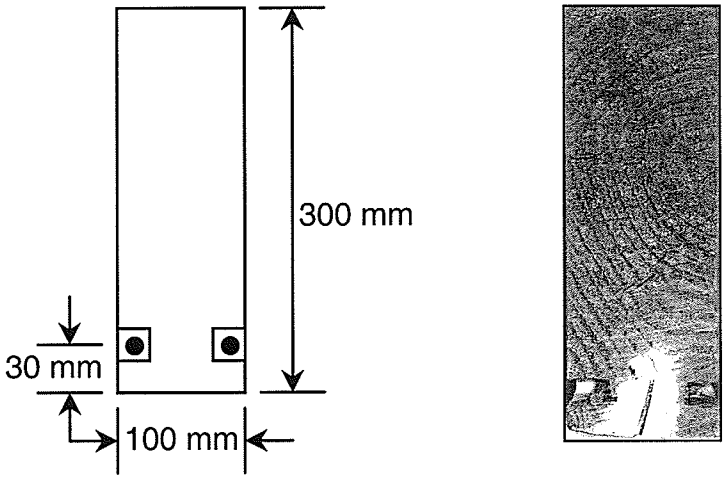

Figure 3.6 – Cross-section of half-scale reinforced timber beam

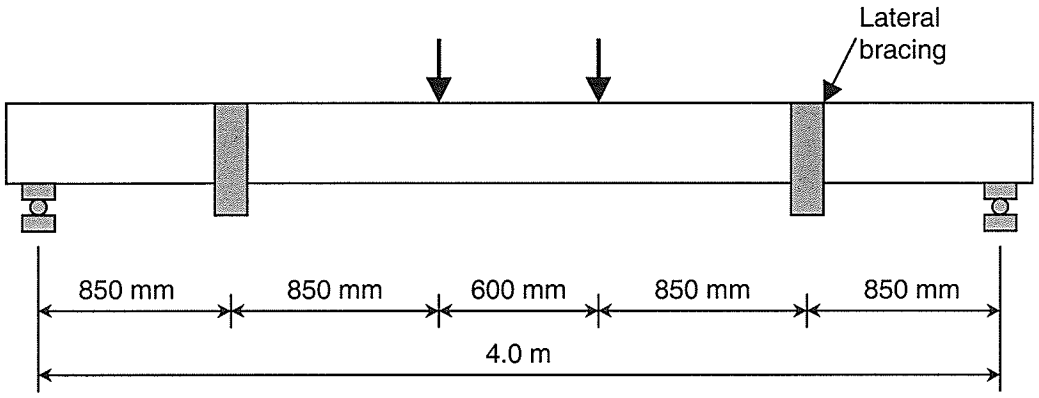

Figure 3.7 – Test configuration for half-scale beams

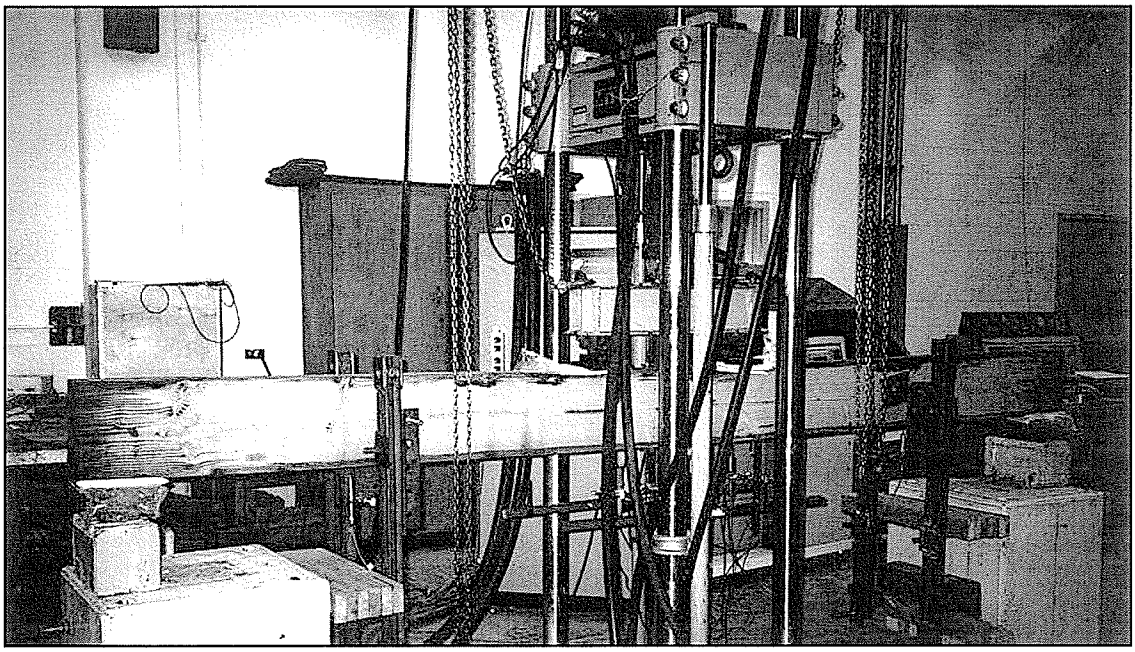

Figure 3.8 – Test set-up for half-scale beams

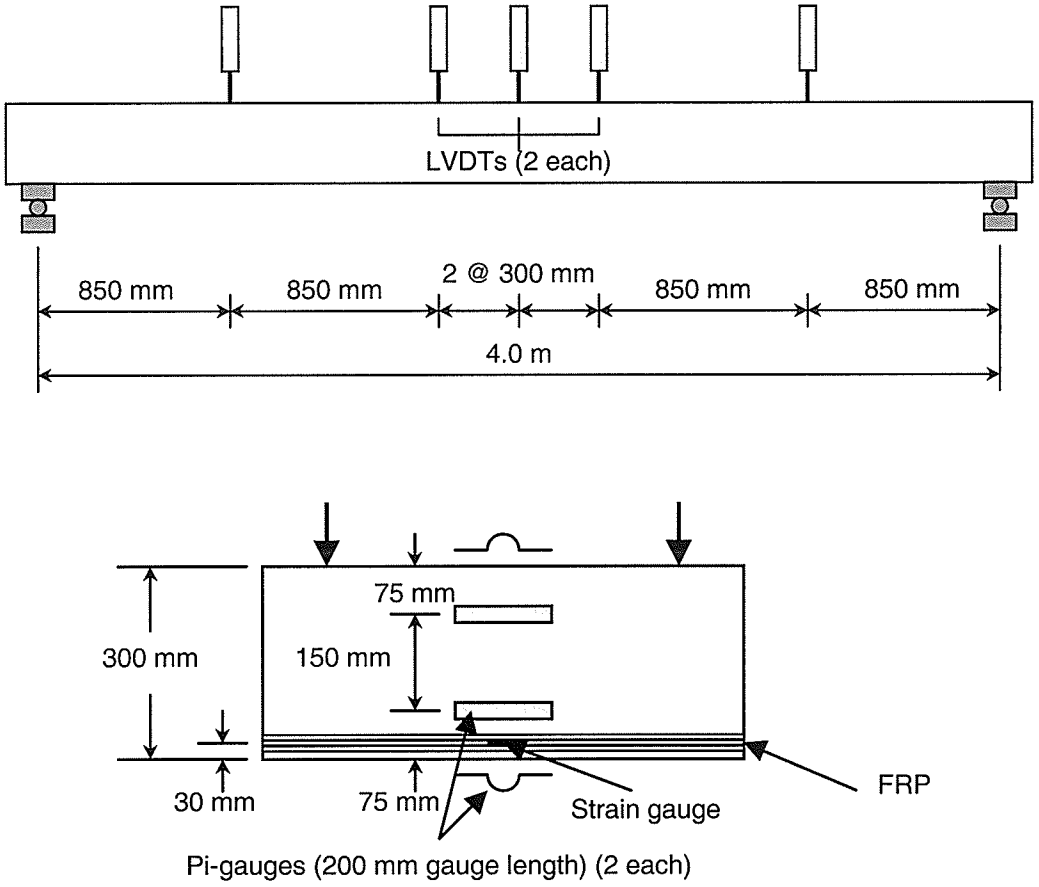

Figure 3.9 – Detail of instrumentation for half-scale beams

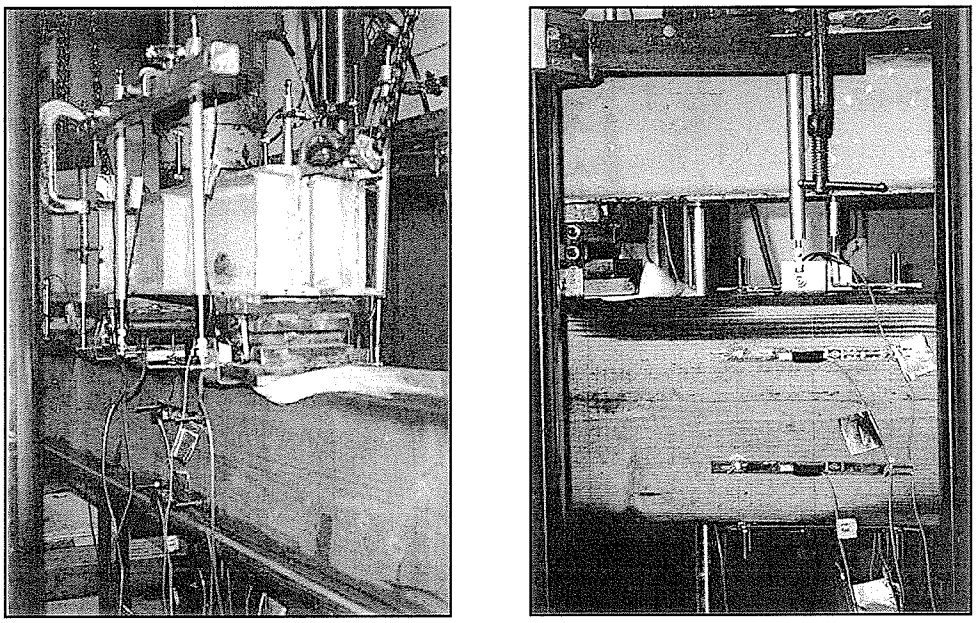

Figure 3.10 – Instrumentation at mid-span of half-scale beams

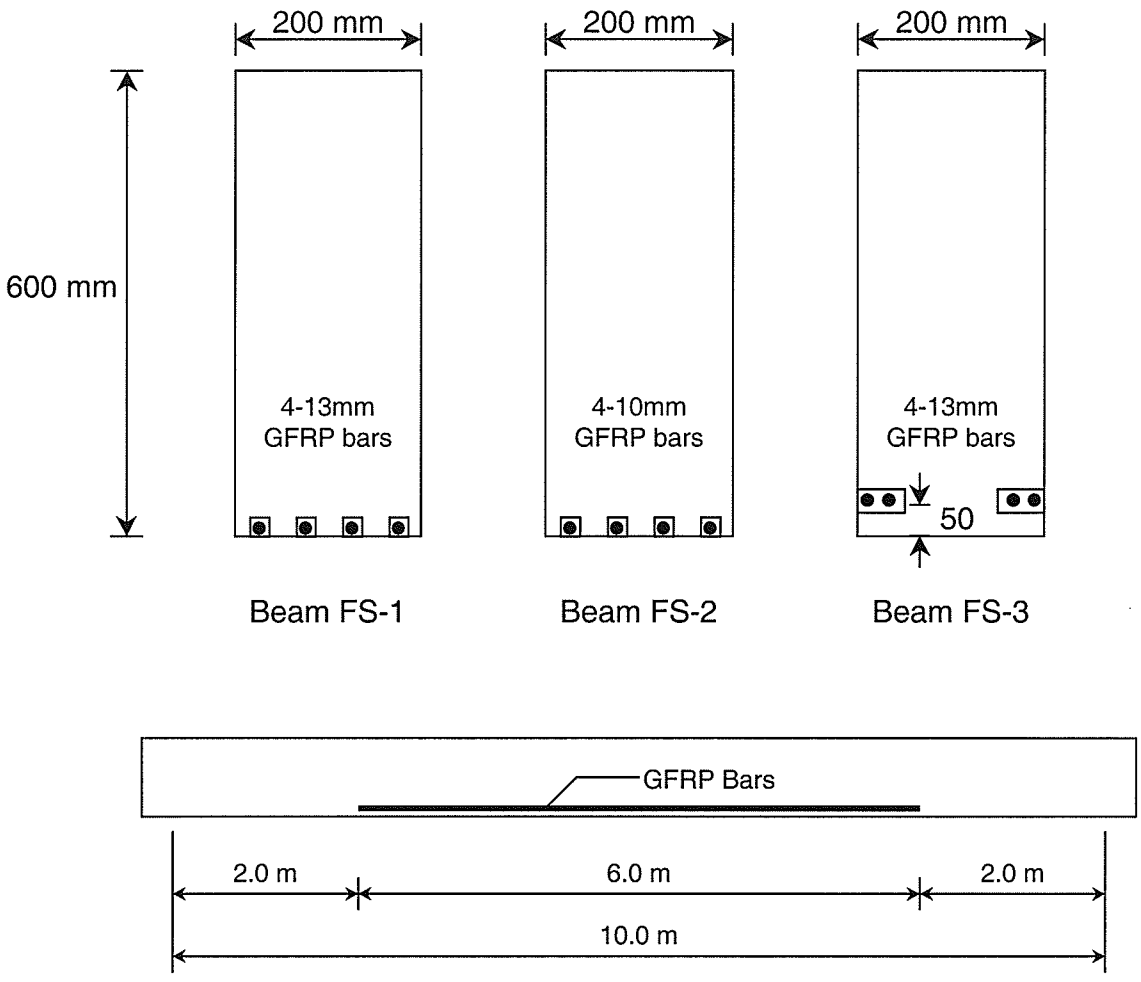

Figure 3.11 – Configuration of full-scale reinforced timber beams

Figure 3.12(a) –Full-scale beams: cutting of grooves

Figure 3.12(b) –Full-scale beams: application of epoxy

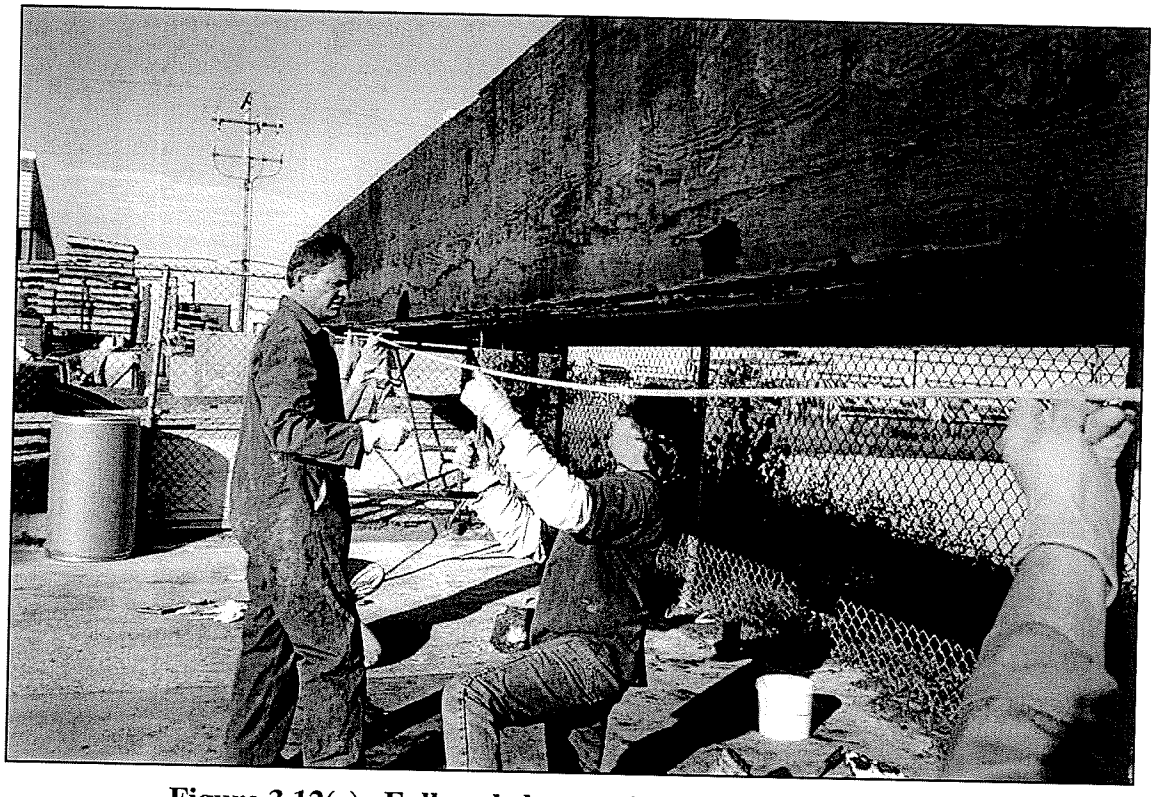

Figure 3.12(c) –Full-scale beams: installation of C-BAR™

Figure 3.12(d) –Full-scale beams: filling of grooves with epoxy

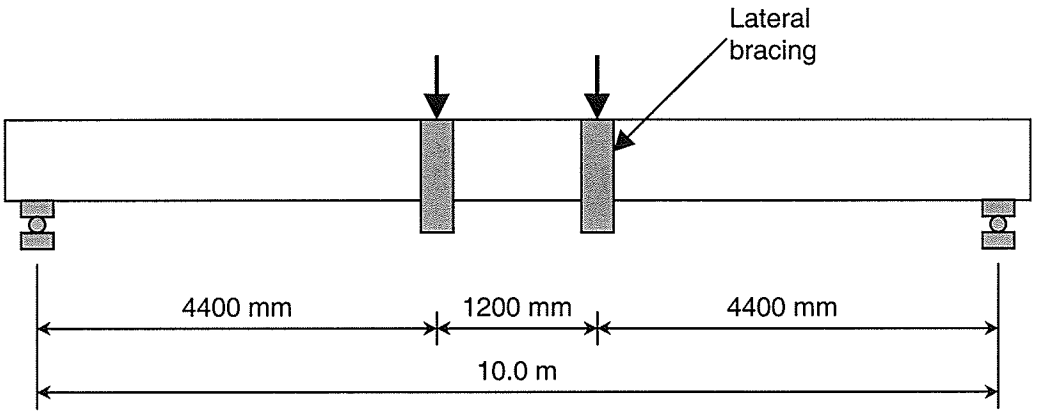

Figure 3.13 – Test configuration for full-scale beams

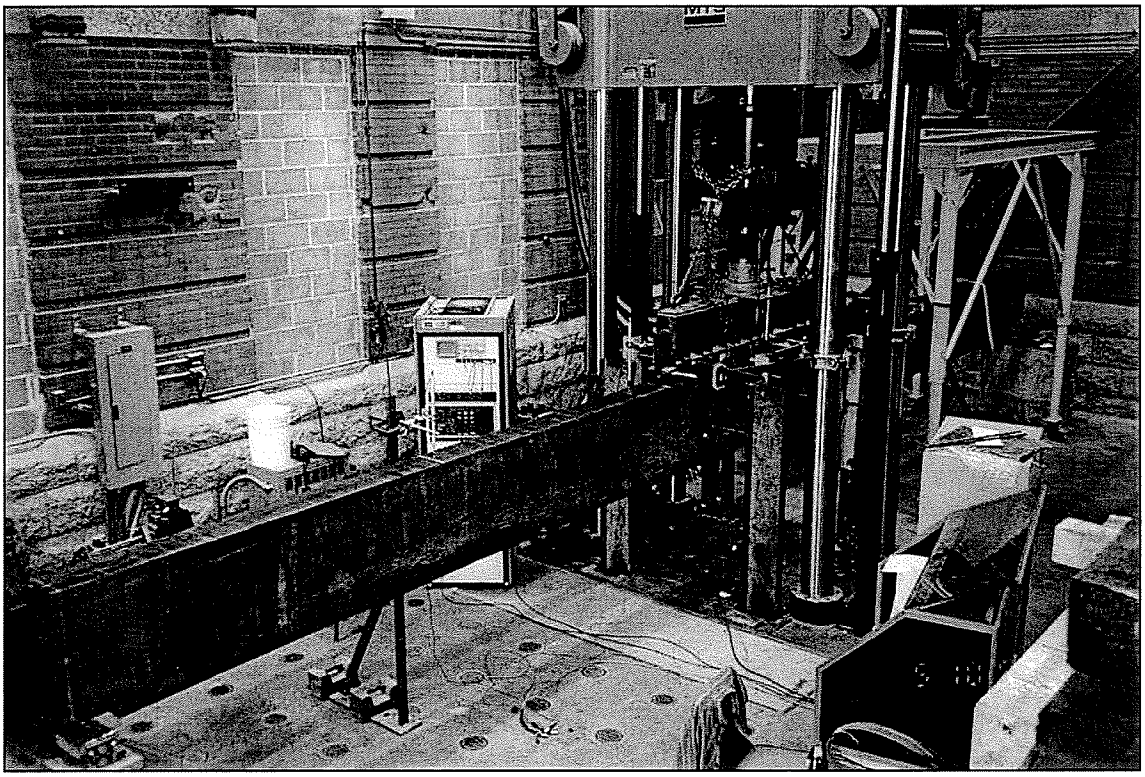

Figure 3.14 – Test set-up for full-scale beams

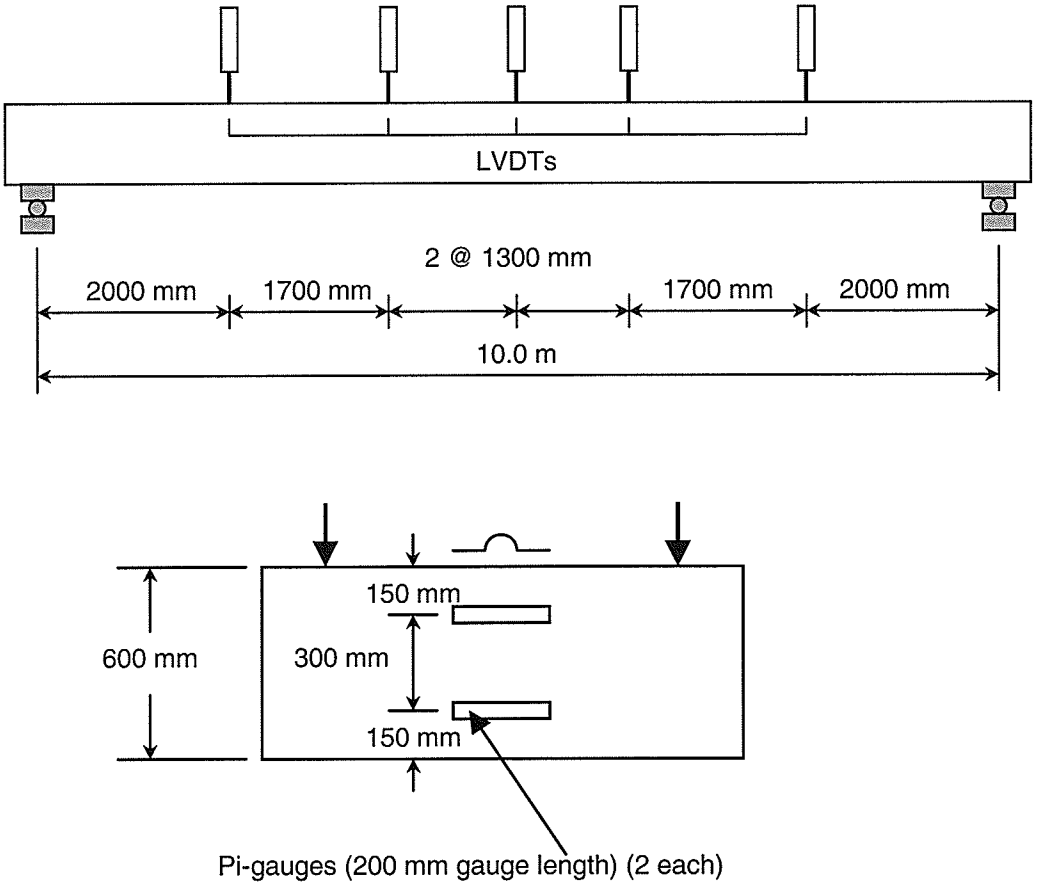

Figure 3.15 – Detail of instrumentation for full-scale beams

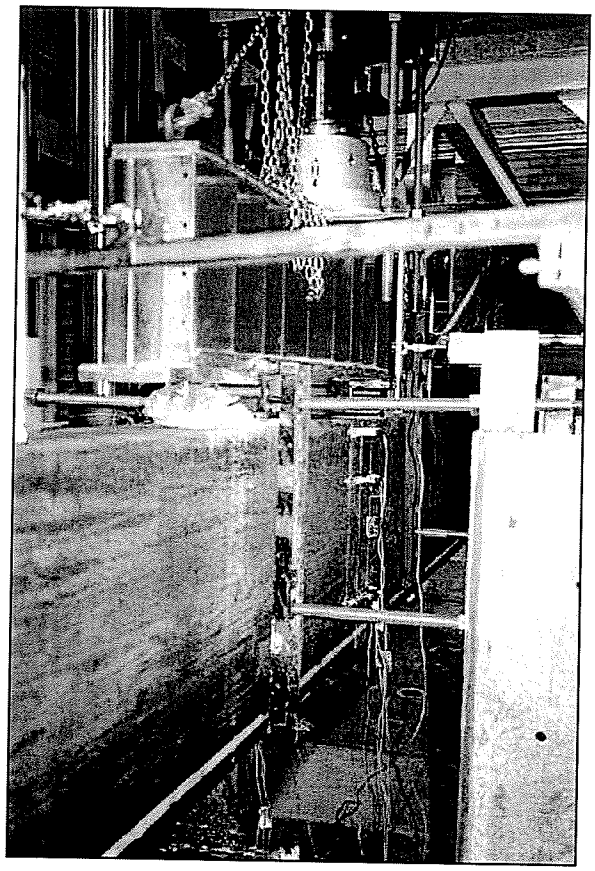

Figure 3.16 – Instrumentation at mid-span of full-scale beams

CHAPTER 4

EXPERIMENTAL RESULTS AND ANALYSIS

4.1 GENERAL

Six small timber beams were reinforced with GFRP bars to qualitatively assess the performance of the bond between the creosote-treated timber, epoxy resin, and GFRP bars. After satisfactory bond performance was observed, twenty-two beams, 1:2 scale models of typical timber bridge stringers, were tested to failure. Seven half-scale beams were used as control beams and fifteen half-scale beams were reinforced with GFRP bars using three different reinforcement ratios. In order to extend the applicability of the experimental results to typical timber bridge stringers, three full-scale stringers, taken from a 40 year-old timber bridge, were reinforced using GFRP bars. A fourth full-scale stringer was used as an unreinforced control beam. All of the beams were tested to failure to determine the effect of varying the reinforcement ratio. This chapter describes the results of the six bond specimens, twenty-two half-scale beam tests, and four full-scale beam tests conducted in this experimental program.

4.2 BOND SPECIMENS

Six small timber beams with a cross-section of 100x130-mm and a length of 1500-mm were reinforced with GFRP bars and tested to failure. The GFRP bars were installed in grooves cut 15-mm deep into the bottom of the beams. The strain in the GFRP bars was monitored up to and beyond failure of the timber beams and the maximum measured strain in the bars is reported in Table 4.1. All of the beams failed due to crushing of the timber in the compression zone as shown in Figure 4.1.

The two beams reinforced with coated C-BAR™ experienced slip and debonding of the GFRP bars as shown in Figure 4.2. Total debonding of the bars occurred from mid-span to one end of the beams after reaching the maximum load. The failure surface between the bars and epoxy was completely smooth and the epoxy had imprints corresponding to the deformed ribs of the C-BAR™. The behaviour suggests that the bond strength was provided mainly by bearing stresses induced by the deformed ribs. The smooth surface indicates a lack of chemical bond between the epoxy and the bars.

Debonding and slip of the GFRP reinforcement did not occur in the specimens reinforced with Rotaflex Rod and the sandblasted C-BAR™. At failure, several cracks were observed in the epoxy matrix as well as minor localized debonding at locations adjacent to cracks in the timber; however, the bars were fully bonded to the epoxy outside the failure region. The failure surface between the bars and the epoxy showed that the epoxy had penetrated into the surface of the bars, resulting in an increase in the bond strength.

There were no short-term problems with the bond between the epoxy and the timber, even in locations with creosote penetration. Long-term durability tests of the epoxy-timber bond were not performed. In all of the beams, the maximum recorded strain in the GFRP bars was greater than 0.005, which was the expected maximum tensile strain of the timber. Based on the results from the bond specimens, it was decided to use uncoated C-BAR™ to reinforce the full-scale beams.

4.3 HALF-SCALE BEAMS

4.3.1 Failure Mode

Twenty-two beams with a cross-section of 100x300-mm and a length of 4.3-m were loaded monotonically up to failure. Fifteen half-scale beams were reinforced with GFRP bars installed in grooves that were cut 30-mm above the bottom fibres into the sides of the beams. The grooves had a depth of 25-mm and a width that varied from 10 to 20-mm depending on the number of bars in each groove. Figure 4.3 shows a typical beam at failure. Out of the 22 beam specimens tested in this part of the program, 19 beams failed in flexure, while 3 beams failed in a combination of flexure and shear. This research program is concerned with flexural strengthening only, so the data from the flexural-shear failures was excluded from the analysis.

For the flexural failures, two failure modes were observed: compression and tension. If the beam exhibited crushing in the compression zone at maximum load, the failure was classified as a compression failure. If crushing did not occur at the maximum measured load, the failure was classified as a tension failure. Figures 4.4 and 4.5 show typical

compression and tension failure modes, respectively. It can be seen in Figure 4.4 that for compression failure, cracking is present in the tension zone. All of the beams initially cracked in the tension zone, but for the compression failures, crushing in the compression zone controlled the ultimate load. Table 4.2 summarizes the failure modes observed for the different reinforcement ratios used in this part of the experimental program.

All of the plain timber beams failed in tension with no sign of crushing in the compression zone. For the reinforced beams that failed in flexure, 60 percent of the beams failed in a compression failure mode. The addition of the GFRP bars caused a change in the failure mode from brittle tension in the plain timber specimens to a more ductile compression-initiated failure in the compression zone of the reinforced specimens. Due to the high strength of the GFRP reinforcement, the GFRP bars did not rupture in any of the beams. There was some localized debonding of the bars adjacent to tension cracks in the timber, but the bond between the bars, epoxy, and timber remained intact outside the failure region. None of the failures were due to debonding or delamination of the reinforcement as has been observed in applications using FRP sheets or strips for external reinforcement (Dorey and Cheng 1996, Hernandez et al. 1997, and Bakoss et al. 1999).

4.3.2 Load-Deflection

The load-deflection curves for typical plain and GFRP-reinforced timber specimens are shown in Figure 4.6. Test results showed a large variation in the measured stiffness and strength for both the plain and reinforced specimens. The curves shown in Figure 4.6

represent the lower and upper bound behaviour of the stiffness range of the tested beams. The load-deflection curves for each beam are included in Appendix A.

For the plain timber beams, the initial variation 0-A´ was linear until the timber cracked in the tension zone at point A´. Failure usually occurred at or shortly beyond point A´. For the stiffest and strongest plain timber specimens, some non-linearity of the load-deflection was observed and a minor increase in load carrying capacity was achieved after point A´. Failure in the plain timber beams was always governed by the tensile strength of the timber in bending.

For the reinforced beams, the initial variation 0-A was linear until the timber cracked in the tension zone at point A. The stiffness then gradually decreased until maximum load was reached at point B and crushing started in the compression zone. Deflection continued to increase with a minor decrease in load up to point C, at which point a significant crack occurred in the tension zone, causing a rapid drop in load to point D. The reinforced beam was capable of additional deflection and load carrying capacity up to point E where the tests were terminated due to limitations of the testing equipment. The reinforced beams behaved linearly up to 65 to 95 percent of the ultimate load.

4.3.3 Strain Distribution

For each of the half-scale beams, the strain in the timber was monitored at four locations at mid-span using pi-gauges with a gauge length of 200-mm, as was shown in Figure 3.9. The strain in the GFRP bars was measured using electric resistance strain gauges bonded to the bars in the reinforced beams. All strains were measured for the duration of the test,

but a continuous record of strain was not always possible. Cracking of the beams sometimes caused the pi-gauges to detach from the surface of the beam and prevented further measurement of the strain. The typical load-deflection curves for plain and reinforced timber are shown in Figures 4.7(a) and 4.8(a), respectively, and the corresponding load-strain curves are shown in Figures 4.7(b) and 4.8(b), respectively. The load-strain curves for each beam are included in Appendix A.

For the plain timber beam, the load-strain relationship, shown in Figure 4.7(b), was linear up to initiation of cracks in the tension zone. Cracking is reflected by the discontinuities in the load-deflection curve, shown in Figure 4.7(a), and the load-strain curve at a load level of 30 kN. After cracking, the load-strain relationship remained linear, but with a reduced slope, reflecting the reduced stiffness of the cracked section. The strain profile for the plain timber beam is shown at three different load levels in Figure 4.9. It can be seen that strain profile was approximately linear for all load levels, confirming the assumption from bending theory that plane sections originally plane remain plane during bending.

For the reinforced timber beam, the load-strain relationship, shown in Figure 4.8(b), was linear up to initiation of cracks in the tension zone. Cracking is reflected by the discontinuities in the load-deflection curve, shown in Figure 4.8(a), and the load-strain curve at a load level of 68 kN. After cracking the load strain relationship was non-linear, reflecting the gradual loss in stiffness as cracks propagated through the tension zone. The strain profile for the reinforced timber beam is shown at three different load levels in

Figure 4.10. As for the plain timber beam, the strain profile of the reinforced timber beam was approximately linear for all load levels. The strain measured in the GFRP bars fits very well with the strains measured in the timber. This behaviour indicates complete bond between the creosote-treated timber, epoxy, and GFRP bars. For modeling purposes, it would be valid to assume the strain in the GFRP bars was equivalent to the strain in the adjacent timber.

Table 4.3 summarizes the average tensile strains at failure for the plain and reinforced beams. For the reinforced beams, the tensile strain in timber is based on the measured strain in the GFRP bars since cracking of the beams prevented measurement of the strain on the bottom of the beams at failure. Assuming the neutral axis was located at mid-height of the beam and a linear strain profile, the strain on the bottom would be 25 percent greater than the measured strain in the GFRP bars based on the geometry of the section shown in Figure 3.9. The GFRP reinforcement caused an increase in the extreme fibre strain at failure from 0.0035 to 0.0058, which represents an increase of 64 percent. This supports the conclusions of Johns and Lacroix (2000) that the presence of FRP material arrests the crack opening, confines local rupture, and bridges local defects in the timber. The result is that the timber can support higher nominal stresses and strains before failing.

4.3.4 Strength and Ultimate Load

Table 4.4 presents a summary of the average ultimate load, and modulus of rupture (MOR) for the different reinforcement ratios examined using the half-scale beams tested in this experimental program. Table 4.5 provides the modulus of elasticity (MOE), ultimate load, and MOR for each individual beam tested. The MOR was calculated using

$$MOR = \frac{M_F}{S_g} \tag{4.1}$$

where M_F = bending moment at failure location
S_g = section modulus based on gross section properties

The self-weight of the beams was included in the calculation of MOR. Two of the reinforced beams (one each for ρ_{GF} of 0.27% and 0.82%) failed outside of the constant moment region, and this has been taken into account in the calculation of MOR. The MOE was calculated from the initial linear-elastic behaviour for each beam using

$$E = \frac{Pa}{48\Delta I_T}\left(3L^2 - 4a^2\right) \tag{4.2}$$

where E = modulus of elasticity
P = total applied load
Δ = deflection at mid-span
I_T = moment of inertia of transformed section
L = span of the beam
a = shear span of the beam

Test results indicate that the increase in ultimate load ranged from 48 to 60 percent, while the increase in MOR was between 40 and 53 percent. The lower increase in average MOR was due to the fact that some beams failed outside of the constant moment region. The test results appear to indicate that the MOR increased with increasing reinforcement ratio, but this cannot be a conclusive statistical comparison due to the limited number of specimens tested.

There was a wide range of strength and stiffness observed for each reinforcement ratio used in the experimental program. Figure 4.11 shows the relationship between MOR and MOE for all the tested beams. The measured values indicate that MOR increased with increasing MOE for both the plain and reinforced timber beams. This behaviour was also reported by Johns and Lacroix (2000). The data for different reinforcement ratios are equally scattered across the average range of MOR and MOE for the plain and reinforced timber data sets. In spite of the fact that there is no obvious trend, the average can be used to determine an approximate value of MOR for a given value of MOE for both plain and reinforced timber beams. The linear trends shown in Figure 4.11 were used to determine the strength enhancement for a wide range of timber strength as shown in Figure 4.12. For the range of reinforcement ratios considered in this experimental program, the strength enhancement was between 38 percent (for timber strength of 45MPa) and 50 percent (for timber strength of 20MPa). These values of strength enhancement compare well to the results reported by Johns and Lacroix (2000). Analytical modeling of the strength and bending behaviour is presented in Chapter 5.

4.4 FULL-SCALE BEAMS

4.4.1 Failure Mode

Four full-scale timber stringers with a cross-section of 200x600-mm were loaded monotonically up to failure. Three stringers were reinforced with GFRP bars installed in grooves cut into the timber. Two of the stringers had grooves cut into the bottom surface and one stringer had grooves cut 50-mm above the bottom fibres into the sides of the beam. The GFRP-strengthened beams underwent large deflections before failure as shown in Figure 4.13. Two flexural failure modes were observed for the full-scale beams: tension and compression. Table 4.6 summarizes the failure modes observed for each of the full-scale beams.

The plain timber specimen, Beam FS-4, failed in tension by progressive cracking in the tension zone. Beam FS-1 also failed in tension when tension cracks propagated suddenly along a weak plane in the timber. Figure 4.14 shows the tensile failure of Beam FS-1. Beams FS-2 and FS-3 both failed in compression and underwent substantial deflection before failure. Significant crushing occurred in the compression zone and both beams underwent additional deflection and a decrease in supported load until excessive cracking occurred in the tension zone. Figure 4.15 shows the compression failure of Beam FS-2.

The failure modes observed for the full-scale beams were the same as those observed for the half-scale beams. The addition of the GFRP bars caused a change in the failure mode from brittle tension in the plain timber specimens to a more ductile compression-initiated failure in the reinforced specimens. Due to the high strength of the GFRP reinforcement, the GFRP bars did not rupture in any of the beams. There was some localized debonding

of the bars adjacent to tension cracks in the timber, but the bond between the bars, epoxy, and timber remained intact outside the failure region.

4.4.2 Load-Deflection

The load-deflection curves, for the four full-scale beams, are shown in Figure 4.16 and the load-deflection curves for each beam individually are included in Appendix A. For beam FS-4, the initial variation 0-A´ was linear until the timber cracked in the tension zone at point A´. The beam underwent significant additional deflection with increased load carrying capacity until maximum load was reached at point B´. The relative size of the segment A´-B´ was greater for Beam FS-4 than for the half-scale plain timber beams. A much slower loading rate was used for Beam FS-4 so that failure occurred after 2 hours, while failure of the half-scale timber beams occurred after 10 to 20 minutes. The increased load-duration for Beam FS-4 caused cracking to initiate sooner than for the half-scale timber beams.

For Beam FS-2, the initial variation 0-A was linear until the timber cracked in the tension zone at point A causing a drop in the supported load to point B. With decreased stiffness, the load increased to point C where crushing started and the timber cracked again in the tension zone causing a drop in the supported load to point D. The load and deflection continued to increase up to point E, which was at the same load level as point C. Beyond point E, the beam underwent additional deflection with a steady decrease in supported load until the test was terminated at point F due to excessive deflection.

The general load-deflection behaviour for the full-scale beams was very similar to the behaviour of the half-scale beams. Note that all of the reinforced beams behaved linearly up to 95 percent of the ultimate load.

4.4.3 Strain Distribution

For each of the full-scale beams, the strain in the timber was monitored at three locations at mid-span using pi-gauges with a gauge length of 200-mm, as was shown in Figure 3.15. The strain in the GFRP bars was measured using electric resistance strain gauges bonded to the bars in the reinforced beams. All strains were measured for the duration of the test, but a continuous record of strain was not always possible. Cracking of the beams sometimes caused the pi-gauges to detach from the surface of the beam and prevented further measurement of the strain. The load-deflection and load strain curves for Beam FS-2 are shown in Figures 4.17(a) and 4.17(b), respectively. The load-strain curves for each full-scale beam are included in Appendix A.

For Beam FS-2, the load-strain relationship, shown in Figure 4.17(b), was linear up to initiation of cracks in the tension zone. Cracking is reflected by the discontinuities in the load-deflection curve, shown in Figure 4.17(a), and the load-strain curve at a load level of 272 kN. The strain gauges on the GFRP bars were damaged when the beam cracked and did not provide accurate strain readings for the remainder of the test. Vibration of the beam during cracking also disturbed the pi-gauges, which prevented further measurement of the strain. The strain profile for Beam FS-2 is shown at three different load levels in Figure 4.18. As for the half-scale beams, the strain profile was linear at all load levels. The strain measured in the GFRP bars fit very well with the strains measured in the

timber. This confirms that there was excellent bond between the timber, epoxy, and GFRP bars.

4.4.4 Stiffness

The three reinforced beams were tested in bending up to a load level of 40 kN prior to strengthening so that the effect of strengthening on bending stiffness could be evaluated. Using a modified Equation (4.2) the stiffness was calculated from the initial linear-elastic behaviour of each beam

$$EI = \frac{Pa}{48\Delta}\left(3L^2 - 4a^2\right) \tag{4.3}$$

Table 4.7 presents the stiffness of the strengthened and unstrengthened beams and compares the increase in stiffness to analytical predictions. The analytical predictions were calculated using a transformed section analysis. The measured increase in stiffness ranged from 0 to 7.4 percent, while the transformed section analysis predicted a stiffness increase ranging from 1.4 to 3.4 percent. A large increase in stiffness was not expected due to the low reinforcement ratios used in the experimental program. The small number of full-scale beams tested makes it difficult to evaluate the accuracy of the stiffness predictions.

4.4.5 Strength and Ultimate Load

Table 4.8 provides the experimental results, including MOE, ultimate load, and MOR for each of the full-scale beams. MOE was calculated using equation (4.2) and MOR was

calculated using equation (4.1). The self-weight of the beams was included in the calculation of MOR.

All of the reinforced beams were significantly stronger than the unreinforced Beam FS-4. There was a wide range of strength and stiffness observed for each of the full-scale beams and it was not possible to establish a relationship between the two properties due to the small number of beams tested. Figure 4.19 shows the experimental results from the full-scale beams included in the relationship between MOR and MOE for the half-scale beams, previously shown in Figure 4.11. It can be seen that the points for Beams FS-1, FS-2, and FS-3 all match the trend defined by the half-scale reinforced beams. The data point for Beam FS-4 appears to fall slightly below the trend defined by the half-scale plain timber beams. Beam FS-4 was tested at a much slower loading rate than the other beams and the measured strength is probably lower than the true short-term strength due to duration of load effects. The data shown in Figure 4.19 suggests that there was no size effect between the half-scale and full-scale beams.

Table 4.1 – Summary of Bond Specimen Results

Reinforcement	$\varepsilon_{GF\ max}$	Debonding
Rotaflex	0.021	No
Rotaflex	N/A †	No
C-BAR™ (coated)	0.009	YES
C-BAR™ (coated)	0.011	YES
C-BAR™ (sandblasted)	0.011	No
C-BAR™ (sandblasted)	N/A *	No

† extensometer not working properly
* strain gauge damaged

Table 4.2 – Observed Failure Modes for Half-Scale Beams

ρ_{GF} (%)	No. of Beams	Failure Modes
0	7	Tension (7)
0.27	3	Tension (1) Compression (2)
0.41	6	Tension (2) Compression (2) Flexure-Shear (2)
0.82	6	Tension (2) Compression (3) Flexure-Shear (1)

Table 4.3 – Summary of Tensile Strains at Failure

Beam	Avg ε_F	Location
Plain Timber	0.0035	Bottom
Reinforced	0.0046	GFRP bars
Reinforced	0.0058*	Bottom

* calculated from ε_F of GFRP assuming neutral axis is at mid-height and a linear strain profile

Table 4.4 – Summary of Ultimate Load and MOR for Half-Scale Beams

ρ_{GF} (%)	No. of Beams	Avg P_{ult} (kN)	% Increase in P_{ult}	Avg MOR (MPa)	% Increase in MOR
0	7	46.6	N/A	26.7	N/A
0.27	3	72.8	56	37.3	40
0.41	4	68.9	48	39.4	48
0.82	5	74.6	60	40.9	53

Table 4.5 – Experimental Results for Half-Scale Beams

ρ_{GF} (%)	Beam ID	MOE (MPa)	P_{ult} (kN)	MOR (MPa)
0	F1	6999	32.5	18.8
	J1	7602	34.4	19.8
	B1	8568	37.5	21.6
	H1	9654	43.5	25.0
	C1	10197	64.7	37.0
	A1	10257	36.9	21.2
	G1	14662	76.5	43.7
0.27	F2	6039	40.0	23.0
	D2*	11189	85.7	36.0
	D1	12491	92.6	52.8
0.41	L1	7274	47.2	27.1
	K1	7450	65.1	37.2
	H2	9327	55.9	32.0
	I1	14724	107.5	61.3
0.82	L2	7598	59.6	34.1
	K2*	7770	57.0	24.1
	A2	10855	75.8	43.3
	G2	10969	77.4	44.2
	I2	13140	103.0	58.7

* Failure occurred outside of the constant moment region

Table 4.6 – Observed Failure Modes for Full-Scale Beams

Beam ID	ρ_{GF} (%)	Reinforcement Location	Failure Mode
FS-1	0.42	Bottom	Tension
FS-2	0.26	Bottom	Compression
FS-3	0.42	Side	Compression
FS-4	0	None	Tension

Table 4.7 – Bending Stiffness of Full-Scale Beams

Beam ID	EI ($x10^{12}$ N-mm^2)		$\frac{(EI)_{reinf.}}{(EI)_{initial}}$	$\frac{I_T}{I_g}$
	Initial	Reinforced		
FS-1	37.8	37.8	1.000	1.034
FS-2	47.8	50.3	1.052	1.014
FS-3	30.4	32.7	1.074	1.033

Table 4.8 – Experimental Results for Full-Scale Beams

ρ_{GF} (%)	Beam ID	MOE (MPa)	P_{ult} (kN)	MOR (MPa)
0.42	FS-1	10506	236	44.3
0.26	FS-2	13276	296	55.3
0.42	FS-3	8445	191	36.1
0	FS-4	11870	132	24.8

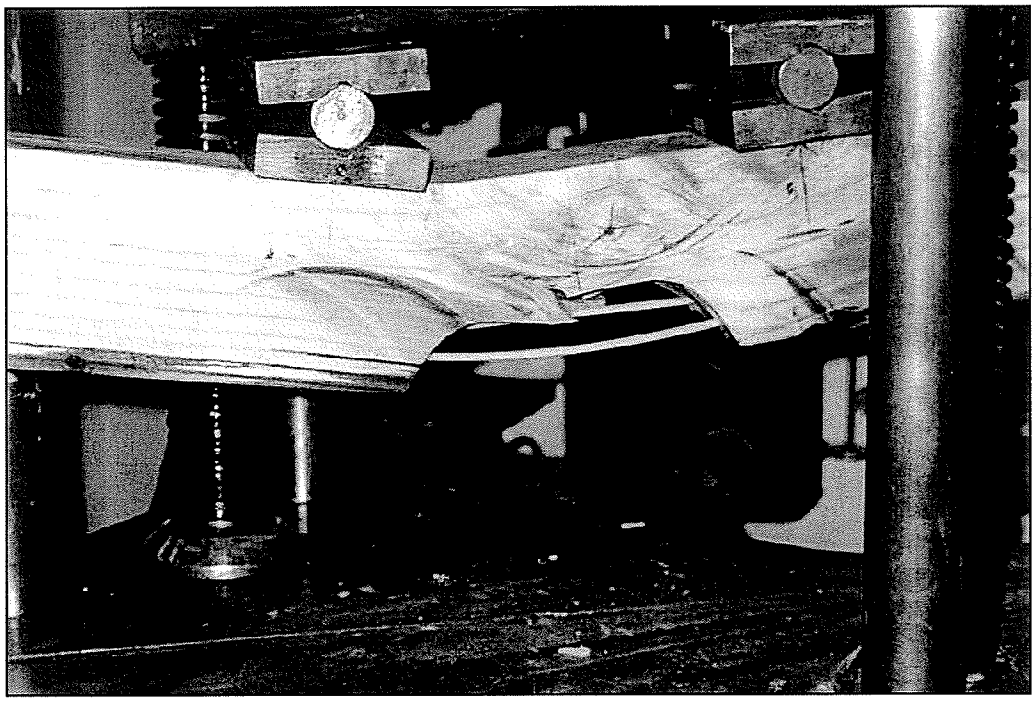

Figure 4.1 – Typical failure of bond specimen

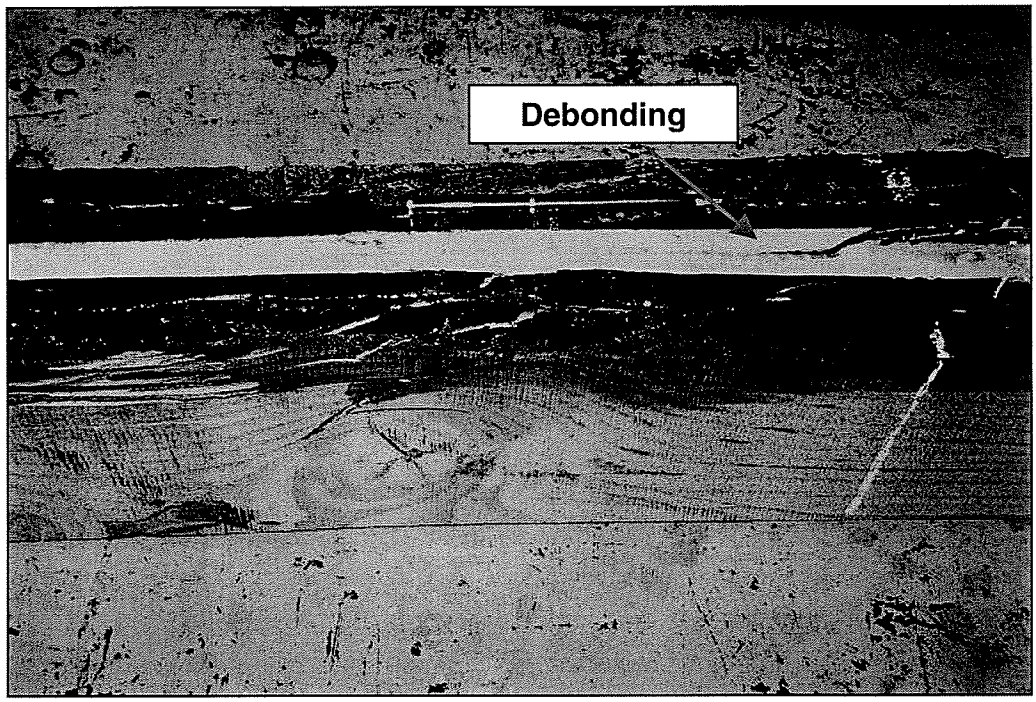

Figure 4.2 – Debonding of coated C-BAR™

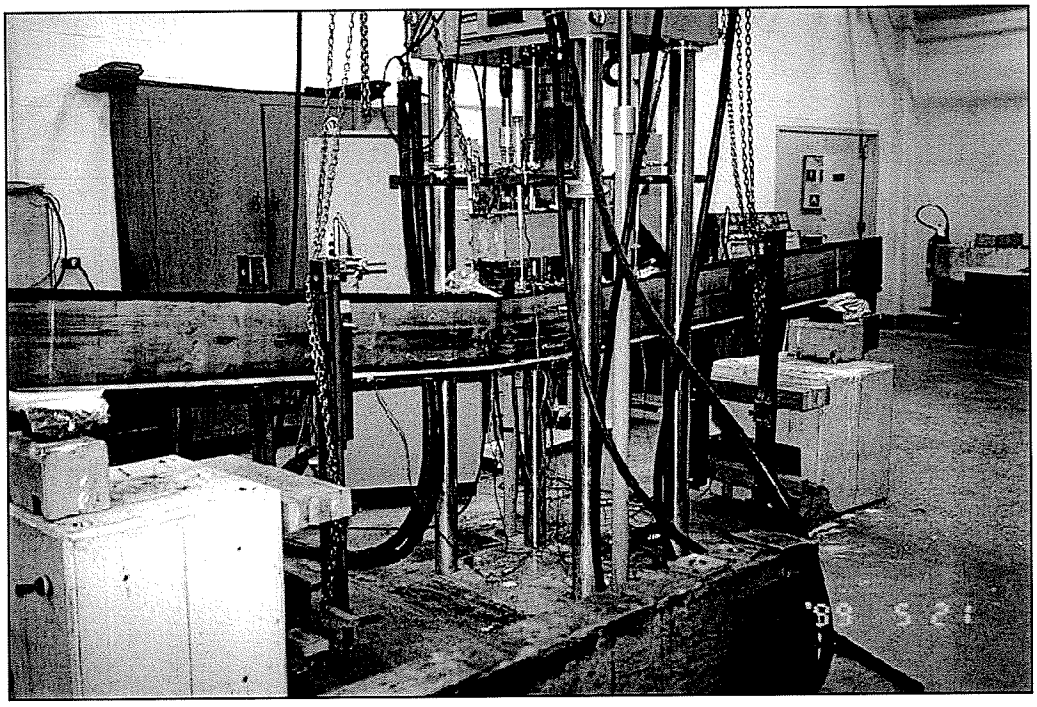

Figure 4.3 – Typical half-scale beam at failure

Figure 4.4 – Typical compression-flexural failure mode

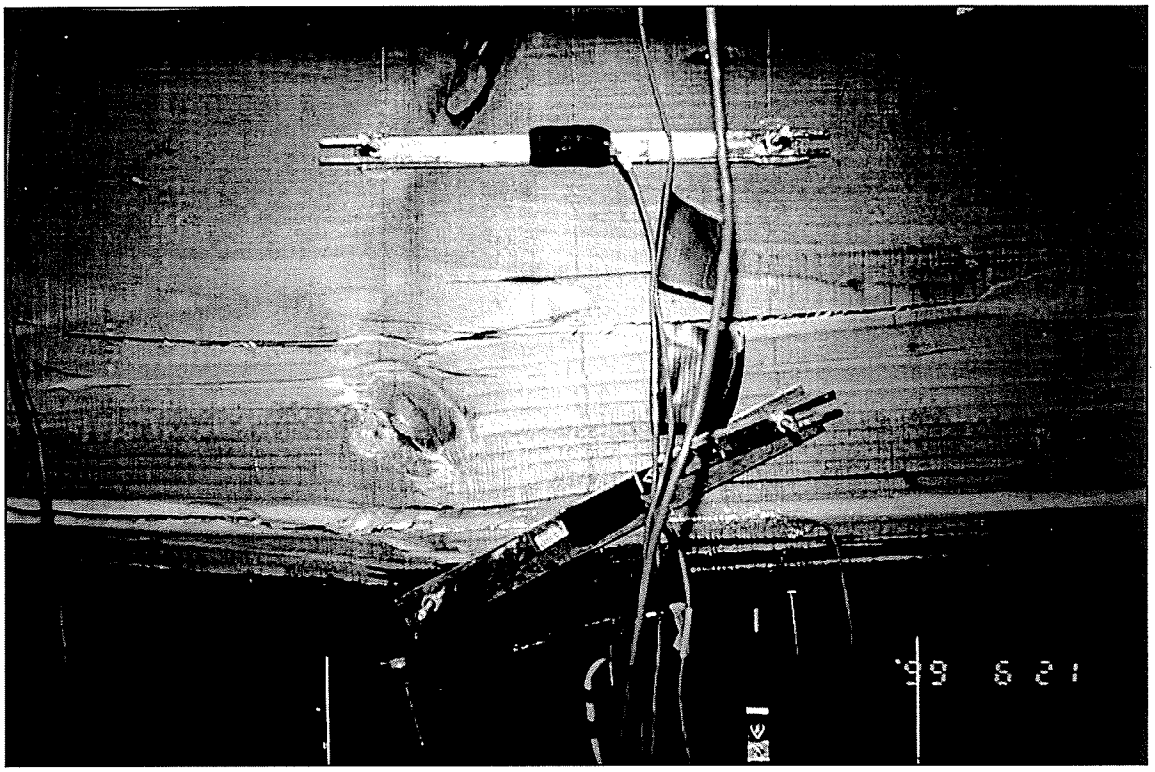

Figure 4.5 – Typical tension-flexural failure mode

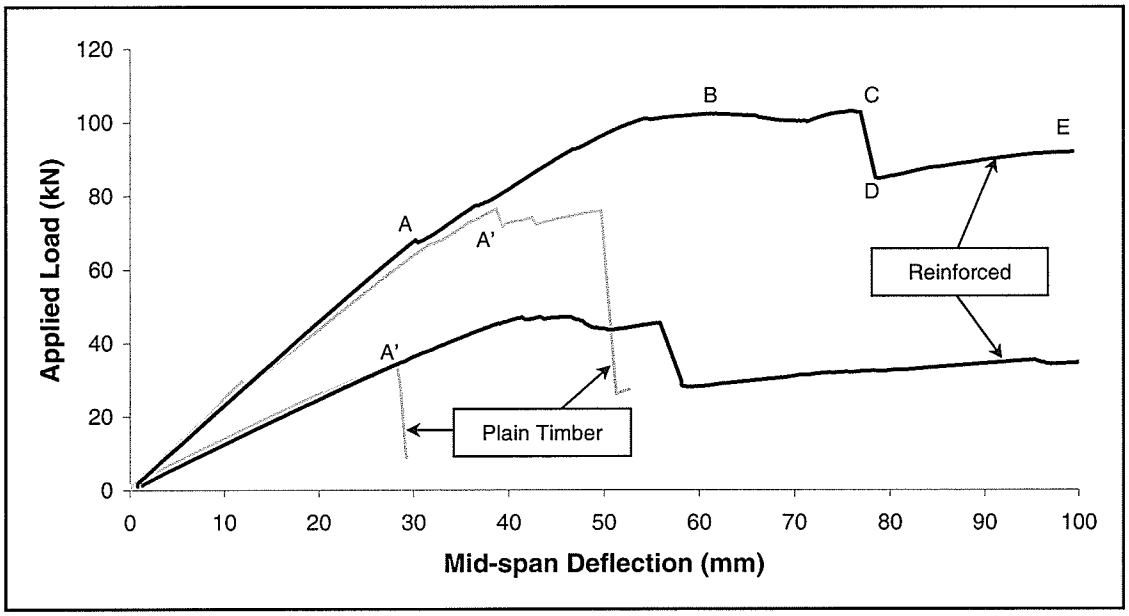

Figure 4.6 – Typical load-deflection curves of half-scale beams

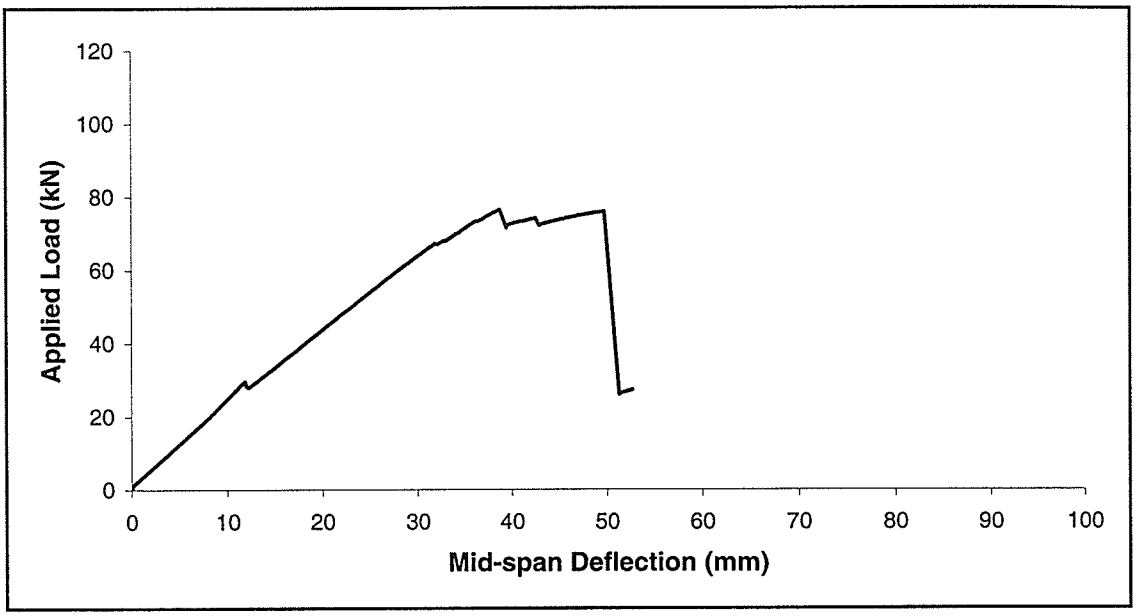

Figure 4.7(a) – Load-deflection curve for Beam G1 (plain timber)

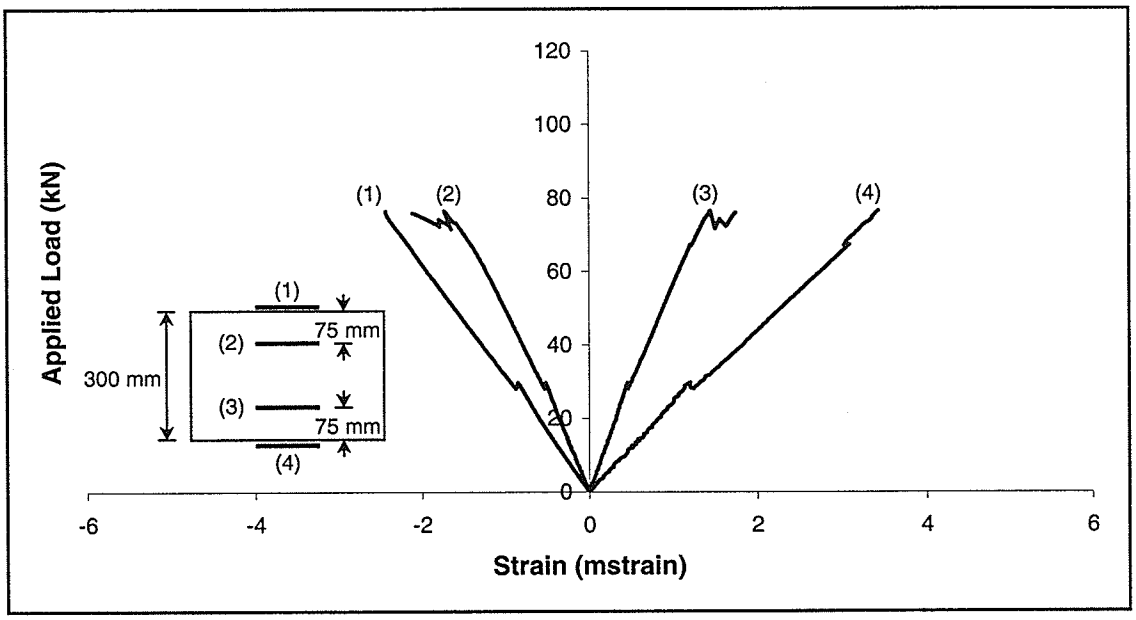

Figure 4.7(b) – Load-strain curves for Beam G1 (plain timber)

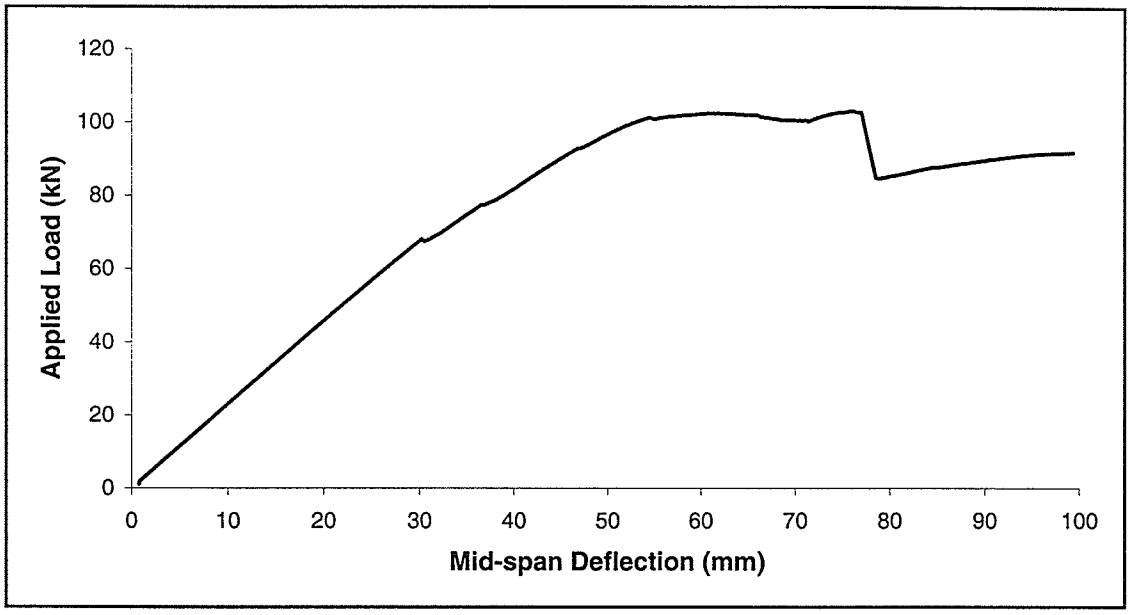

Figure 4.8(a) – Load-deflection curve for Beam I2 (ρ_{GF} = 0.82%)

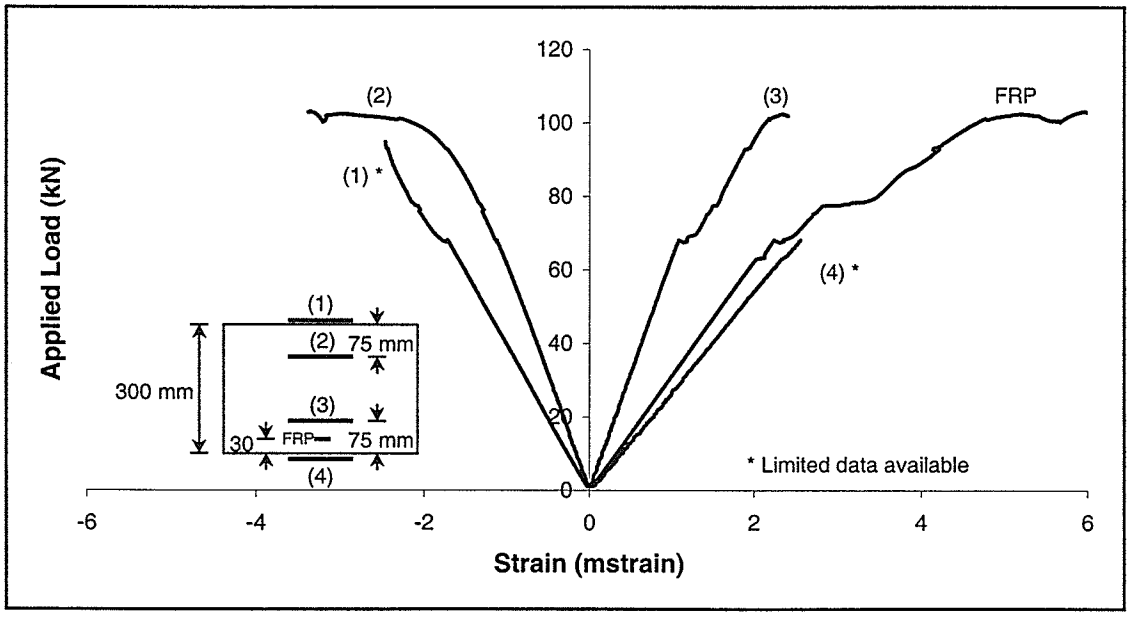

Figure 4.8(b) – Load-strain curves for Beam I2 (ρ_{GF} = 0.82%)

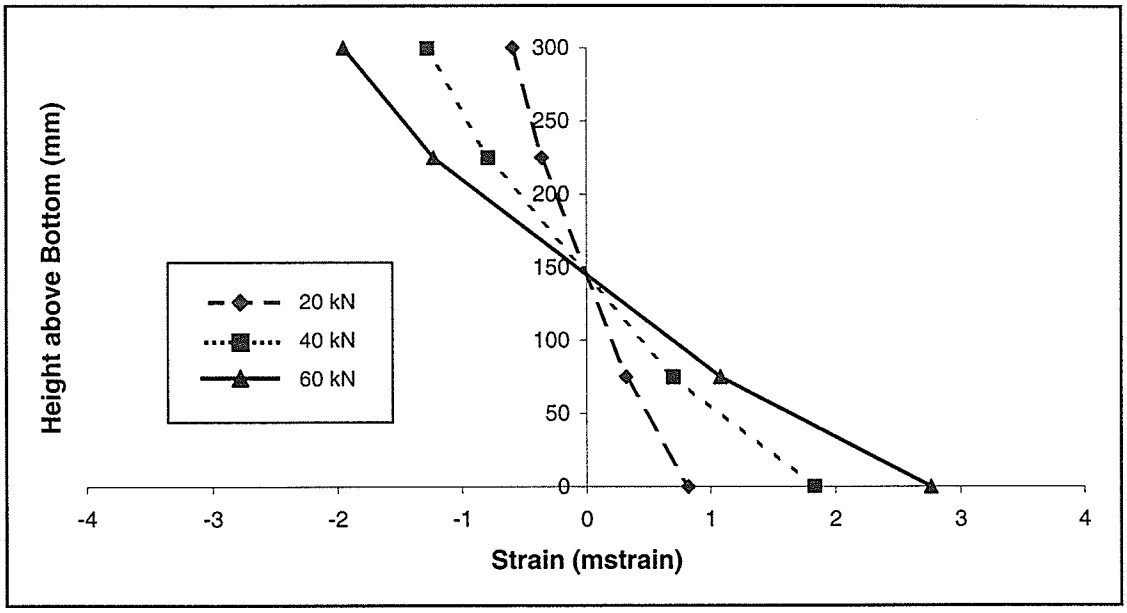

Figure 4.9 – Strain profile of Beam G1 (plain timber)

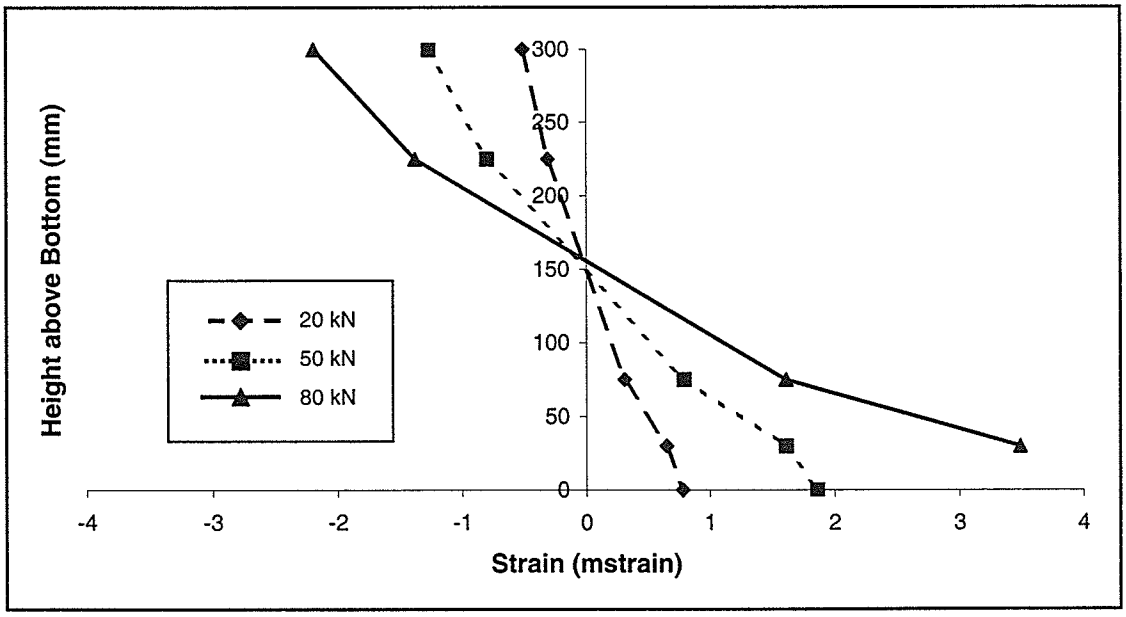

Figure 4.10 – Strain profile of Beam I2 (ρ_{GF} = 0.82%)

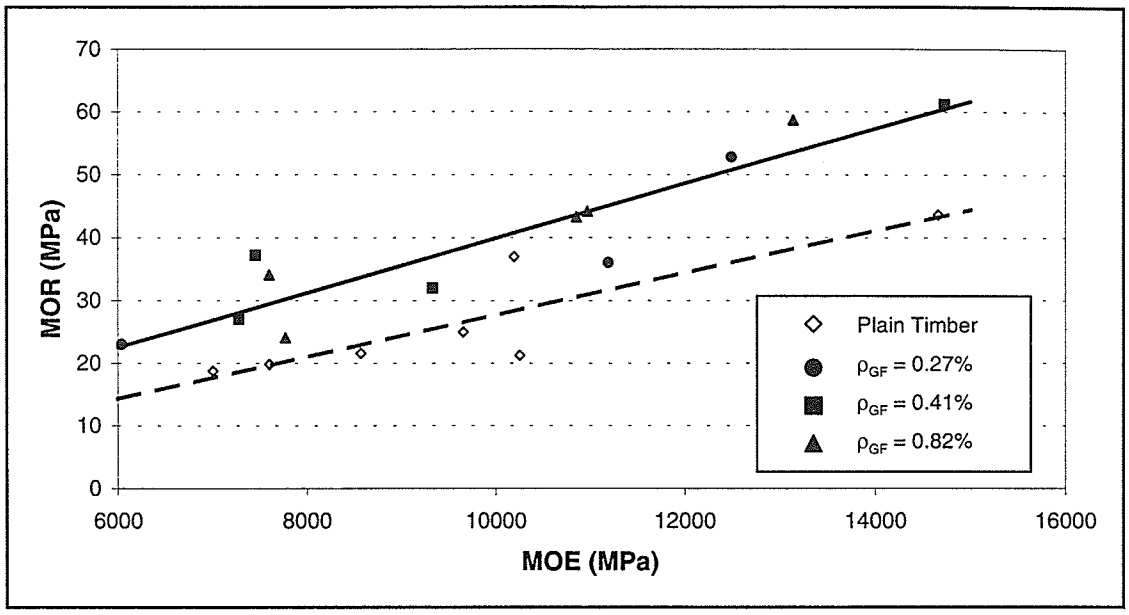

Figure 4.11 – Experimental MOR versus MOE for half-scale beams

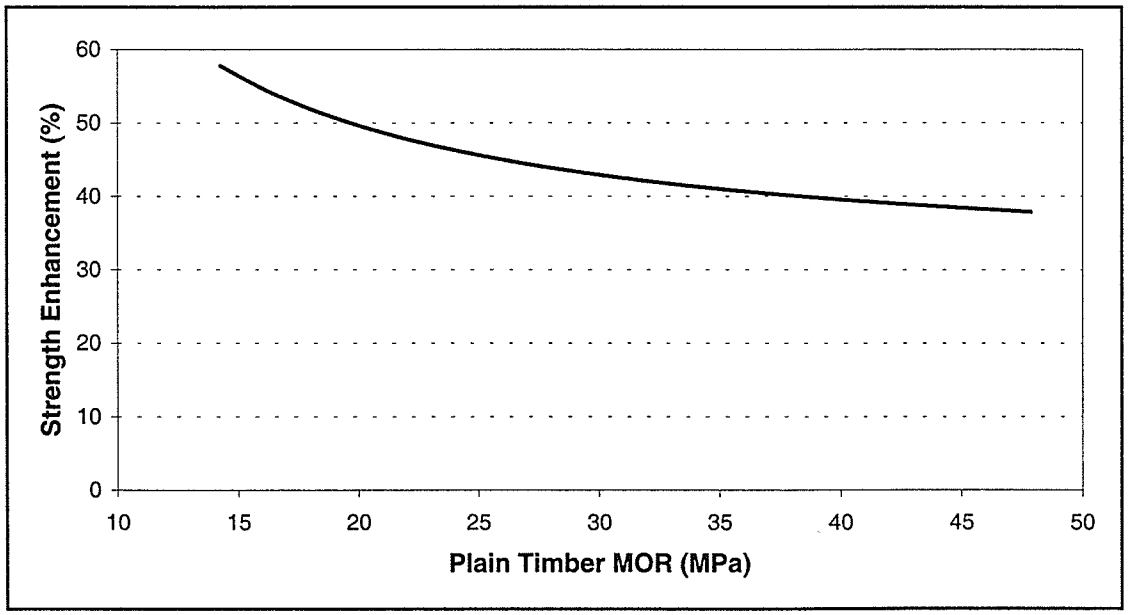

Figure 4.12 – Experimental strength enhancement of GFRP-strengthened beams

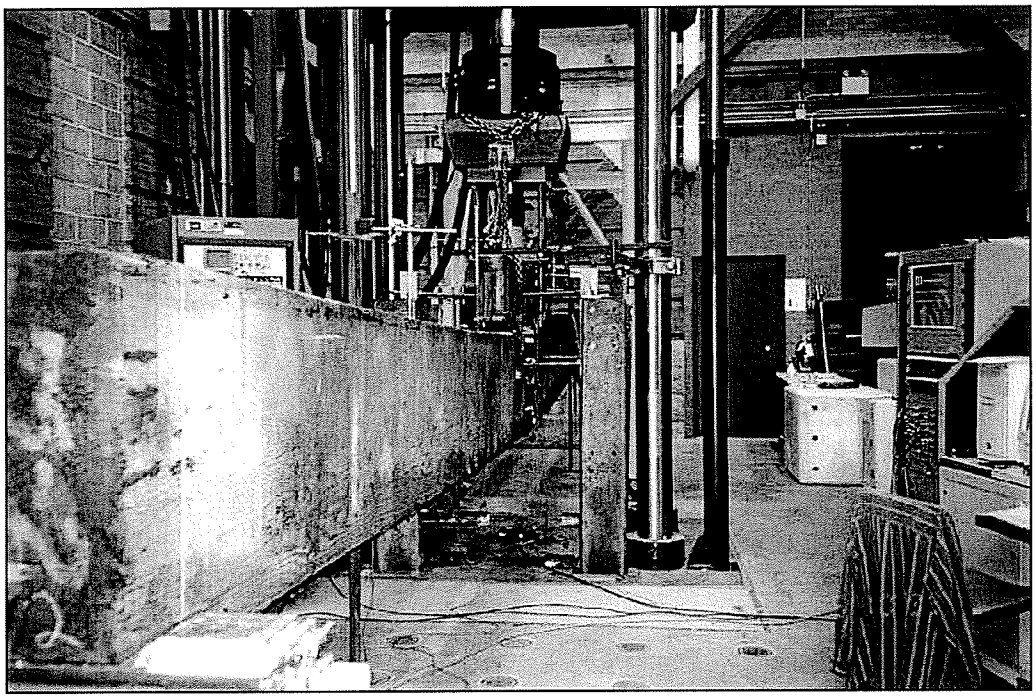

Figure 4.13 – Beam FS-2 at failure

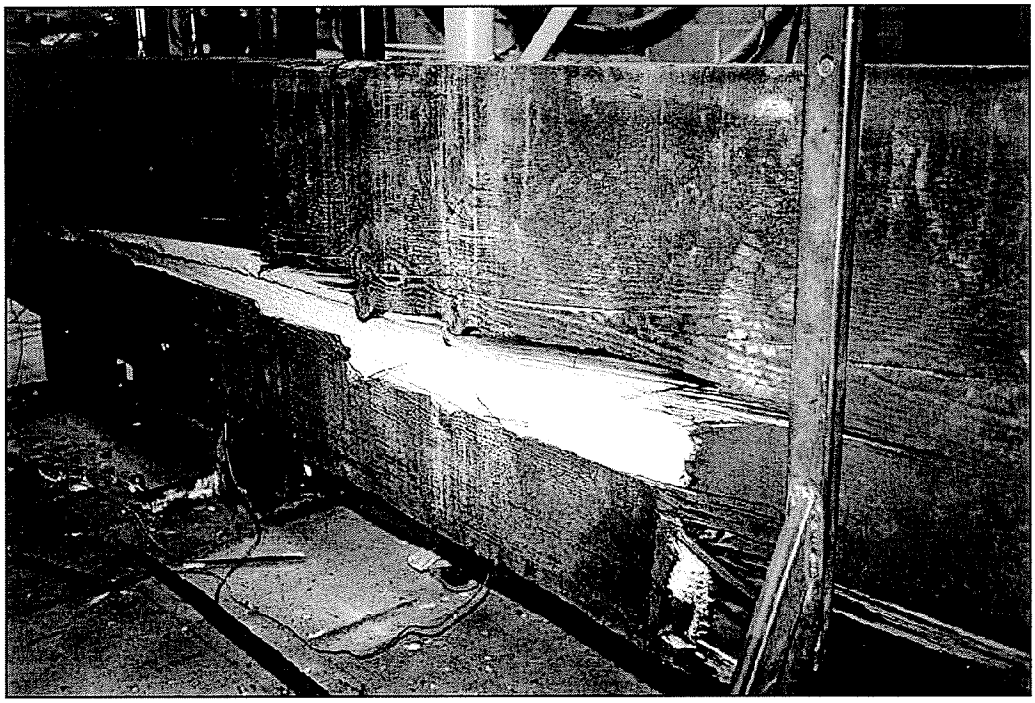

Figure 4.14 – Tension failure of Beam FS-1

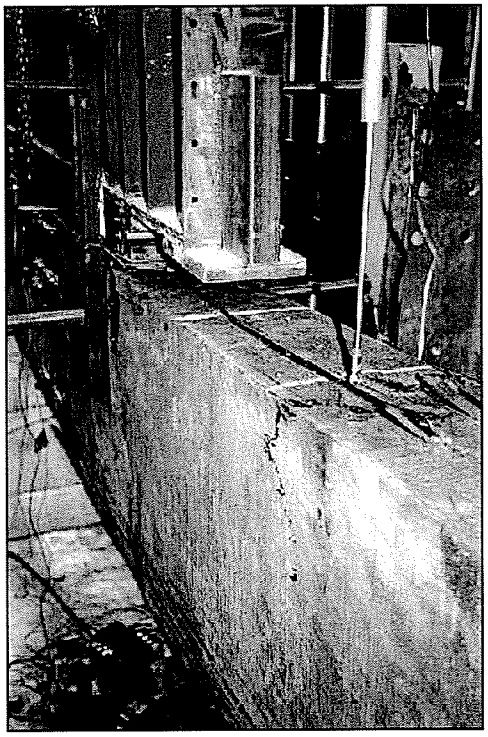

Figure 4.15 – Compression failure of Beam FS-2

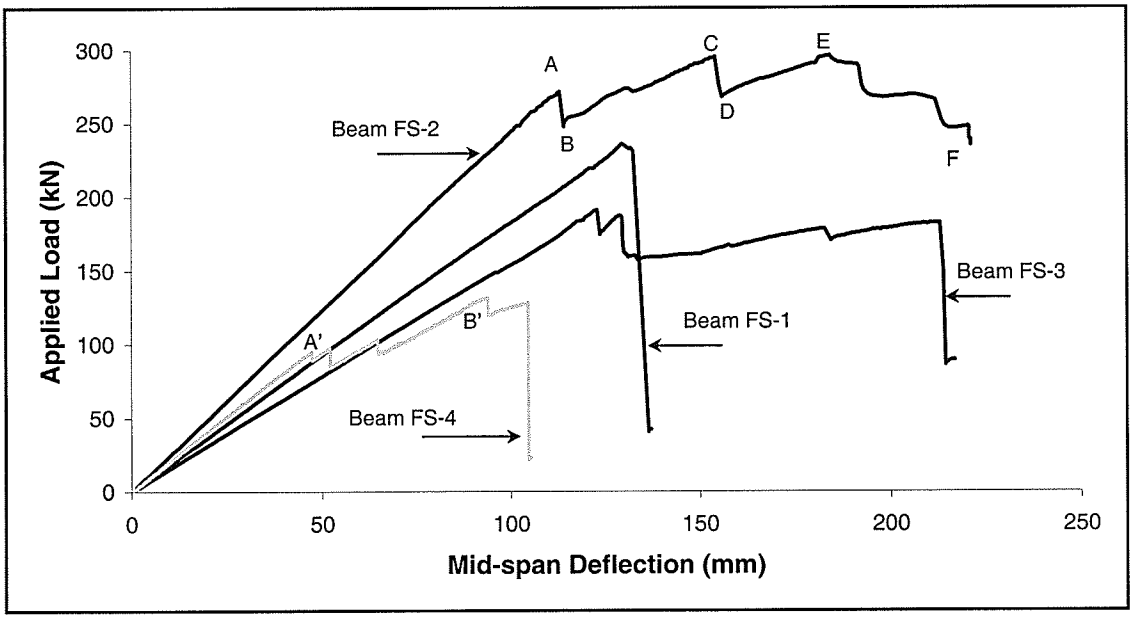

Figure 4.16 – Load-deflection curves of full-scale beams

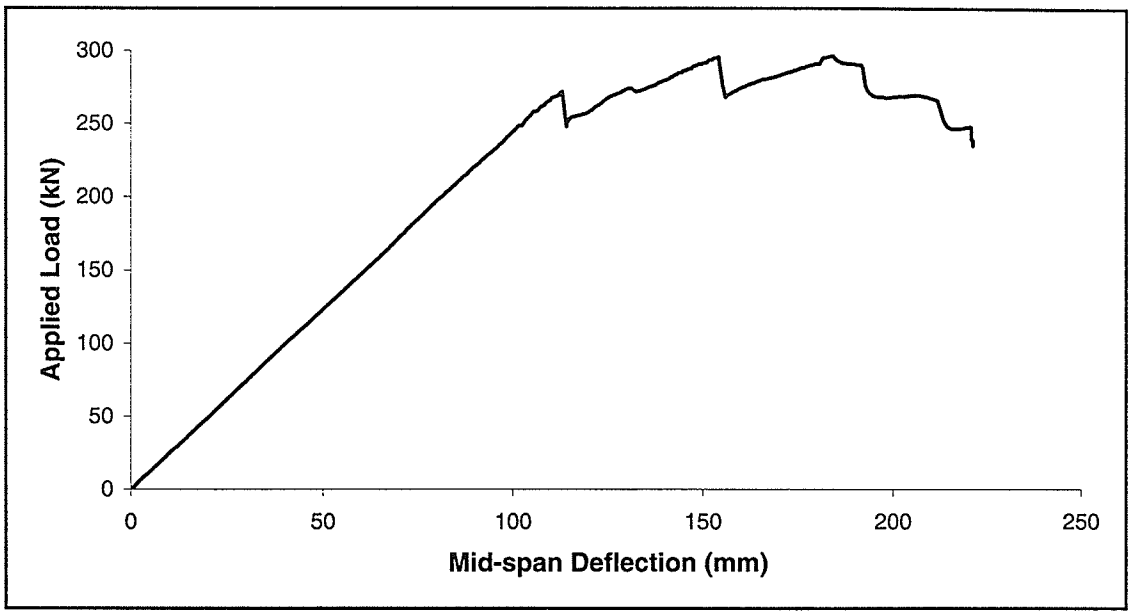

Figure 4.17(a) – Load-deflection curve for Beam FS-2 (ρ_{GF} = 0.26%)

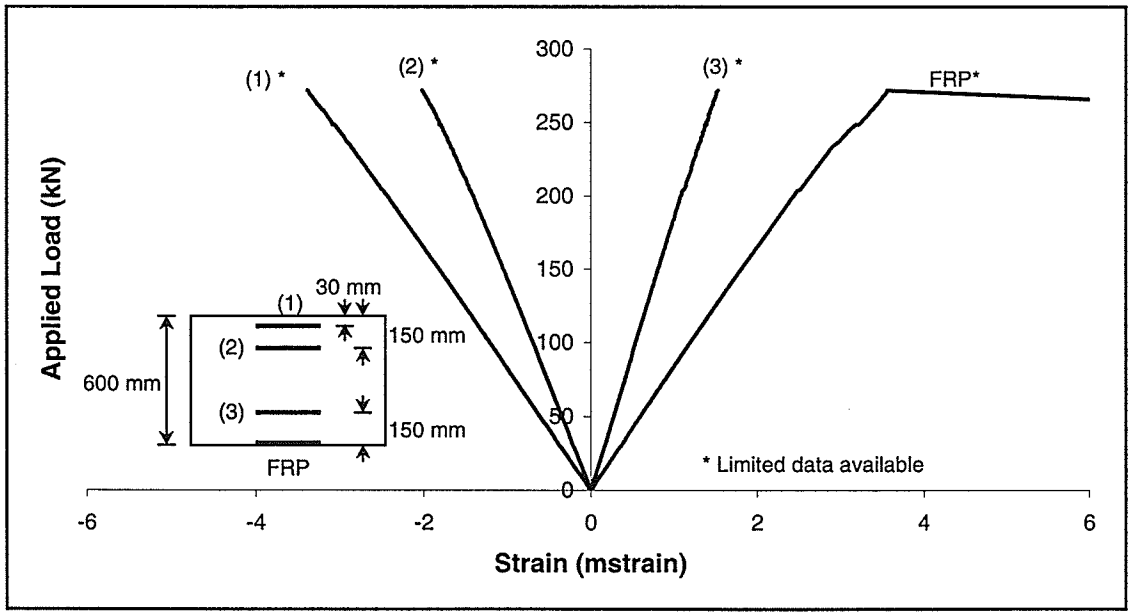

Figure 4.17(b) – Load-strain curves for Beam FS-2 (ρ_{GF} = 0.26%)

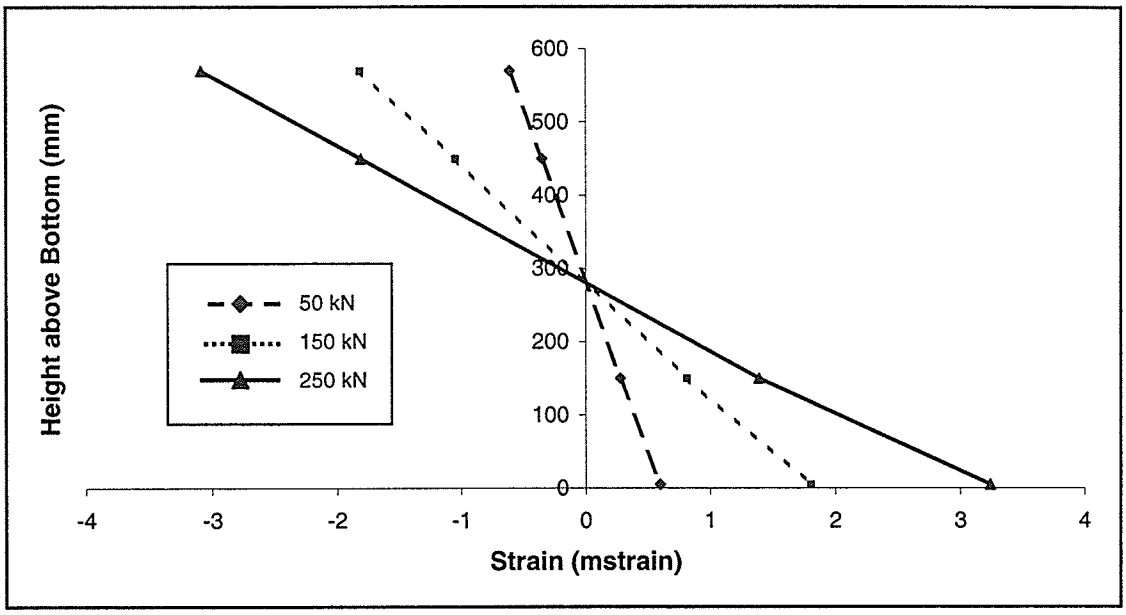

Figure 4.18 – Strain profile of Beam FS-2 (ρ_{GF} = 0.26%)

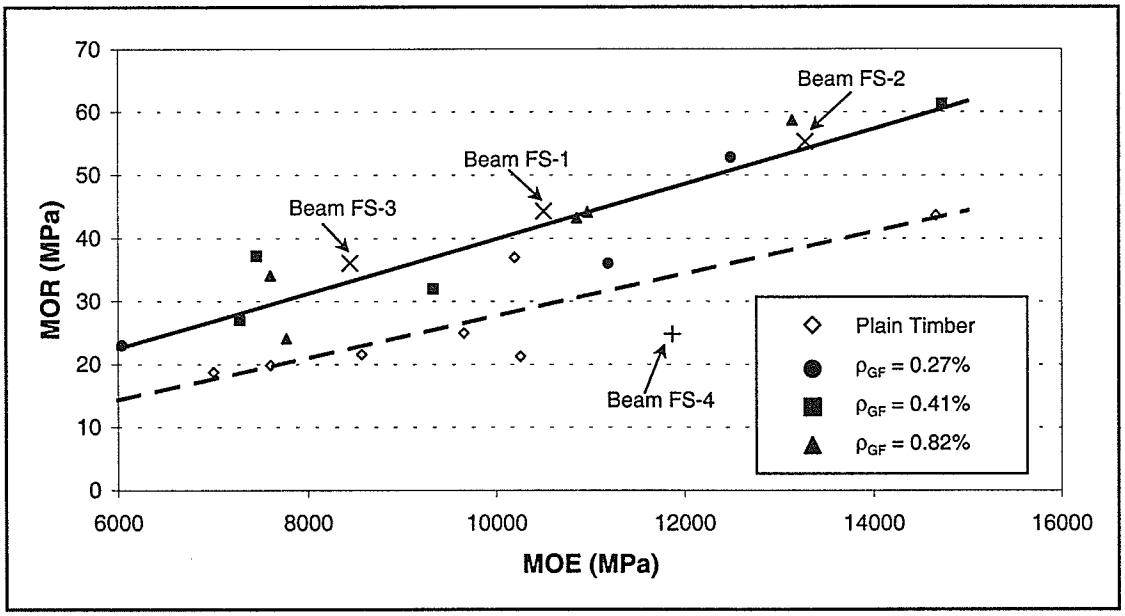

Figure 4.19 – Experimental MOR versus MOE for all beams

CHAPTER 5

ANALYTICAL MODELS FOR BENDING STRENGTH OF PLAIN AND REINFORCED TIMBER

5.1 GENERAL

Following the work of Plevris and Triantafillou (1992), the analytical model presented by Buchanan (1990) was used to predict the bending strength of the plain and reinforced timber beams. The model is first calibrated for plain timber using the experimental data from the half-scale specimens presented in Chapter 4. A modification to the model is presented and the modified model is calibrated using the experimental data from the half-scale reinforced specimens. The effect of varying the FRP reinforcement ratio is evaluated using the modified model. A comparison of the model predictions and experimental results for the full-scale reinforced beams is presented.

5.2 ANALYTICAL MODEL FOR BENDING STRENGTH OF PLAIN TIMBER

The modeling of bending strength of timber is a complex problem. When timber is tested in bending, weak pieces of timber will fail due to tension, while failure of strong pieces of timber will be initiated by wrinkling of the fibres in the compression zone. For pieces

that fail in bending due to tension, the bending strength is always greater than the uniaxial tensile strength. The strongest pieces of timber can be more than twice the strength of the weakest pieces for any given species. Figure 5.1 shows the typical shape of the distribution of timber strengths.

Buchanan (1990) developed an analytical model to predict the bending strength of commercial timber from the compression and tension strengths of members of the same size as the bending member. The model is most useful for predicting the bending strength at specified levels of the strength distribution, such as the fifth and fiftieth percentile. In order to predict the strength of an individual member, the location within the strength distribution, or percentile rank, of the member must be determined. The assumptions made by Buchanan (1990) with respect to stress-strain behaviour of timber and size effects are described below. The method used to calculate the percentile rank and input strengths for the model and the calculation procedure for the model are presented. The model is calibrated using the data from the plain timber half-scale specimens presented in Chapter 4.

5.2.1 Idealized Stress-Strain Behaviour

Bazan (1980) studied the relationship between tension, compression, and bending strengths for clear wood. He proposed an idealized stress-strain relationship for wood with a bilinear relationship to represent the compression behaviour. Buchanan (1990) modified this relationship slightly and used it to predict the bending strength of commercial timber. The stress-strain relationship used by Buchanan is shown in Figure 5.2. Tension behaviour is assumed to be linear elastic, and failure occurs when the stress

reaches the ultimate tensile strength f_{tu}. A bi-linear relationship is assumed for the compression behaviour, with a linear part up to maximum compression strength f_{cu}, and a corresponding strain ε_y. The slope of the descending branch is a fraction, m, of the modulus of elasticity of the timber, E_w, as shown in Figure 5.2. Bazan assumed that m varied with the depth of the neutral axis, while Buchanan assumed that m is a constant.

5.2.2 Size Effects

Madsen and Buchanan (1986) followed the work of Bohannan (1966) and applied Weibull's (1939) brittle fracture theory to commercial timber. They noted some difficulty in the application of brittle fracture theory to commercial timber since timber strength tends to be dominated by a small number of large defects whereas wood strength is dominated by a large number of small defects. The effect of member length and depth was quantified using brittle fracture theory:

$$\frac{x_1}{x_2} = \left(\frac{L_2}{L_1}\right)^{1/k_1} \tag{5.1}$$

$$\frac{x_1}{x_2} = \left(\frac{d_2}{d_1}\right)^{1/k_2} \tag{5.2}$$

where
x_1 = strength of member of length L_1 or depth d_1
x_2 = strength of member of length L_2 or depth d_2
k_1 = length effect parameter
k_2 = depth effect parameter

The parameters k_1 and k_2 reflect the variation in strength between members of different lengths and depths, respectively. Brittle fracture is primarily a bending and tension phenomenon, but Buchanan (1984) also found evidence for the size effect on the compression strength. The influence of the size effect is different for bending, tension and compression; therefore, k_1 and k_2 will have different values for each property. Similar expressions were also developed for the width effect; however, Madsen and Buchanan (1986) could find no conclusive results to support the effect of the width on timber strength.

The load configuration also affects timber strength, since the stressed length depends on the load arrangement. Madsen and Buchanan (1986) quantified the load configuration effect by converting the type of loading to an equivalent stressed length. For the simply supported beam shown in Figure 5.3, subjected to two symmetrical loads, the equivalent stressed length, L_e, can be calculated by:

$$L_e = \frac{1+\frac{a_1 k_1}{L}}{k_1+1} L \tag{5.3}$$

where
L_e = equivalent stressed length
L = span of the beam
a_1 = distance between symmetrically placed loads
k_1 = length effect parameter

Another important factor affecting the bending strength of wood is the stress distribution effect, which accounts for the extreme fibre tension stress at failure being greater in a

bending test than in an axial tension test. Madsen and Buchanan (1986) quantified the stress distribution effect using the brittle fracture theory. For a typical timber cross-section shown in Figure 5.4(a), the tensile strength in axial tension, f_{tu}, shown in Figure 5.4(b) is smaller than the tensile strength achieved in bending, f_m, shown in Figure 5.4(c). The tensile strength in bending is related to the axial tension strength as follows:

$$f_m = \left(\frac{k_3 + 1}{c} \right)^{1/k_3} f_{tu} \tag{5.4}$$

where
f_m = extreme fibre tension strength in bending
f_{tu} = extreme fibre tension strength in axial tension
c = height of the neutral axis as a ratio of the depth d
k_3 = stress distribution parameter

For all of the different size effects, the shape parameter, k, is related to the variability in strength properties. The coefficient of variation, *cov*, can also be used to characterize the variability in strength properties. Madsen and Buchanan (1986) gave the following simple but good approximation:

$$cov = k^{-0.922} \tag{5.5}$$

From equation (2.6) it can be seen that as the parameter k increases, the *cov* decreases.

5.2.3 Determination of f_{cu} and f_{tu}

Published data from the Canadian Wood Council's (CWC) Lumber Properties Research Project (Barrett and Lau, 1994) was used to determine the input values of f_{cu} and f_{tu}. This CWC project summarized and analyzed the data from thousands of full-size structural tests of commercial lumber with sizes ranging from "2x4" to "2x10". The CWC data was given as parameter-estimates for four different statistical distributions: normal, lognormal, two-parameter Weibull, and three-parameter Weibull distributions. Due to the small number of specimens in the experimental program described in Chapter 4, a statistical distribution could not be fit to the data. A method for locating the position of the experimental data within the distribution of strengths was required to determine the appropriate input strengths for the model.

The CWC project also published point-estimates of the mean and fifth percentile values of modulus elasticity. For the determination of input strengths, it was assumed that the modulus of elasticity values of the timber followed a normal distribution. Barrett and Lau (1994) state that the normal distribution fits modulus of elasticity data well. Using the point-estimates of the mean and fifth percentile modulus of elasticity from the CWC data, the standard deviation and the percentile rank for each beam specimen was determined based on the calculated modulus of elasticity from the experimental data. The calculated percentile rank gave the location within the strength distribution for each beam specimen.

The input strengths for the model were selected from the three-parameter Weibull distributions for the tension and compression strengths of Douglas Fir select structural

grade "2x10" dimension lumber. Size effects had to be considered due to the difference in length and depth of the beams between the CWC project and the experimental program. The CWC strengths were corrected for size effects using Equations (5.1) and (5.2):

$$f_{cu} = \text{UCS}\left(\frac{L_{\text{UCS}}}{L_{ec}}\right)^{1/k_1}\left(\frac{d_{\text{UCS}}}{d}\right)^{1/k_2} \tag{5.6}$$

$$f_{tu} = \text{UTS}\left(\frac{L_{\text{UTS}}}{L_{et}}\right)^{1/k_1}\left(\frac{d_{\text{UTS}}}{d}\right)^{1/k_2} \tag{5.7}$$

where
UCS = compression strength from CWC data
UTS = tension strength from CWC data
L_{UCS}, L_{UTS} = characteristic length for UCS and UTS
d_{UCS}, d_{UTS} = characteristic depth for UCS and UTS
L_{ec}, L_{et} = equivalent stressed length in compression and tension
d = depth of modeled section
k_1, k_2 = size effect parameters for length and depth

The equivalent stressed lengths, L_{ec} and L_{et}, were calculated using Equation (5.3). Table 5.1 summarizes the size effect parameters determined by the CWC Lumber Properties Project. The CWC project used beams with depths ranging from 89-mm to 235-mm, but it was assumed that the calculated size effects would apply to beams with depths greater than 235-mm.

The steps used to calculate f_{cu} and f_{tu} are summarized below:

1. Calculate modulus of elasticity, E_w, for each beam specimen.
2. Determine the percentile rank, P_n, for each beam based on E_w.
3. Calculate UCS and UTS from CWC data for each P_n.
4. Calculate L_{ec} and L_{et} for each beam using Equation (5.3).
5. Calculate f_{cu} and f_{tu} using Equations (5.6) and (5.7).

5.2.4 Calculation Procedure

The following quantities are required as inputs for the model:

b = width of the section
d = depth of the section
E_w = modulus of elasticity of the timber
f_{cu} = compressive strength of the timber
f_{tu} = tensile strength of the timber
k_3 = stress distribution parameter
m = slope of the falling branch in compression

The modulus of elasticity, E_w, was determined from the load-deflection behaviour of the beam specimens. The slope of the descending branch, m, was measured from small compression tests of the timber material. The average value of m for the select structural grade Douglas Fir, used in the timber stringers under consideration, was found to be 0.167. The calculation steps of the model are described below.

Strain compatibility was used for the analysis of the beam specimens. The tensile strength in bending, f_m, was calculated using Equation (5.4) for each beam assuming that $c = 0.5$. The strain at the extreme tension fibre, ε_t, was increased until the extreme fibre tensile stress, f_t, reached f_m. If the extreme fibre compressive stress, f_c, reached the maximum compression strength, f_{cu}, before f_t reached f_m, yielding occurred, the neutral axis shifted downwards, and the tensile strength in bending f_m was recalculated with the new value of c.

The distributions of strain and stress for a rectangular beam, shown in Figure 5.5(a), subjected to a moment sufficient to cause yielding are shown in Figures 5.5(b) and 5.5(c), respectively. Plane sections will remain plane after deformation as shown in Figure 5.5(b). The tensile stress distribution is triangular and the compressive stress distribution is trapezoidal with maximum compressive stress f_{cu} corresponding to compressive strain ε_y. For compressive strains greater than ε_y, the compressive stress is less than f_{cu} as shown in Figure 5.2. The compressive stress at the extreme fibres of the section is a fraction r of f_{cu}. The quantities a, b, and r shown in Figure 5.5(c) can be calculated using the geometry of the section and idealized stress-strain curve shown in Figure 5.2 for a given combination of ε_t and c.

The strain compatibility analysis was performed until failure occurred when f_t reached f_m. Buchanan (1990) described four possible failure modes for timber in bending.

Mode 1

For material that is weak in tension, the induced tensile stress, f_t, reaches the failure strength in bending, f_m, before the induced compressive stress, f_c, reaches the maximum compressive strength, f_{cu}, of the timber. This type of failure can be classified as simple tension failure. The bending strength, or modulus of rupture, is f_m.

Mode 2

For material with an intermediate ratio of tension to compression strength, f_c reaches f_{cu} before f_t reaches f_m. In this case, compressive stresses in the compression zone start to yield, causing a shift of the neutral axis towards the tension zone. Failure occurs when f_t reaches f_m and the failure will be more ductile in comparison to Mode 1.

Mode 3

For material with a high ratio of tension to compression strength, maximum bending strength is governed by the compression strength. The final failure occurs when f_t reaches f_m, but only after the maximum moment has been passed and considerable compression yielding has occurred.

Mode 4

For material that has a very high ratio of tension to compression strength, maximum moment is associated with highly ductile compression yielding, without tension failure.

A simple computer program was written to perform the calculations. A flowchart for the calculation steps is shown in Figure 5.6. The program calculated the bending moment and curvature for each level of extreme fibre tensile strain, ε_t. Maximum bending moment was determined from the moment and curvature data generated by the program. A sample calculation of bending strength using the computer program is included in Appendix B.

5.2.5 Calibration of Model

The analytical model was calibrated with the experimental data for the half-scale plain timber specimens by varying the stress distribution parameter, k_3. A value of k_3 = 10.0 was found to give good calibration. Table 5.2 and Figure 5.7 show a comparison of the experimental and predicted values of modulus of rupture (MOR) using k_3 = 10.0. A detailed comparison of the experimental and predicted MOR for different values of k_3 is included in Appendix C. The predicted values of MOR were calculated in the same manner as the experimental values:

$$MOR = \frac{M_{\max}}{S_g} \tag{5.8}$$

where M_{max} = maximum bending moment from computer program
S_g = section modulus based on gross section properties

5.3 MODIFIED MODEL FOR REINFORCED TIMBER

5.3.1 General

The experimental results presented in Chapter 4 showed a strength increase for the reinforced beams of approximately 30 to 50 percent over the plain timber beams. This level of strength enhancement was also observed by Johns and Lacroix (2000) and is much higher than predicted by a simple strength of materials approach. The FRP reinforcement appears to enhance the tensile strength of the adjacent timber. In the following sections a modification to Buchanan's (1990) model is presented and the modified model is calibrated using the experimental data from the half-scale reinforced beams.

5.3.2 Modifications to the Model

The quantity controlling failure in the model computations is the tensile strength in bending, f_m. The model cannot predict the increase in f_m due to the FRP reinforcement. Equation (5.4) defined f_m:

$$f_m = \left(\frac{k_3 + 1}{c} \right)^{1/k_3} f_{tu}$$

The quantity f_{tu} is the ultimate tensile strength of the timber. FRP-reinforced timber is a different material than plain timber and would have a different strength distribution. An increase in f_{tu} would produce an increase in f_m. The distribution of f_{tu} could be evaluated by tension tests of FRP-reinforced timber.

In the absence of information on the distribution of f_{tu} for FRP-reinforced timber, there are two ways that f_m can increase. A decrease in k_3 produces an increase in f_m, but Equation (5.5) shows that k_3 is inversely proportional to the coefficient of variation. Any decrease in k_3 implies an increase in the coefficient of variation, but past research has shown that the strength of reinforced timber is less variable than strength of plain timber. An increase in f_m can also be produced by the introduction of a modification factor:

$$f_m = \alpha_m \left(\frac{k_3 + 1}{c} \right)^{1/k_3} f_{tu} \tag{5.9}$$

where $\alpha_m > 1.0$

5.3.3 Input Data

For predicting the strength of the reinforced timber sections, the model required the following additional input data (see Figure 5.8):

E_{GF} = modulus of elasticity of the GFRP
s = height of GFRP from the tension fibres as ratio of depth d
ρ_{GF} = GFRP reinforcement ratio
α_m = modification factor for tensile strength

The modulus of elasticity, E_{GF}, was specified by the manufacturer and reported in Section 3.2.2. All of the reinforced beams were prepared with $s = 0.1$.

5.3.4 Calculation Procedure

The computer program developed for the model computations was modified to accommodate the GFRP. Using a transformed section analysis, the initial location of the neutral axis, c, was calculated for each beam before starting the strain compatibility analysis. Figure 5.9 shows the transformed section of a typical reinforced beam. A flowchart for the modified calculation steps is shown in Figure 5.10. Theoretically, failure could be due to rupture of the FRP; however, due to the high strength and large ultimate strain of the FRP used in the experimental program, all failures were governed by the strength of the timber. A sample calculation of bending strength using the computer program is included in Appendix B.

5.3.5 Calibration of Modified Model

The modified analytical model shown in Figure 5.10 was calibrated with the experimental data for the half-scale reinforced timber specimens by varying the modification factor α_m. Calibration of α_m was performed for each reinforcement ratio separately and for all reinforced beams as one group. Table 5.3 shows the calibrated values of α_m. A detailed comparison of the experimental and predicted MOR for different values of α_m is included in Appendix C. From the data in Table 5.3, it appears that α_m increases with increasing reinforcement ratio, but a valid statistical comparison cannot be made due to the small number of specimens. Table 5.4 and Figure 5.11 show a comparison of the experimental and predicted values of MOR for α_m = 1.30. The predicted values of MOR were calculated using Equation (5.8).

5.4 APPLICATION OF THE PROPOSED MODELS

5.4.1 Half-Scale Beams

The analytical models presented in Sections 5.2 and 5.3 were used to predict the strength of plain and reinforced timber, respectively, at multiple levels in the distribution of strength. The predicted values of MOR versus MOE are shown in Figure 5.12 for the plain and reinforced timber. Figure 5.13 shows the calculated strength enhancement versus plain timber MOR for the three reinforcement ratios used in the experimental program.

A number of observations can be made from Figures 5.12 and 5.13. The models predicted a non-linear relationship between MOR and MOE for both the plain and reinforced timber. This differed from the linear relationship assumed during analysis of the experimental data (Figure 4.11). The models gave accurate predictions of strength in the low strength and low stiffness range, which is the range used to determine design strengths. A statistical evaluation of the accuracy of the models could not be made due to the small number of specimens tested.

The predicted strength enhancement shown in Figure 5.13 decreased as the strength of the timber increased. The model predicted a strength increase of between 35 and 46 percent for timber with 20 MPa strength, and a strength increase of between 18 and 21 percent for timber with 70 MPa strength. Johns and Lacroix (2000) observed a similar trend, but with a larger magnitude of strength increase for the weakest timber, as was shown in Figure 2.2. The strength enhancement was not proportional to the amount of reinforcement. Increasing the ratio ρ_{GF} from 0.27 to 0.82 percent increased the strength

enhancement only by approximately 30 percent while the amount of reinforcement was increased three times in magnitude.

5.4.2 Full-Scale Beams

Table 5.5 shows a comparison of the predicted and experimental strengths for the full-scale beams. Beam FS-4 was tested at a much slower loading rate than the other beams, with final failure occurring after two hours. The experimental strength shown in Table 5.5 may be lower than the true short-term strength due to duration of load effects.

It can be seen from Table 5.5 that the experimental strengths for the full-scale reinforced beams were much higher than the strengths predicted by the analytical model. The experimental strengths fit well with the experimental strengths of the half-scale specimens as shown in Figure 4.19. This would suggest an error in the model predictions. The model used the size effect factors presented in Table 5.1 to adjust the CWC strengths to the size of the full-scale beams. These factors were calculated from experimental tests of beams with depths between 89-mm and 235-mm. The rate of change of strength with depth may decrease for depths greater than 235-mm. Thus, the input strengths calculated for the full-scale beams may have been too low. The validity of the model for the full-scale beams cannot be evaluated due to the small number of specimens.

Table 5.1 – Size Effect Parameters

	k_1	k_2
Tension	5.9	4.4
Compression	10.0	9.1

Table 5.2 –Measured versus Predicted MOR for Plain Timber (k_3 = 10.0)

Beam ID	MOE (MPa)	MOR (MPa)		$\frac{MOR_{meas}}{MOR_{pred}}$
		Measured	Predicted	
F1	6999	18.8	18.3	1.03
J1	7602	19.8	19.3	1.02
B1	8568	21.6	21.6	1.00
H1	9654	25.0	25.2	0.99
C1	10197	37.0	27.4	1.35
A1	10257	21.2	27.7	0.77
G1	14662	43.7	54.8	0.80

Table 5.3 –Calibration of α_m

ρ_{GF} (%)	α_m
0.27	1.23
0.41	1.25
0.82	1.34
All Beams	1.30

Table 5.4 –Measured versus Predicted MOR for Reinforced Timber (α_m = 1.30)

ρ_{GF} (%)	Beam ID	MOE (MPa)	MOR (MPa)		$\frac{MOR_{meas}}{MOR_{pred}}$
			Measured	Predicted	
0.27	F2	6039	23.0	23.5	0.98
	D2	11189	36.0	42.1	0.86
	D1	12491	52.8	50.9	1.04
0.41	L1	7274	27.1	26.0	1.04
	K1	7450	37.2	26.2	1.42
	H2	9327	32.0	32.6	0.98
	I1	14724	61.3	68.3	0.90
0.82	L2	7598	34.1	28.5	1.20
	K2	7770	24.1	28.7	0.84
	A2	10855	43.3	42.2	1.03
	G2	10969	44.2	42.9	1.03
	I2	13140	58.7	57.8	1.02

Table 5.5 – Measured versus Predicted MOR for Full-Scale Beams

ρ_{GF} (%)	Beam ID	MOE (MPa)	MOR (MPa)		$\frac{MOR_{meas}}{MOR_{pred}}$
			Measured	Predicted	
0	FS-4	11870	24.8	26.7	0.93
0.42	FS-3	8445	36.1	21.6	1.66
0.42	FS-1	10506	44.3	29.2	1.51
0.26	FS-2	13276	55.3	43.7	1.26

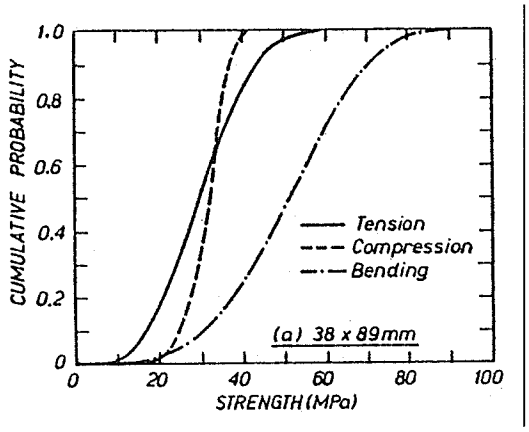

Figure 5.1 – Comparison of bending, tension, and compression strengths from Buchanan (1990)

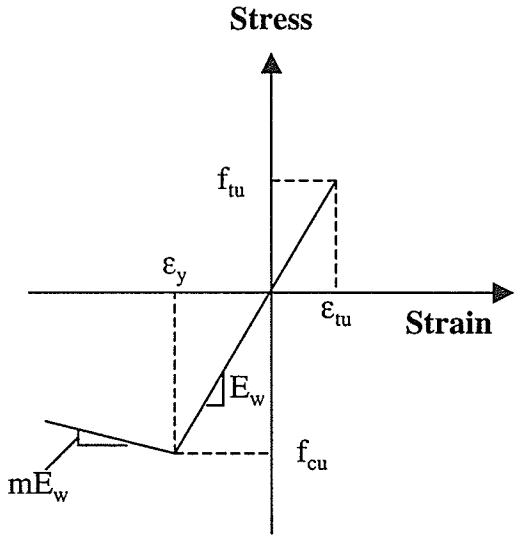

Figure 5.2 – Idealized stress-strain relationship for timber (after Buchanan, 1990)

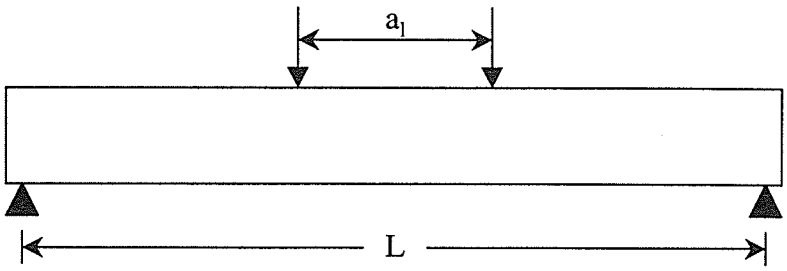

Figure 5.3 – Span and loading of typical beam

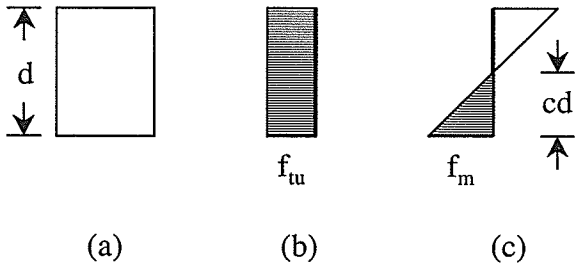

Figure 5.4 – Tension stresses in (a) timber cross-section under (b) uniaxial loading and (c) bending

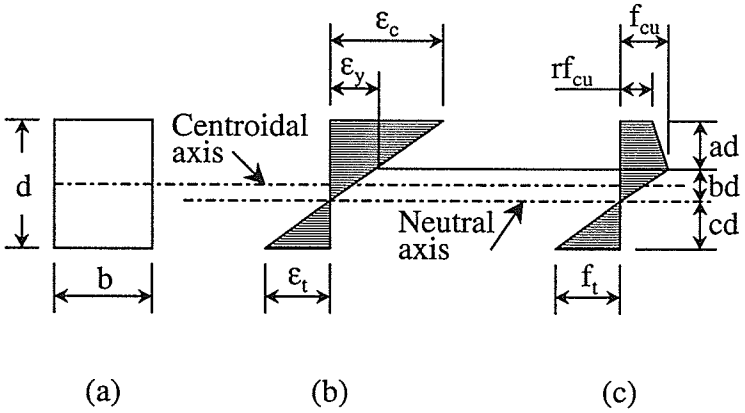

Figure 5.5 – Distribution of stress and strain for bi-linear stress-strain relationship (after Buchanan, 1990)

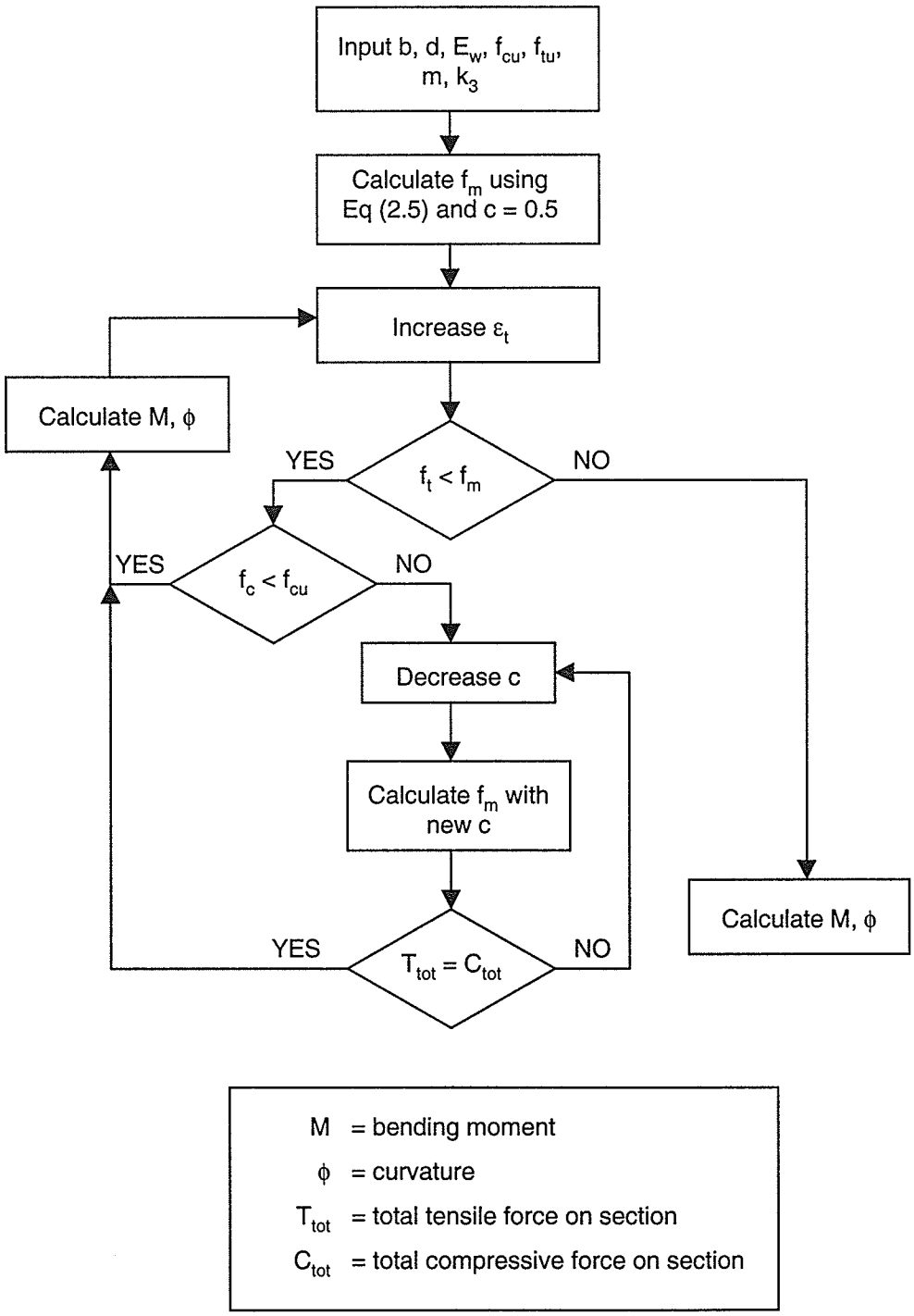

Figure 5.6 – Flowchart for calculating bending strength

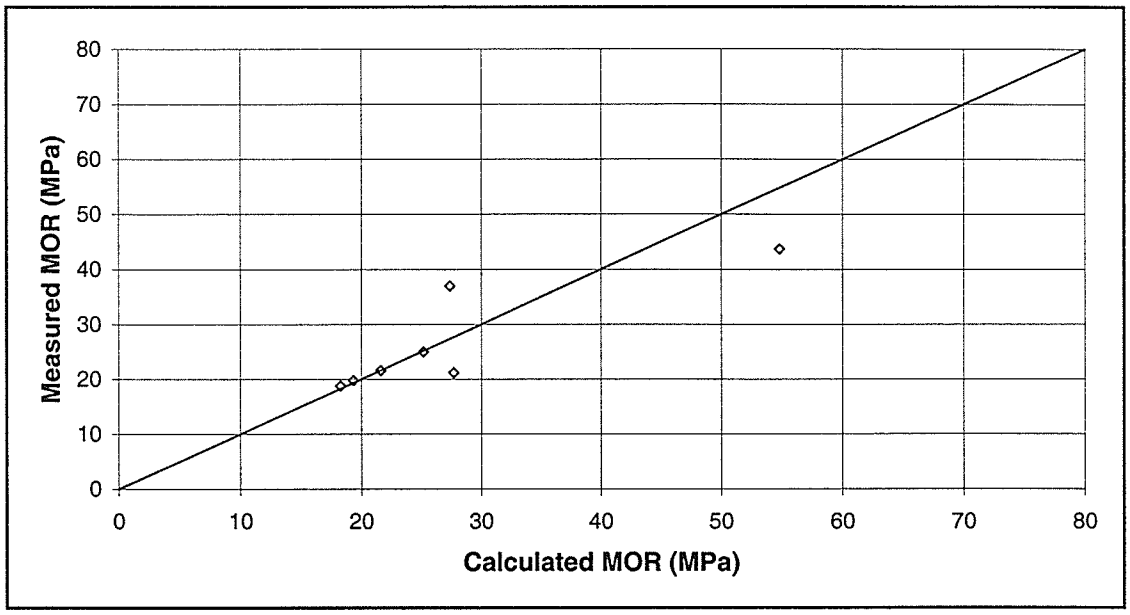

Figure 5.7 – Measured versus calculated MOR for plain timber

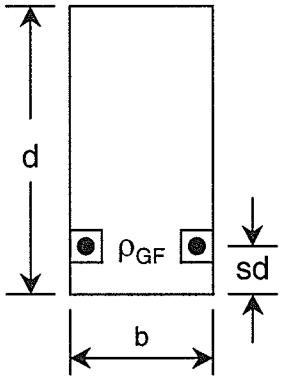

Figure 5.8 – Cross-section of reinforced timber beam

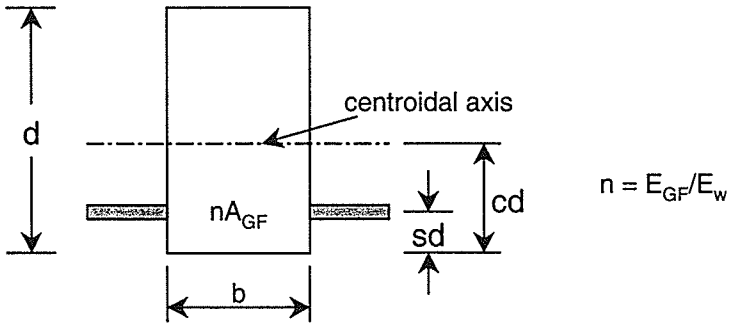

Figure 5.9 – Transformed section of reinforced timber beam

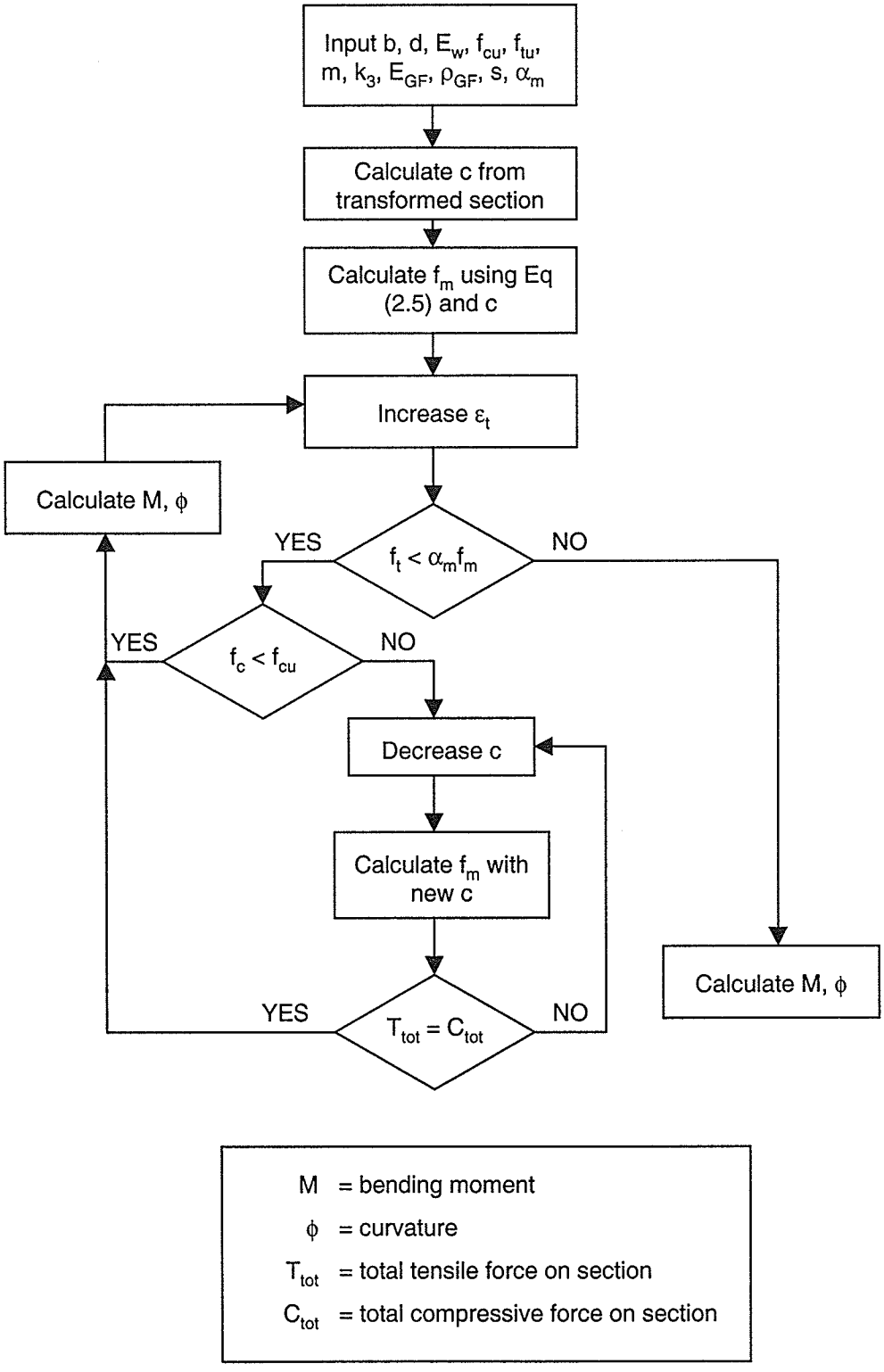

Figure 5.10 – Flowchart for calculating bending strength using modified model

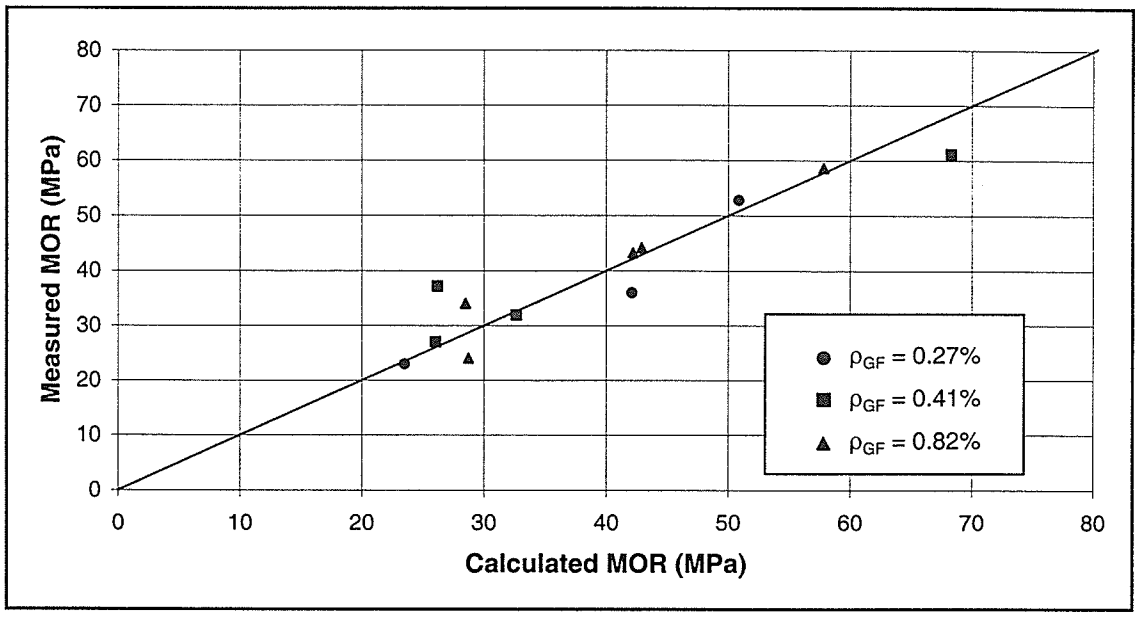

Figure 5.11 – Measured versus calculated MOR for reinforced timber ($\alpha_m = 1.30$)

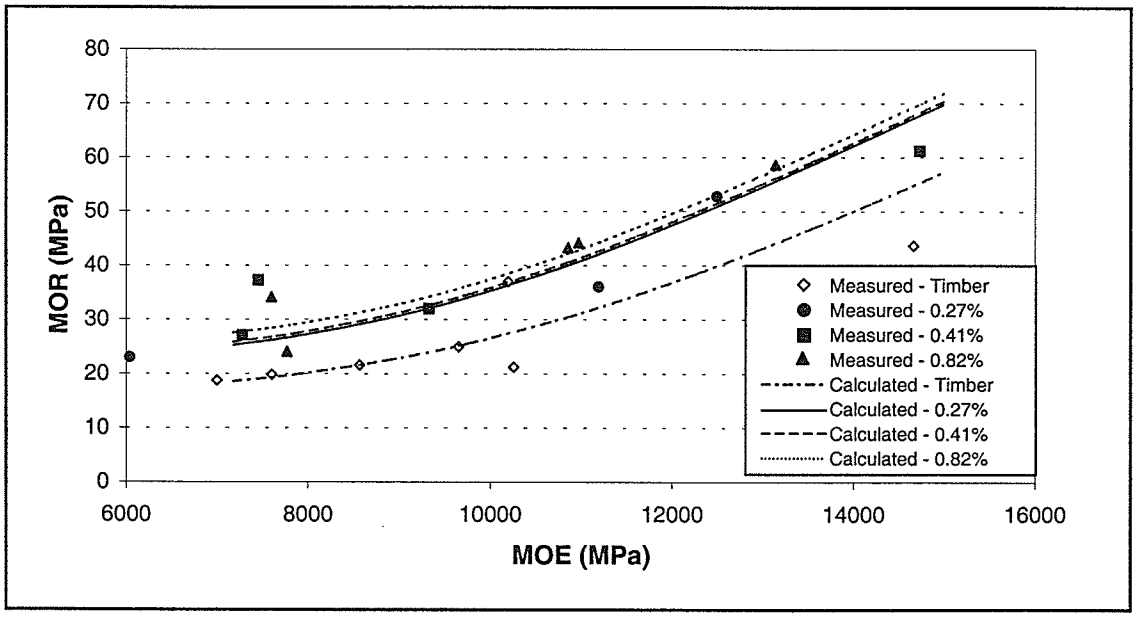

Figure 5.12 – Comparison of measured and calculated MOR

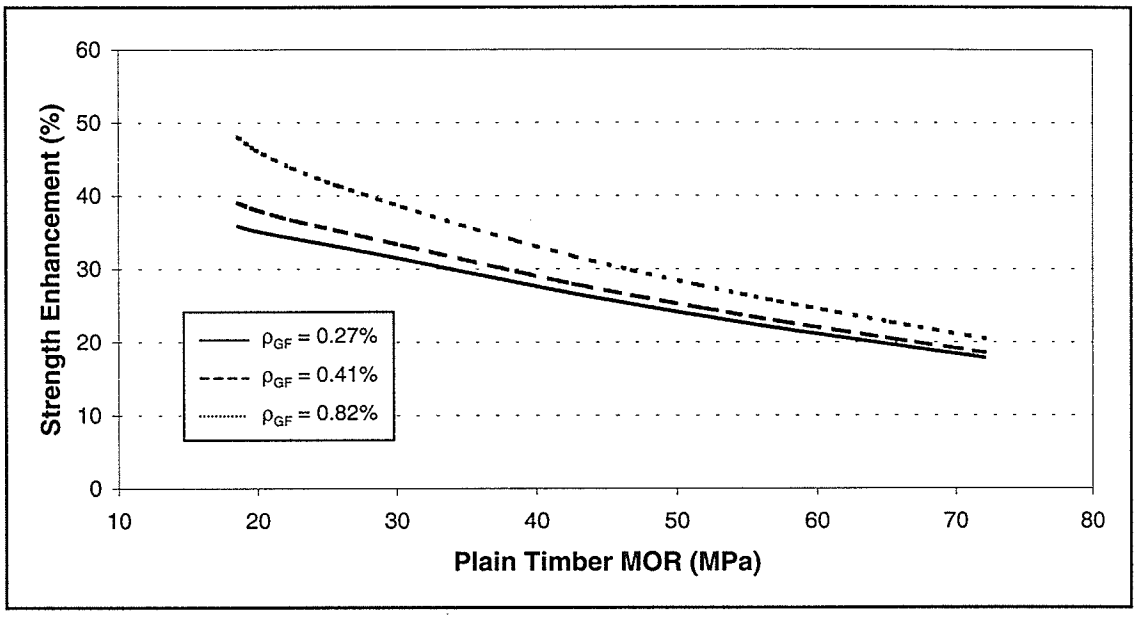

Figure 5.13 – Calculated strength enhancement

CHAPTER 6

SUMMARY AND CONCLUSIONS

6.1 SUMMARY

The use of GFRP bars for flexural strengthening of sawn timber bridge beams was examined by conducting both an experimental investigation and an analytical study. Based on the findings, an analytical model is proposed to predict the bending strength of the GFRP-reinforced timber.

Twenty-two GFRP-reinforced timber beams, 1:2 scale models of typical timber bridge stringers, were tested to failure. Seven of the half-scale beams were used as control beams whereas the remaining fifteen half-scale beams were reinforced with GFRP bars using three different reinforcement ratios. The beams were tested to failure to examine their behaviour and determine the effect of varying the GFRP reinforcement ratio. In order to extend the applicability of the experimental results to typical timber bridge stringers, three full-scale stringers, taken from a 40 year-old timber bridge, were also reinforced with GFRP bars. A fourth full-scale stringer was used as an unreinforced control beam. All of the beams were tested to failure to determine the efficiency of the strengthening technique. Prior to the half-scale and full-scale beam tests, six small

timber beams reinforced with GFRP bars were used to obtain a qualitative assessment of the bond performance between the creosote-treated timber, epoxy resin, and GFRP bars.

Based on the analysis of the test results, a bending strength model is proposed and calibrated using the results of the half-scale unreinforced timber beam tests. The bending strength model is modified to account for the effect of the GFRP reinforcement and the modified model is calibrated using the results of the half-scale reinforced timber beam tests. The proposed bending strength model is used to examine the effect of varying the GFRP reinforcement ratio.

6.2 CONCLUSIONS

This study has shown that GFRP bars are an effective technique for strengthening the flexural capacity of sawn timber bridge beams. The following summarizes the findings of this investigation:

1. There is adequate bond between the creosote-treated timber and epoxy resin. It should be mentioned that the results are representative of short-term behaviour and did not include long-term behaviour.

2. All of the plain timber beams failed in a brittle tension flexural failure mode. The flexural failure mode changed to a more ductile compression-initiated failure mode for 60 percent of the reinforced beams.

3. The GFRP bars did not rupture in any of the tested specimens. Minor localized debonding was observed adjacent to cracks in the timber, but the bond between the timber, epoxy, and GFRP bars remained fully intact outside the failure regions of the beam.

4. The ultimate tensile strain of the timber, ε_{tu}, increased 64 percent for the reinforced beams. The FRP material arrests crack opening, confines local rupture, and bridges local defects in the adjacent timber, allowing the timber to support higher nominal stresses and strains before failing.

5. Similar behaviour in terms of failure mode, load-deflection, strain distribution, and ultimate strength was observed for the half-scale and full-scale timber and reinforced timber beams. There was no evidence of a size effect between the half-scale and full-scale beams.

6. The proposed analytical model is based on assuming a bilinear stress-strain relationship for the timber in compression and calculating the tensile failure stress in bending, f_m, using brittle fracture theory. Increasing the failure stress f_m by the factor α_m = 1.30 for the reinforced beams was found to give good calibration with the experimental results for sawn Douglas Fir timber beams.

7. The proposed analytical model predicts a strength increase of 18 to 46 percent depending on the reinforcement ratio and strength of the original timber for

reinforcement ratios ranging from 0.27 to 0.82 percent and timber strength ranging from 20 to 70 MPa.

8. The strength enhancement was not proportional to the amount of reinforcement. Increasing the reinforcement ratio from 0.27 to 0.82 percent increased the strength enhancement only by approximately 30 percent while the amount of reinforcement was increased three times in magnitude. The effective increase in timber strength accounts for a larger portion of the strength enhancement than the GFRP reinforcement.

9. For timber with a strength of 20 MPa, which corresponds to the design strength, the proposed model predicts a strength increase of 35 to 45 percent for reinforcement ratios ranging from 0.27 to 0.82 percent. This level of enhancement exceeds the minimum 25 percent increase in strength outlined in the research objectives.

6.3 RECOMMENDATIONS FOR FUTURE RESEARCH

In order to achieve full understanding of the structural behaviour of FRP-reinforced timber, further research work is recommended in the following areas:

1. Investigate the long-term bond performance between the epoxy resin and timber over a wide range of environmental conditions.

2. Evaluate the behaviour of FRP-reinforced timber under cyclic and dynamic loading.

3. Investigate and quantify the increase in effective tensile strength of timber caused by the presence of FRP materials.

4. Develop techniques for shear strengthening of timber bridge stringers.

REFERENCES

1. AASHTO (1996). *Standard Specifications for Highway Bridges*, American Association of State Highway and Transportation Officials, Washington DC.

2. ASTM (1992). Standard methods for static tests of timber in structural sizes, ASTM D198-92. American Society for Testing and Materials, Philadelphia, PA.

3. Bakoss, S.L., Greenland, A. and Crews, K.I. (1999). "Bridge deck and industrial heavy-duty flooring system based on laminated veneer lumber beams reinforced with carbon fibre composites." Proceedings of the 8th International Conference on Structural Faults and Repair, London, UK, July 13-15, 1999.

4. Barrett, J.D., and Lau, W. (1994). Canadian Lumber Properties. Edited by E.D. Jones, Canadian Wood Council, Ottawa, Ontario, Canada.

5. Bazan, I.M.M., (1980). "Ultimate bending strength of timber beams." Ph.D. thesis presented to Nova Scotia Technical College, Halifax, Nova Scotia, Canada.

6. Bohannan, B. (1962). "Prestressed wood members." *Forest Products Journal*, 12(12), pp. 596-602.

7. Bohannan, B. (1966). "Effect of member size on bending strength of wood members." *Forest Service Research Paper FPL 56*, U.S. Department of Agriculture, Washington, D.C.

8. Buchanan, A.H. (1984). "Strength model and design methods for bending and axial load interaction in timber members." Ph.D. thesis presented to the University of British Columbia, Vancouver, British Columbia, Canada.

9. Buchanan, A.H. (1990). "Bending strength of lumber." *Journal of Structural Engineering*, ASCE, 116(5), pp. 1213-1229.

10. Bulleit, W.M., Sandberg, L.B., and Woods, G.J. (1989). "Steel-reinforced glued laminated timber." *Journal of Structural Engineering.*, ASCE, 115(2), pp. 433-444.

11. Chajes, M.J., Kaliakin, V.N. and Meyer, A.J. (1996). "Behaviour of engineered wood-CFRP beams." Proceedings of the Fifth International Conference on Composites in Infrastructure, ICCI 96, Tucson, Arizona, pp. 870-877.

12. Dagher, H.D. and Lindeyberg, R. (2000). "Development of AASHTO design specifications of FRP-glulam bridges." Transportation Research Board 79th Annual Meeting, January 9-13, 2000, Washington DC.

13. Dorey, A.B. and Cheng, J.J.R. (1996). "The behaviour of GFRP glued laminated timber beams." Proceedings in Advanced Composite Materials in Bridges and Structures, ACMBS II, M.M. El-Badry, Editor. Montreal, Quebec, Canada, pp. 787-794.

14. Galloway, T.L., Fogstad, C., Dolan, C.W. and Puckett, A.J. (1996). "Initial tests of Kevlar prestressed timber beams." *Gen. Tech. Rep. FPL-GTR-94.* Madison, Wisconsin: U.S. Department of Agriculture, Forest Service, Forest Products Laboratory.

15. Hernandez, R., Davalos, J.F., Sonti, S.S., Kim, Y. and Moody, R.C. (1997). "Strength and stiffness of reinforced yellow-poplar glued laminated beams." *Res. Pap. FPL-RP-554.* Madison, Wisconsin: U.S. Department. of Agriculture, Forest Service, Forest Products Laboratory.

16. Johns, K.C. and Lacroix, S. (2000). "Composite reinforcement of timber in bending." Accepted for publication in the *Canadian Journal of Civil Engineering*.

17. Lantos, G. (1970). "The flexural behaviour of steel reinforced laminated timber beams." *Wood Science.*, 2(3), pp. 136-143.

18. Madsen, B. and Buchanan, A.H. (1986). "Size effects in timber explained by a modified weakest link theory." *Canadian Journal of Civil Engineering*, 13(2), pp. 218-232.

19. Madsen, B. (1992). Structural Behaviour of Timber, Timber Engineering Ltd., North Vancouver, British Columbia, Canada.

20. Mark, R. (1961). "Wood-aluminum beams within and beyond the elastic range." *Forest Products Journal*, 11(10), pp. 477-484.

21. Neale, K.W. and Labossière, P. (1997). "State-of-the-art report on retrofitting and strengthening by continuous fibre in Canada." Third International Symposium on Non-Metallic Reinforcement for Concrete Structures, Japan Concrete Institute, October 14-16, 1997, Sapporo, Japan, pp. 25-39.

22. Peterson, J. (1965). "Wood beams prestressed with bonded tension elements." *Journal of Structural Engineering.*, ASCE, 91(1), pp. 103-119.

23. Plevris, N. and Triantafillou, T.C. (1992). "FRP-reinforced wood as a structural material." *Journal of Materials in Civil Engineering*, ASCE, 4(3), pp. 300-317.

24. Rizkalla, S.H. (1997). "A new generation of civil engineering structures." Third International Symposium on Non-Metallic Reinforcement for Concrete Structures, Japan Concrete Institute, October 14-16, 1997, Sapporo, Japan, pp. 113-128.

25. Sliker, A. (1962). "Reinforced wood laminated beams." *Forest Products Journal*, 12(1), pp. 91-96

26. Sonti, S.S., GangaRao, H.V.S. and Superfesky, M.C. (1996). "Rehabilitation and strengthening of glulam stringers for bridge superstructures." Proceedings of the Fifth International Conference on Composites in Infrastructure, ICCI 96, Tucson, Arizona, pp. 800-813.

27. Swanson, S.R. (1997) Introduction to design and analysis with advanced composite materials, Prentice Hall, Upper Saddle River, NJ.

28. Tingley, D.A. and Gai, C. (1998). "FRP reinforced glulam performance: A case study of the Lighthouse bridge." Proceedings in Developments in Short and Medium Span Bridge Engineering, Canadian Society for Civil Engineering, 1998.

29. Triantafillou, T.C. and Deskovic, N. (1992). "Prestressed FRP sheets as external reinforcement of wood members." *Journal of Structural Engineering*, ASCE, 118(5), pp. 1270-1284.

30. Triantafillou, T.C. (1998). "Strengthening of structures with advanced FRPs." *Progress in Structural Engineering and Materials*, 1(2), pp. 126-134.

31. Weibull, W. (1939). "A statistical theory of the strength of materials." *Proc. No. 151*, Royal Swedish Institute of Engineering Research, Stockholm, Sweden.

APPENDIX A

LOAD-DEFLECTION AND LOAD-STRAIN CURVES

Figures A1 to A23 contain two figures each showing the results for each beam test. Figures (a) are load-deflection curves, which illustrate the beam deflection at mid-span up to failure. Figures (b) are load-strain curves at four or five locations across the beam cross-section. The locations of the pi-gauges used to measure the strain are shown below.

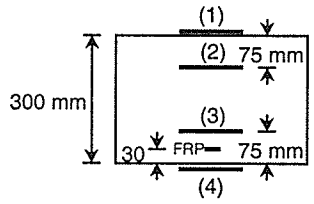

Half-scale beams

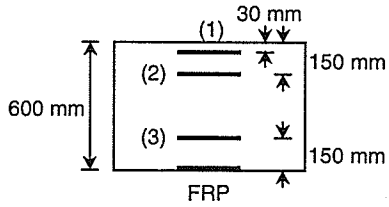

Full-scale beams

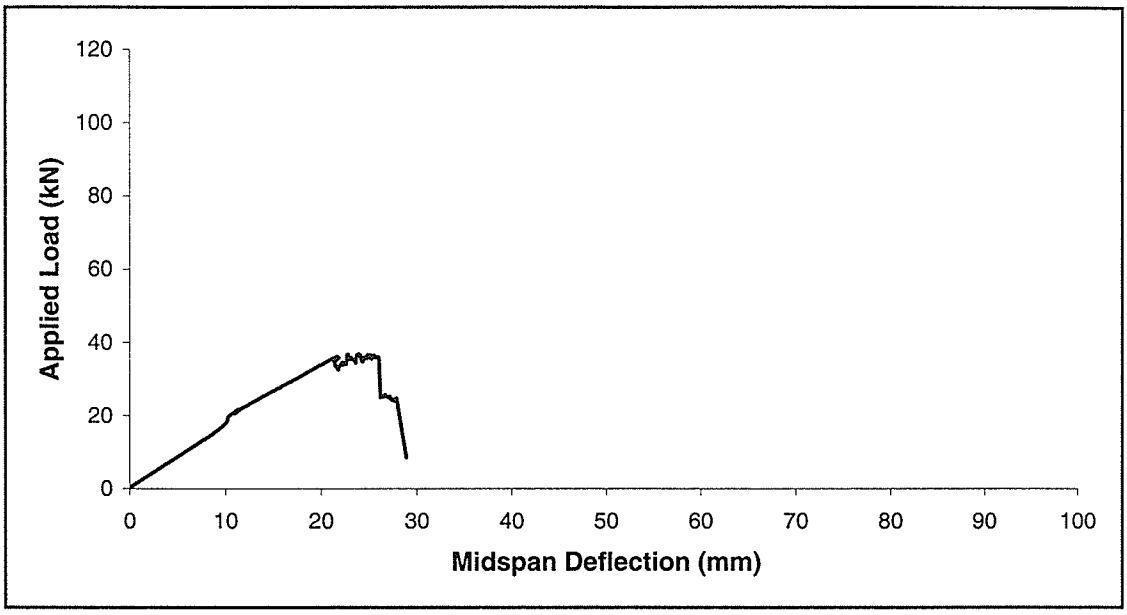

Figure A1(a) – Load-deflection curve for Beam A1 (plain timber)

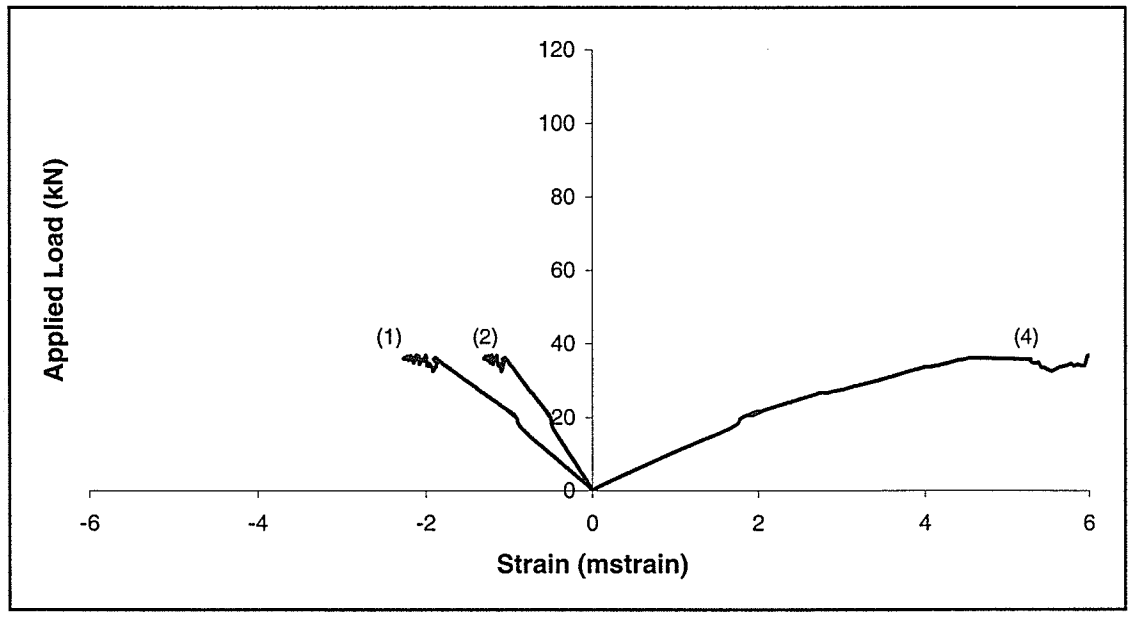

Figure A1(b) – Load-strain curves for Beam A1 (plain timber)

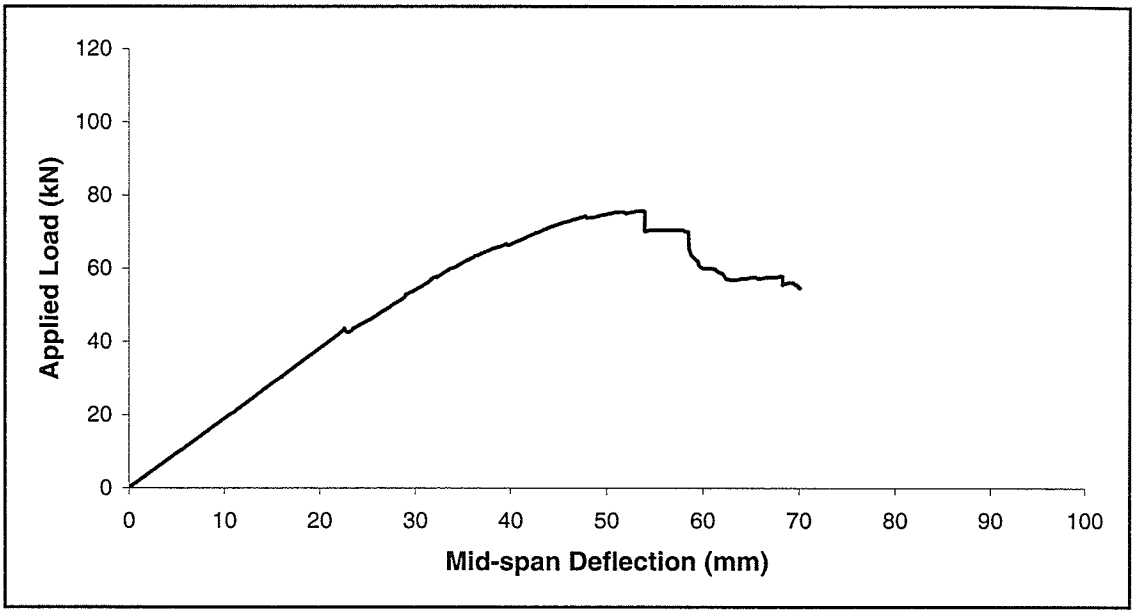

Figure A2(a) – Load-deflection curve for Beam A2 (ρ_{GF} = 0.82%)

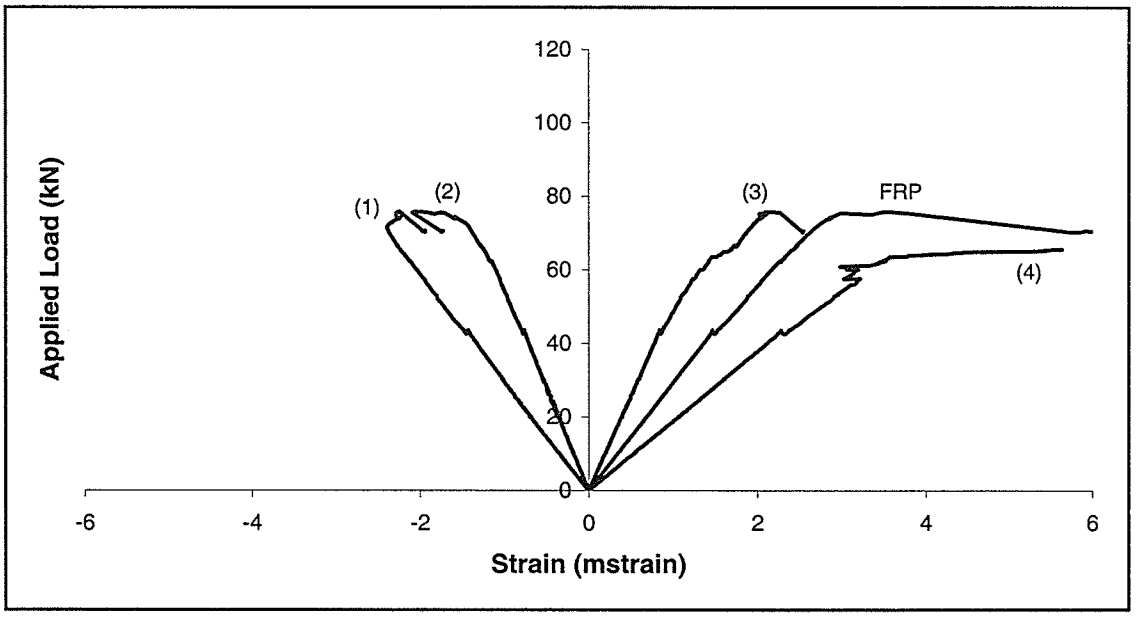

Figure A2(b) – Load-strain curves for Beam A2 (ρ_{GF} = 0.82%)

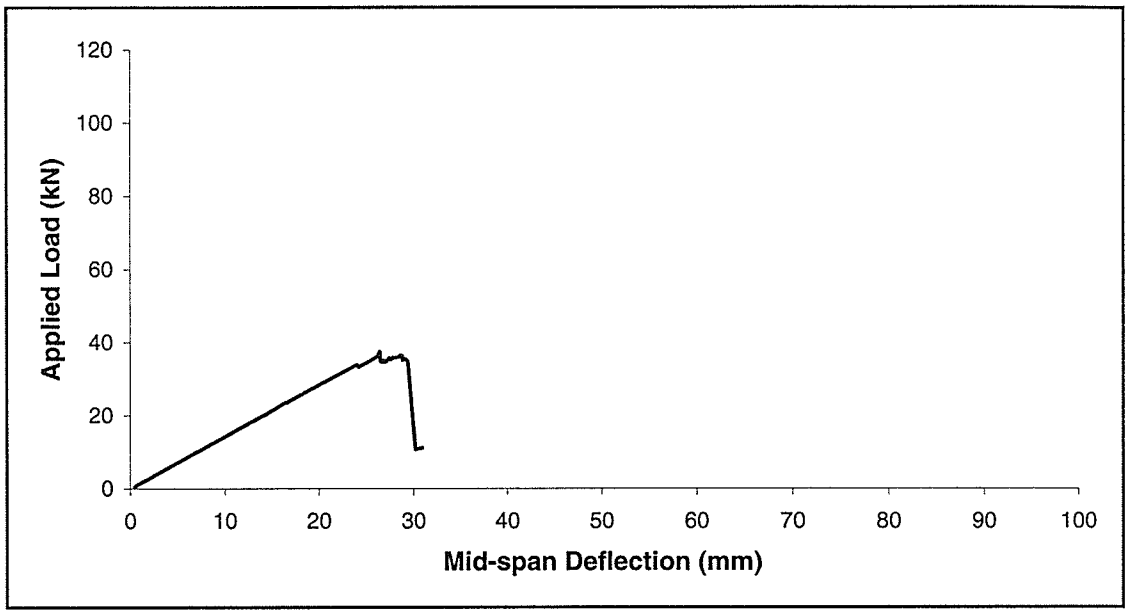

Figure A3(a) – Load-deflection curve for Beam B1 (plain timber)

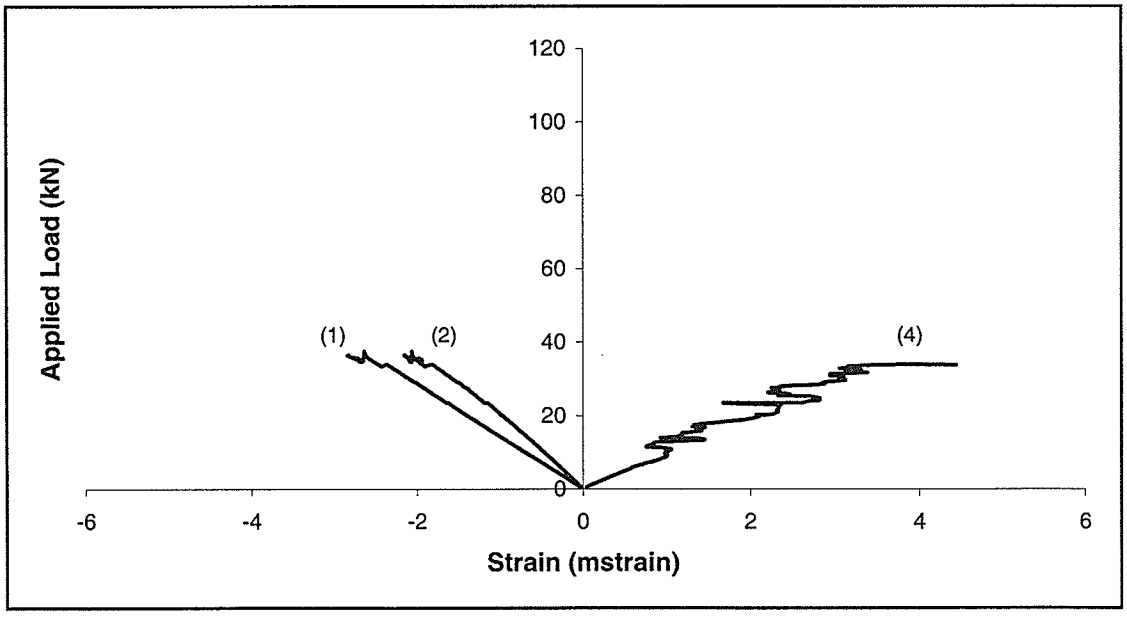

Figure A3(b) – Load-strain curves for Beam B1 (plain timber)

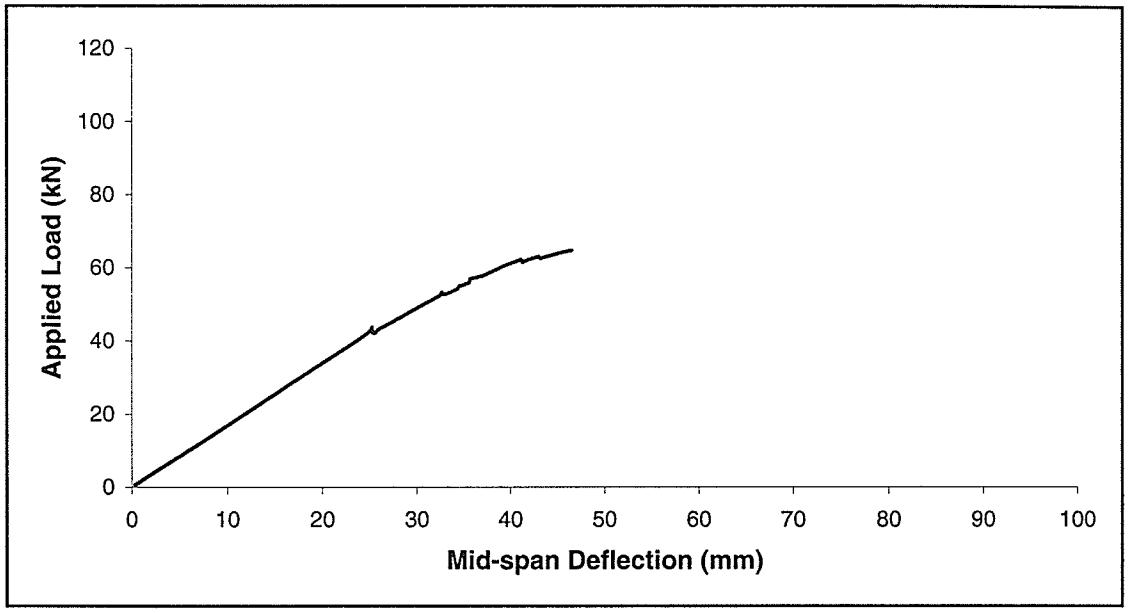

Figure A4(a) – Load-deflection curve for Beam C1 (plain timber)

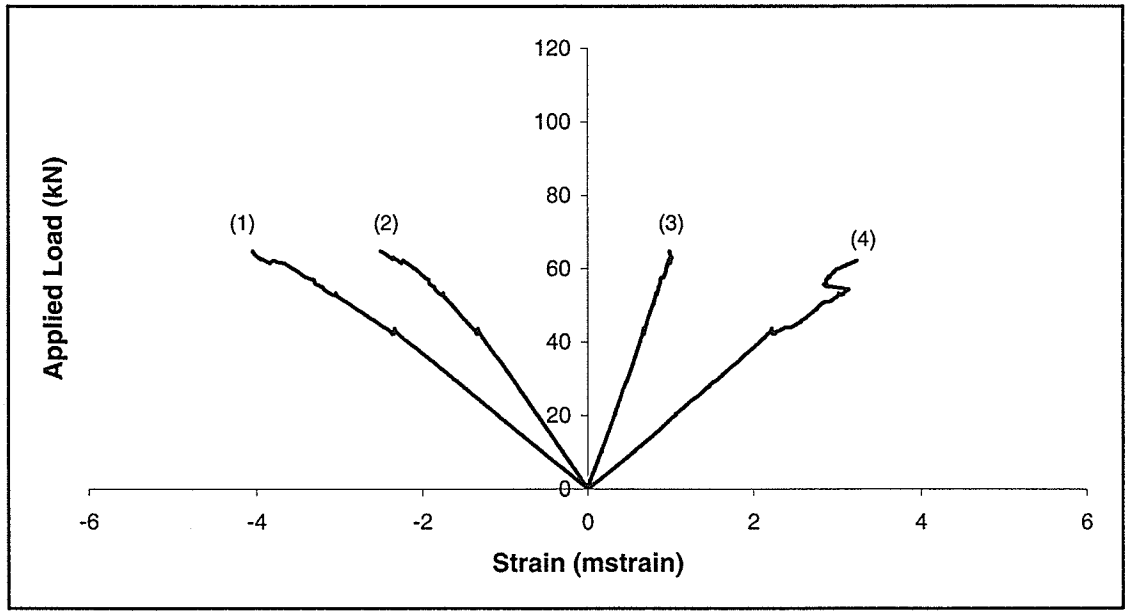

Figure A4(b) – Load-strain curves for Beam C1 (plain timber)

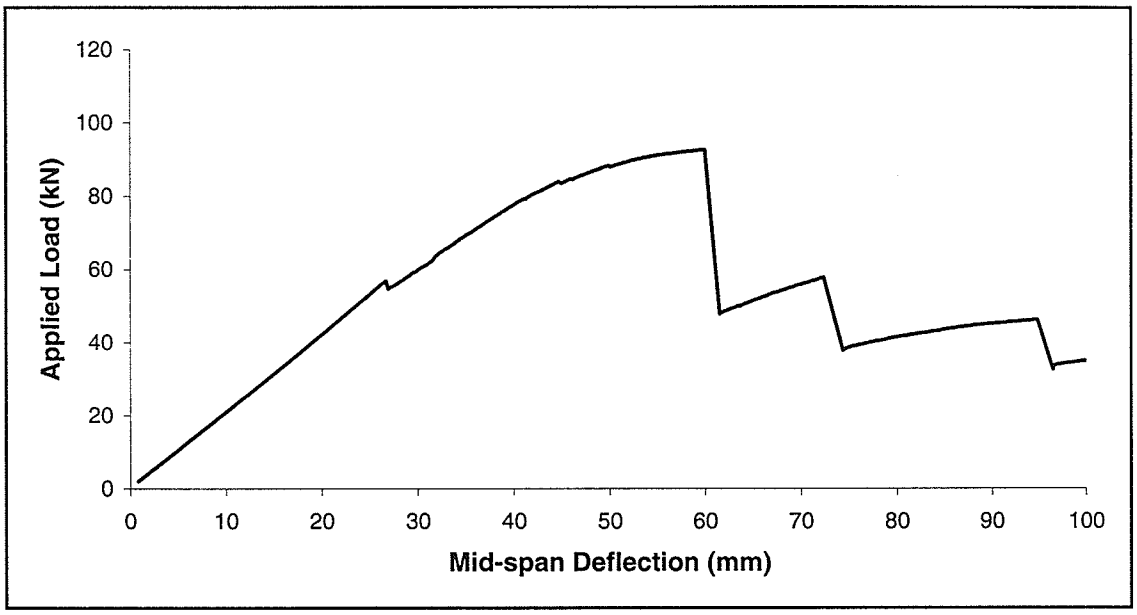

Figure A5(a) – Load-deflection curve for Beam D1 (ρ_{GF} = 0.27%)

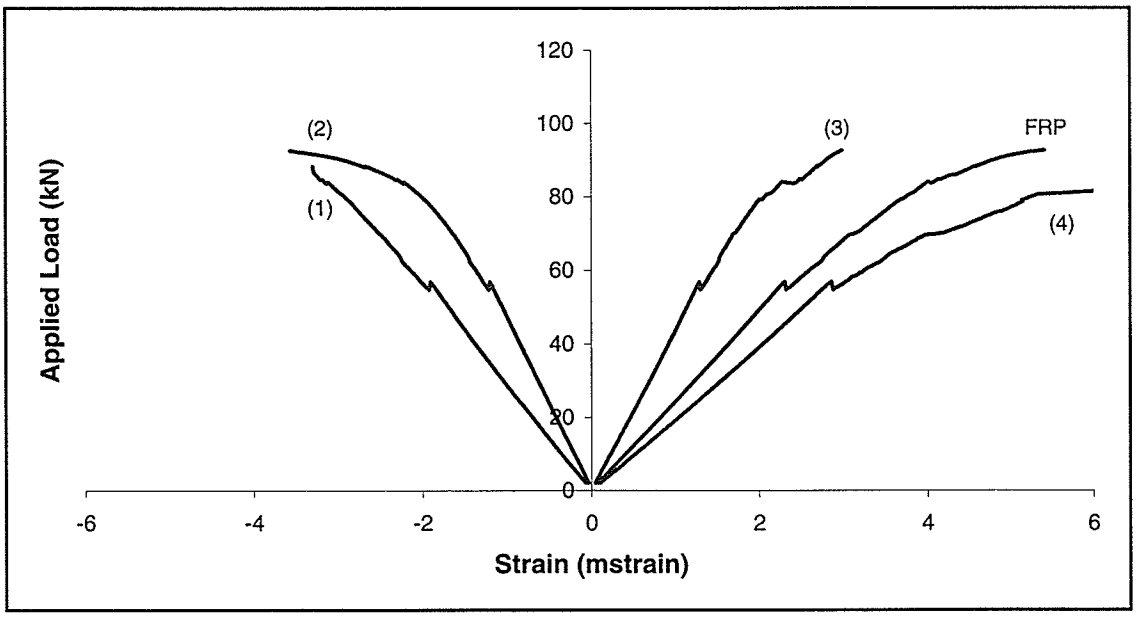

Figure A5(b) – Load-strain curves for Beam D1 (ρ_{GF} = 0.27%)

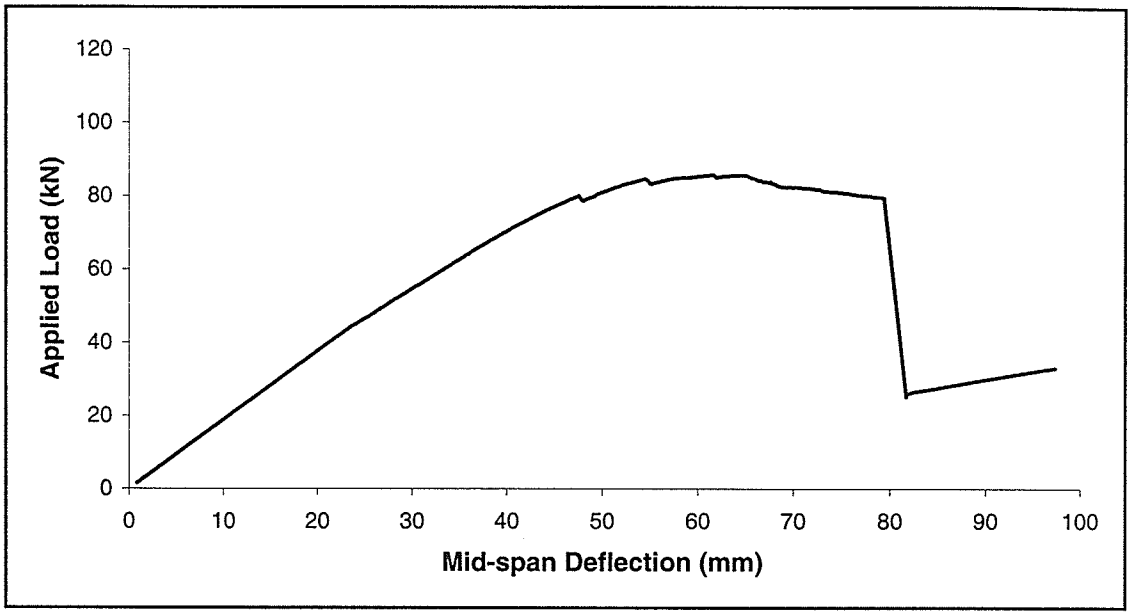

Figure A6(a) – Load-deflection curve for Beam D2 (ρ_{GF} = 0.27%)

Strains not measured for Beam D2.

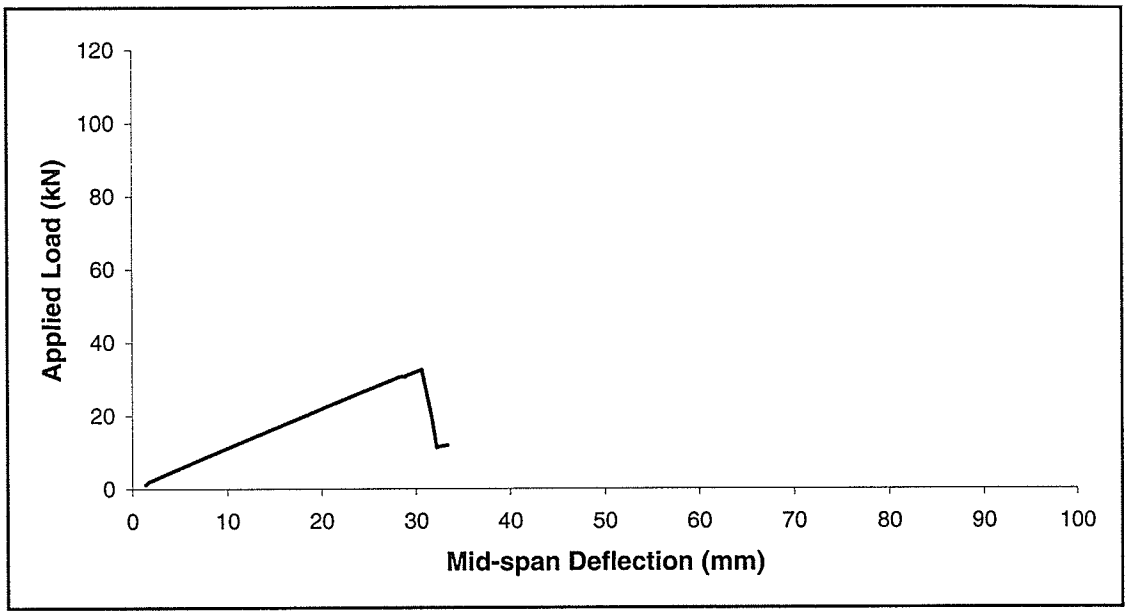

Figure A7(a) – Load-deflection curve for Beam F1 (plain timber)

Strains not measured for Beam F1.

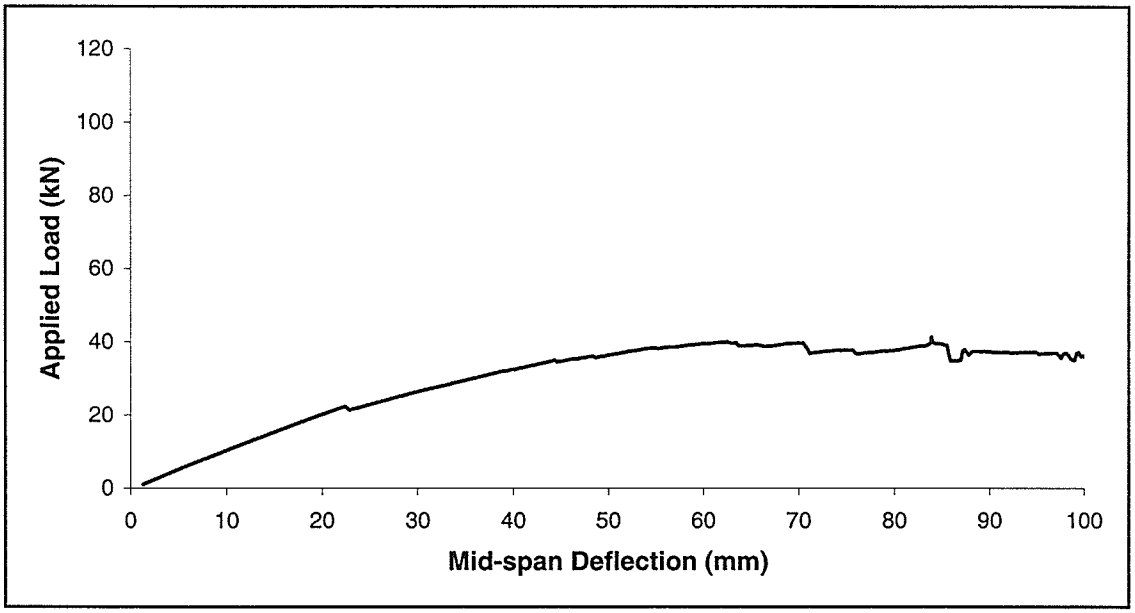

Figure A8(a) – Load-deflection curve for Beam F2 (ρ_{GF} = 0.27%)

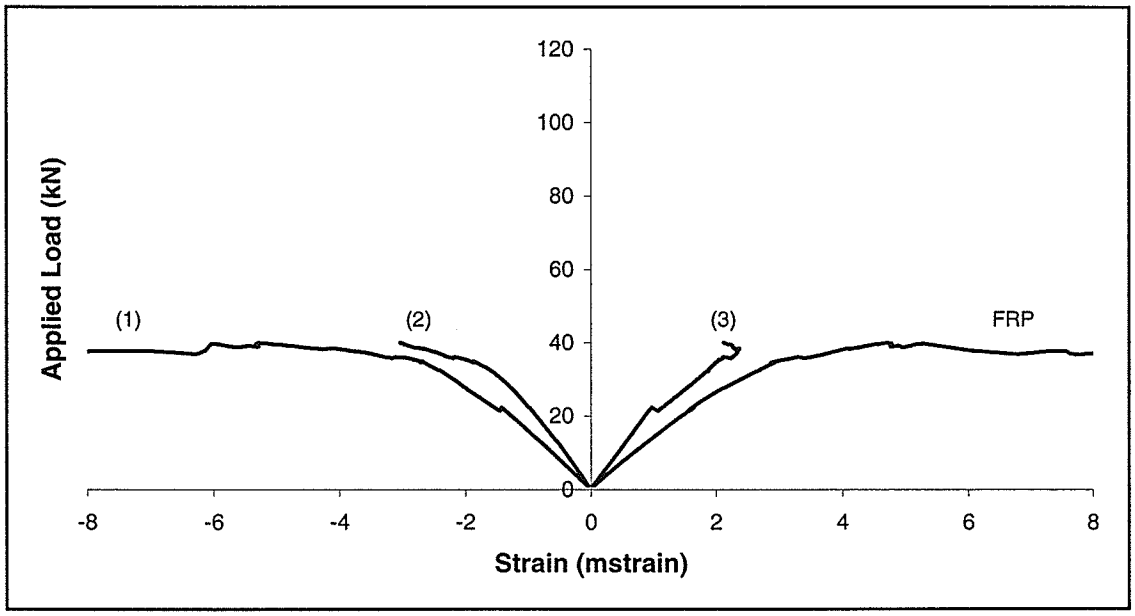

Figure A8(b) – Load-strain curves for Beam F2 (ρ_{GF} = 0.27%)

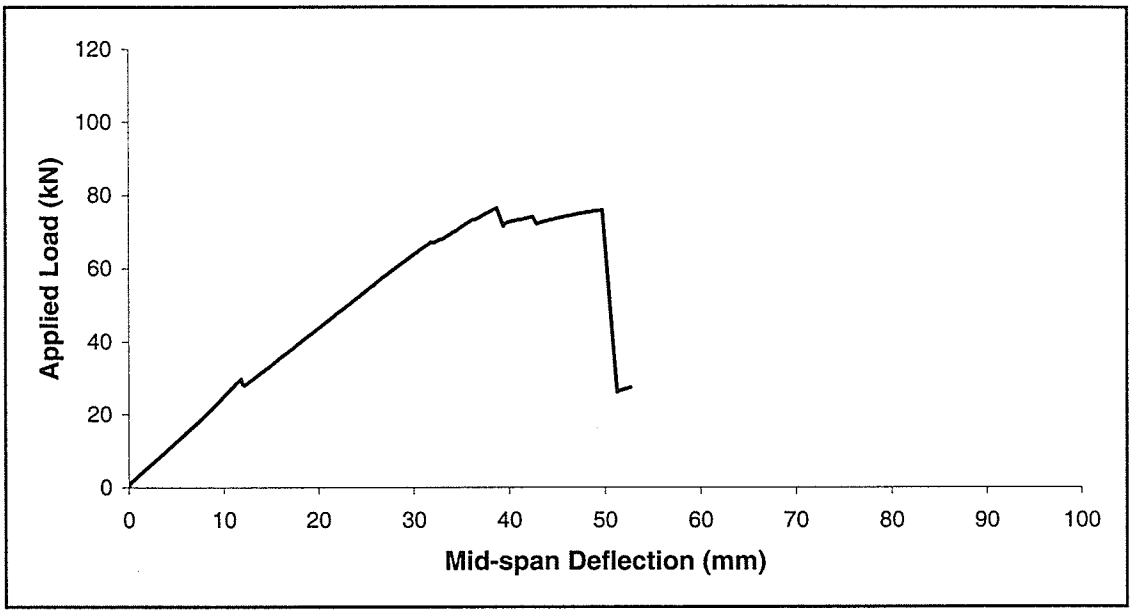

Figure A9(a) – Load-deflection curve for Beam G1 (plain timber)

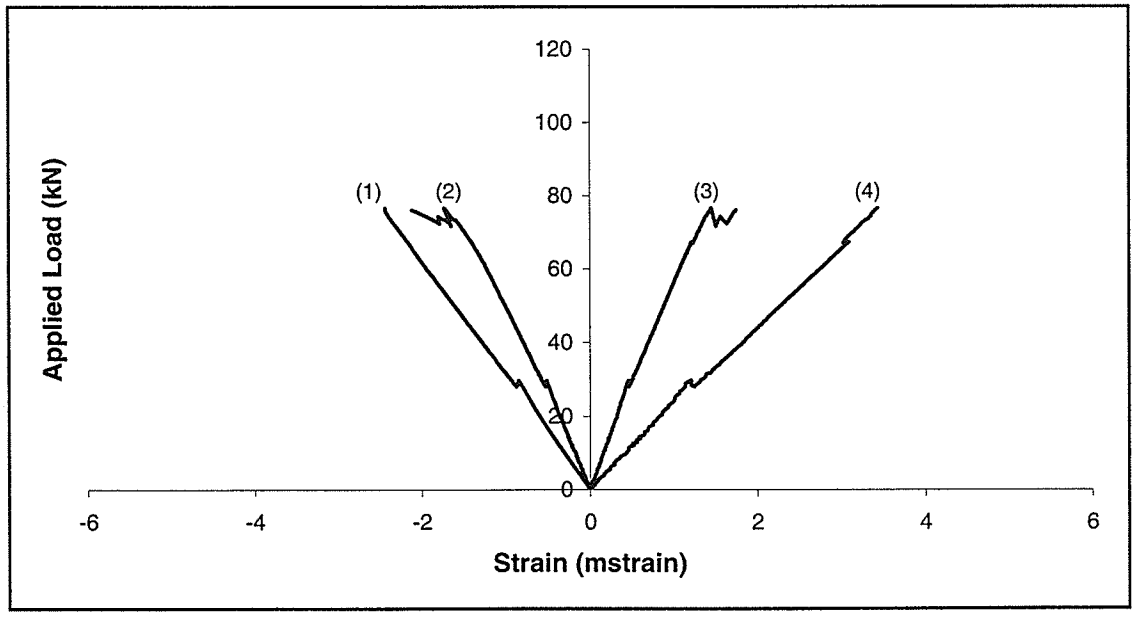

Figure A9(b) – Load-strain curves for Beam G1 (plain timber)

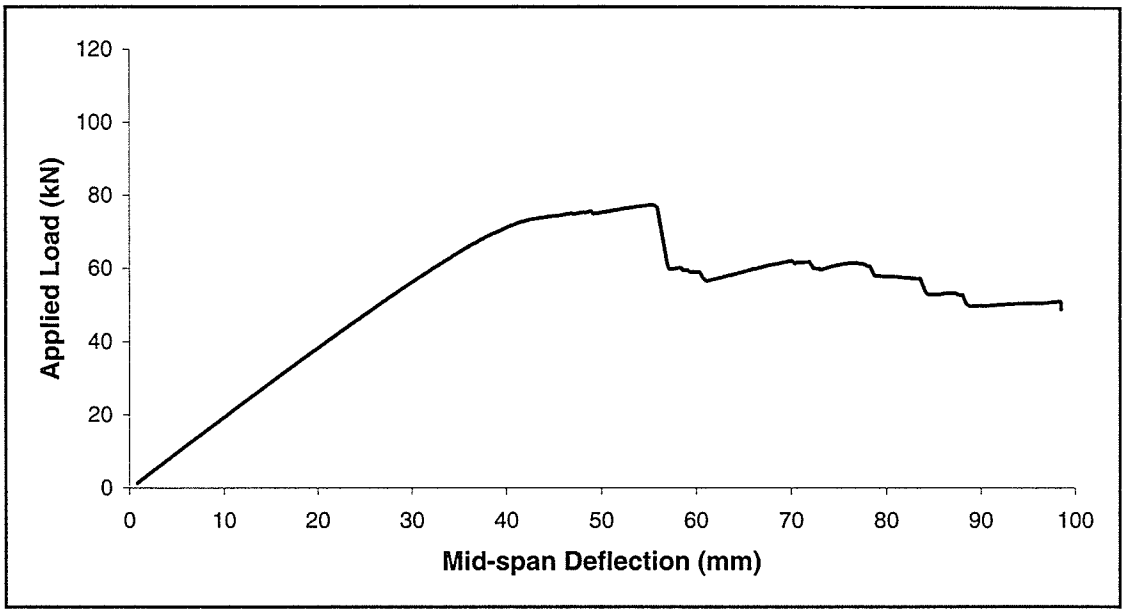

Figure A10(a) – Load-deflection curve for Beam G2 (ρ_{GF} = 0.82%)

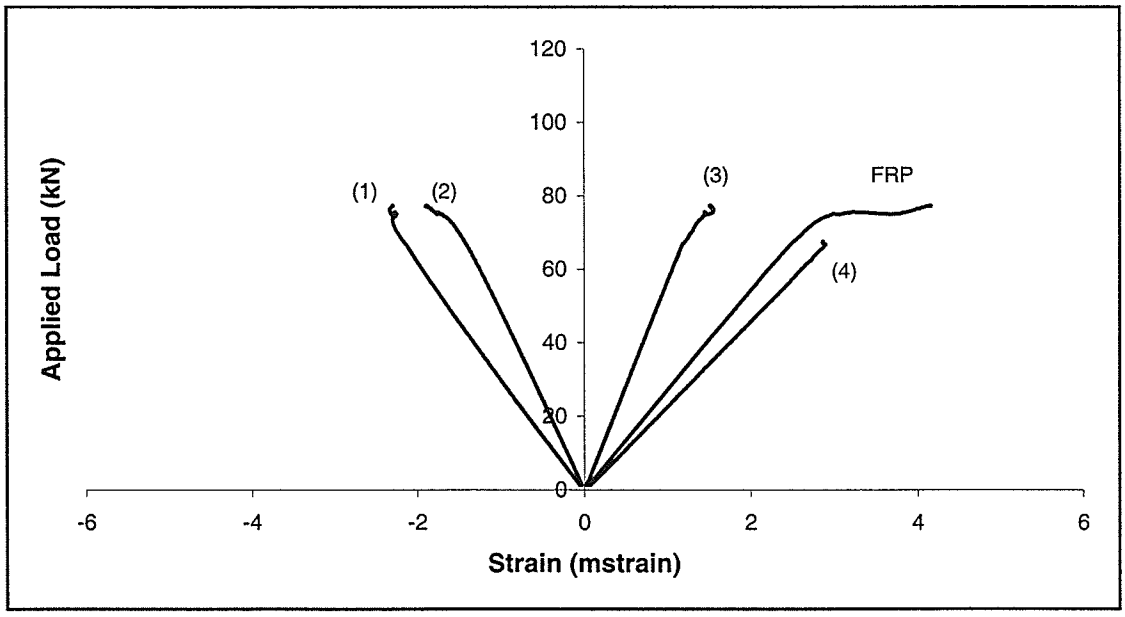

Figure A10(b) – Load-strain curves for Beam G2 (ρ_{GF} = 0.82%)

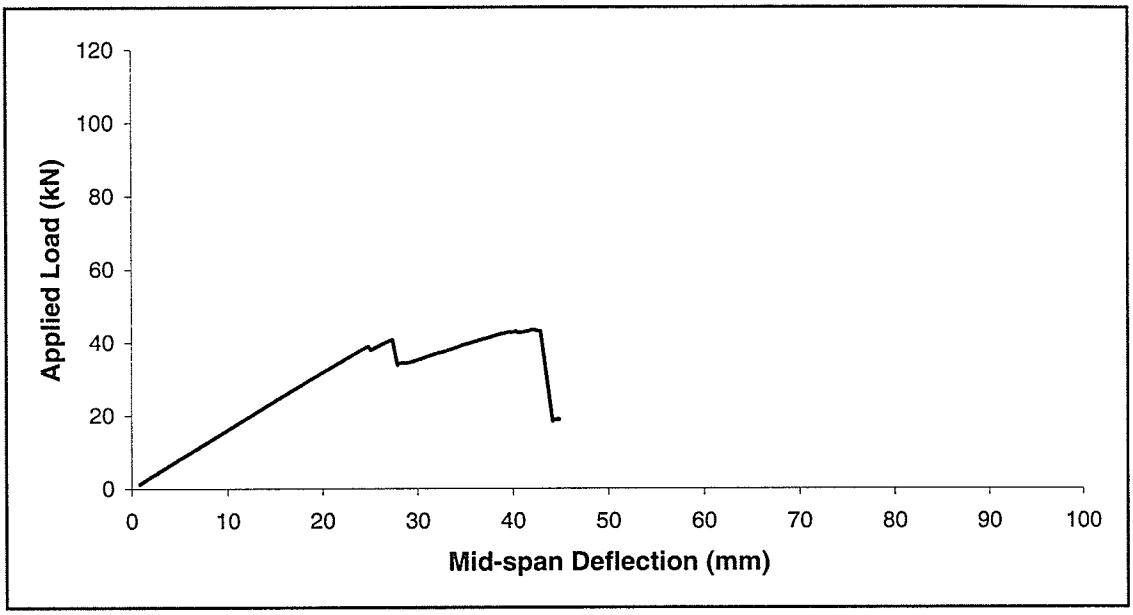

Figure A11(a) – Load-deflection curve for Beam H1 (plain timber)

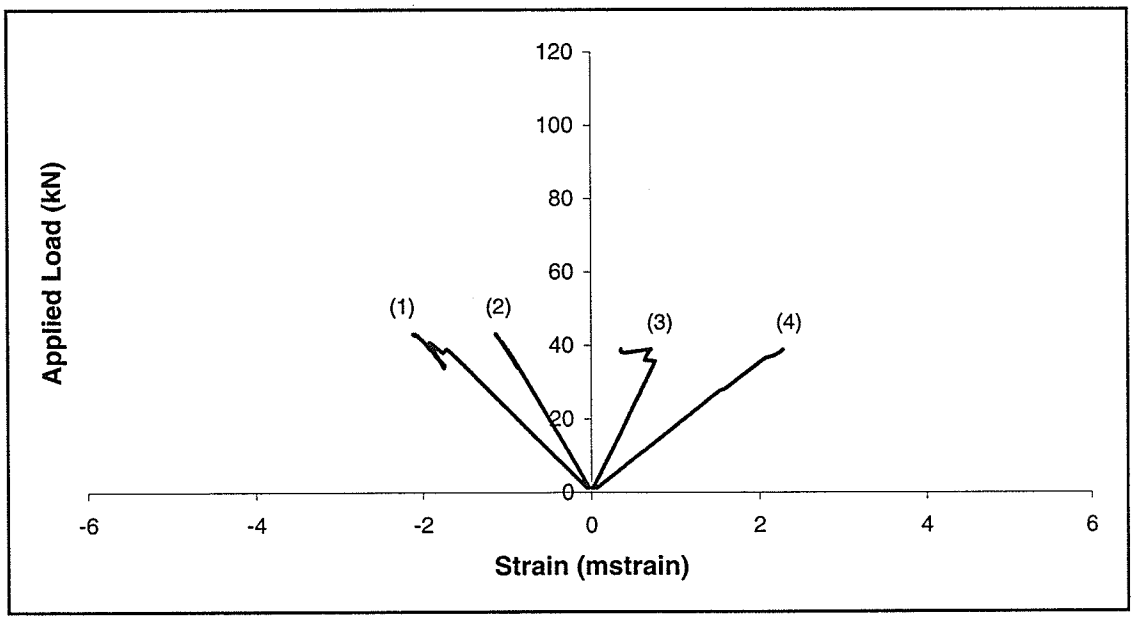

Figure A11(b) – Load-strain curves for Beam H1 (plain timber)

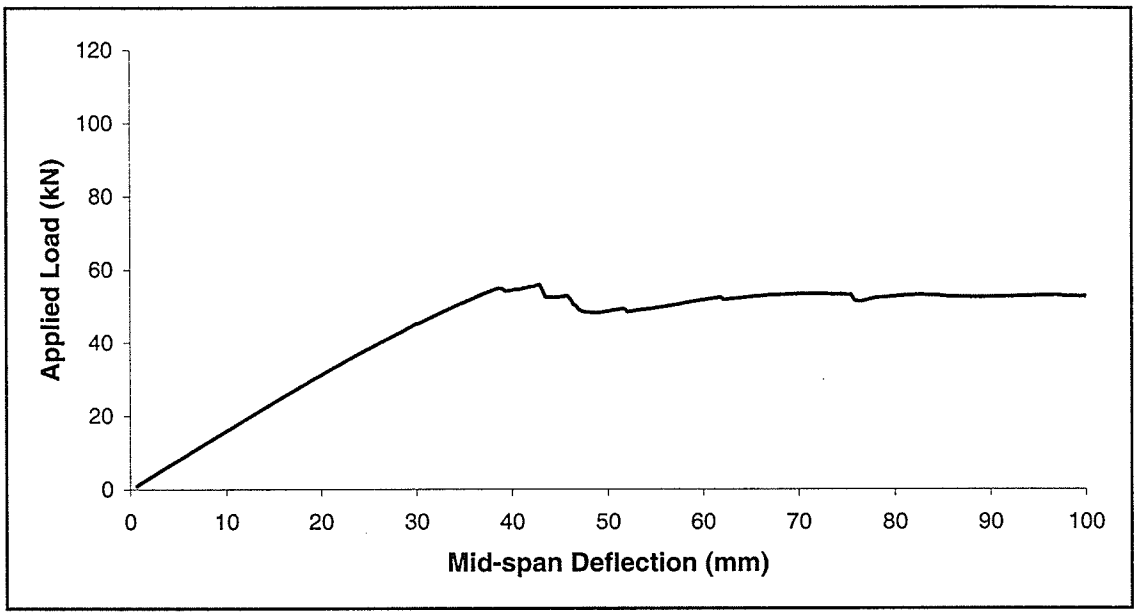

Figure A12(a) – Load-deflection curve for Beam H2 (ρ_{GF} = 0.41%)

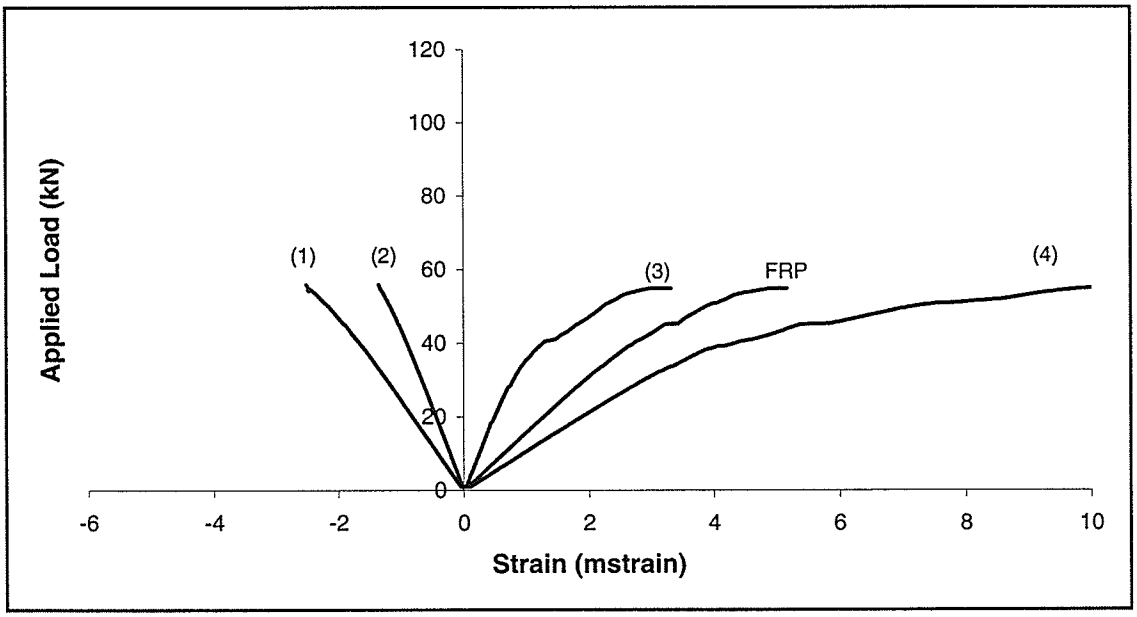

Figure A12(b) – Load-strain curves for Beam H2 (ρ_{GF} = 0.41%)

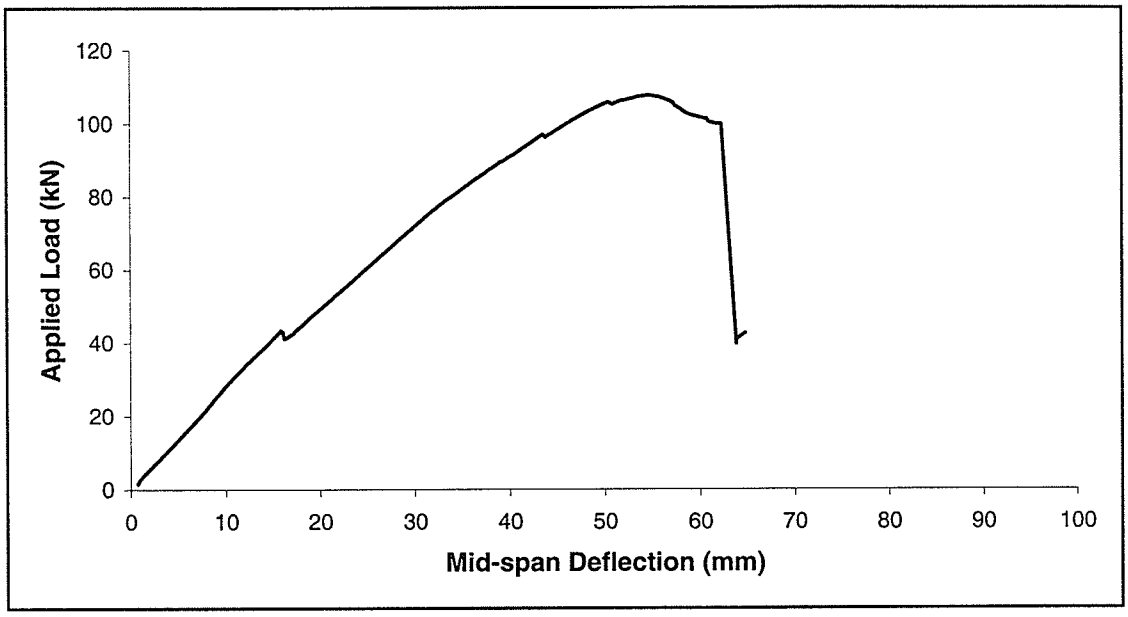

Figure A13(a) – Load-deflection curve for Beam I1 (ρ_{GF} = 0.41%)

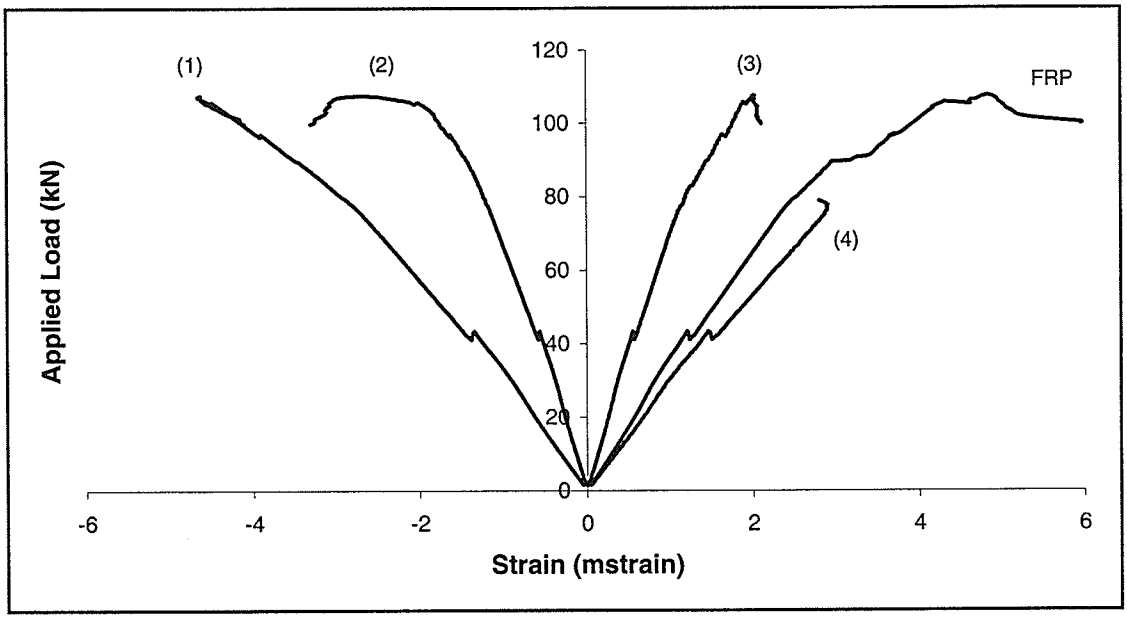

Figure A13(b) – Load-strain curves for Beam I1 (ρ_{GF} = 0.41%)

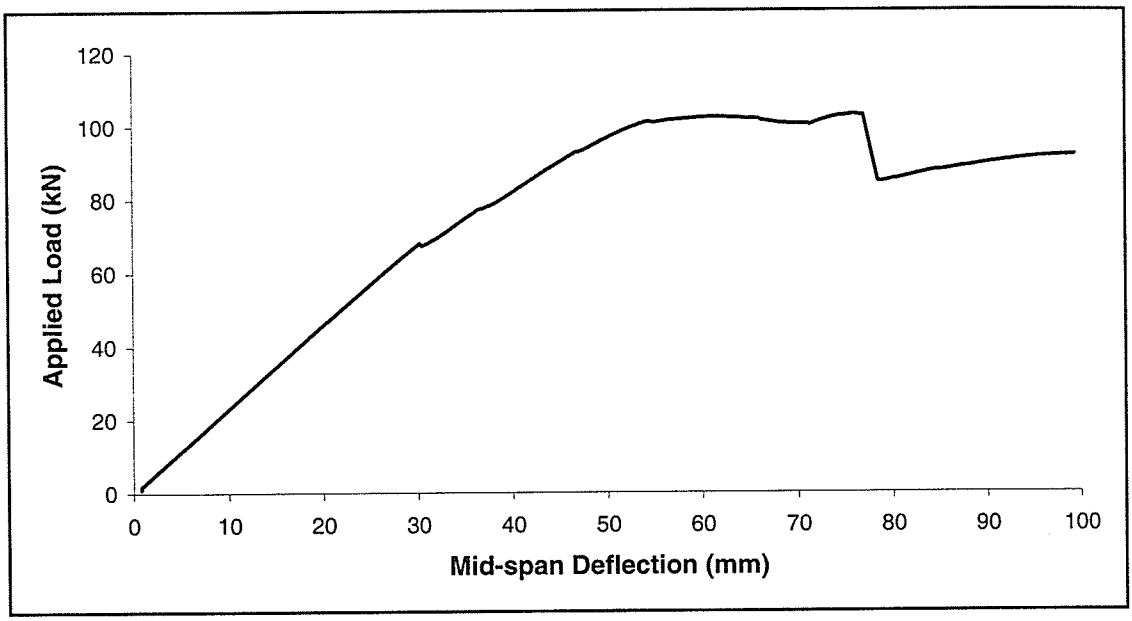

Figure A14(a) – Load-deflection curve for Beam I2 (ρ_{GF} = 0.82%)

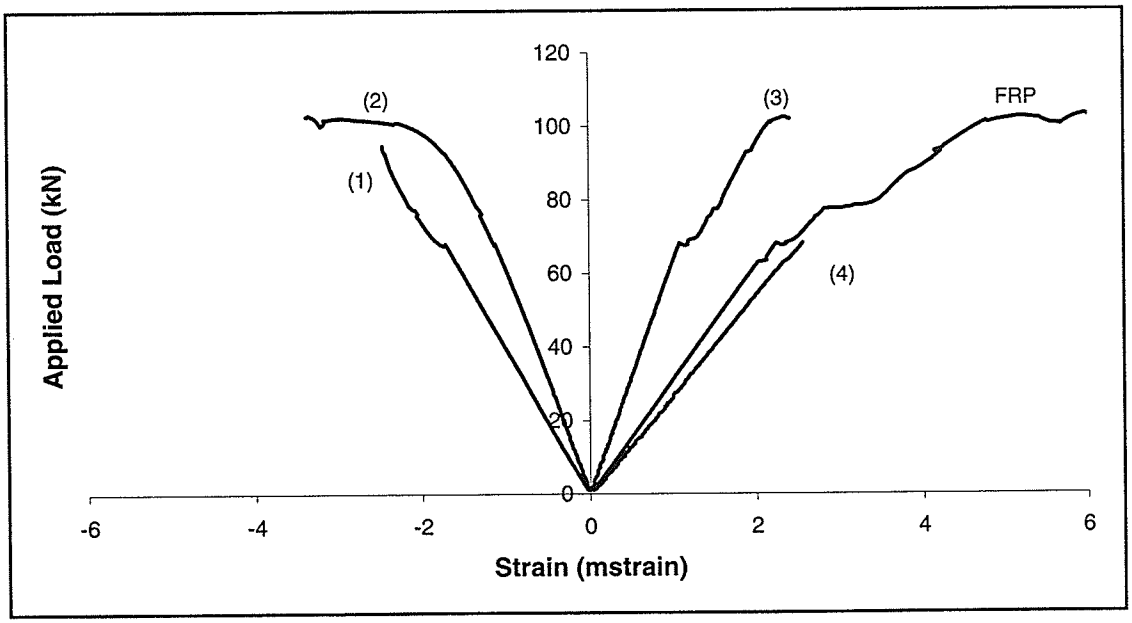

Figure A14(b) – Load-strain curves for Beam I2 (ρ_{GF} = 0.82%)

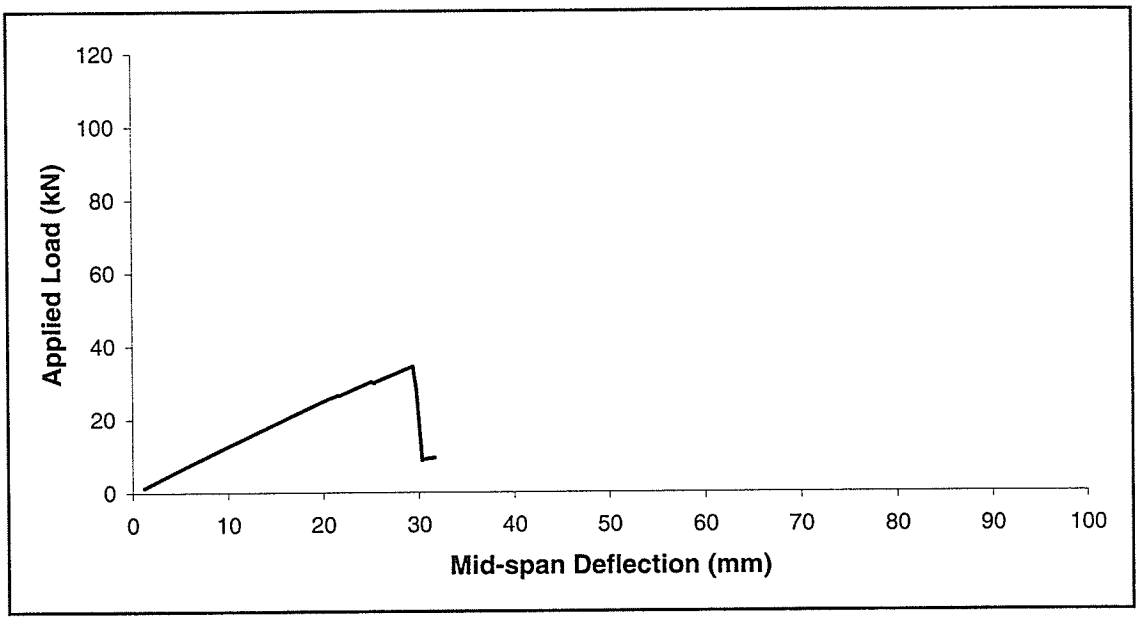

Figure A15(a) – Load-deflection curve for Beam J1 (plain timber)

Strains not measured for Beam J1.

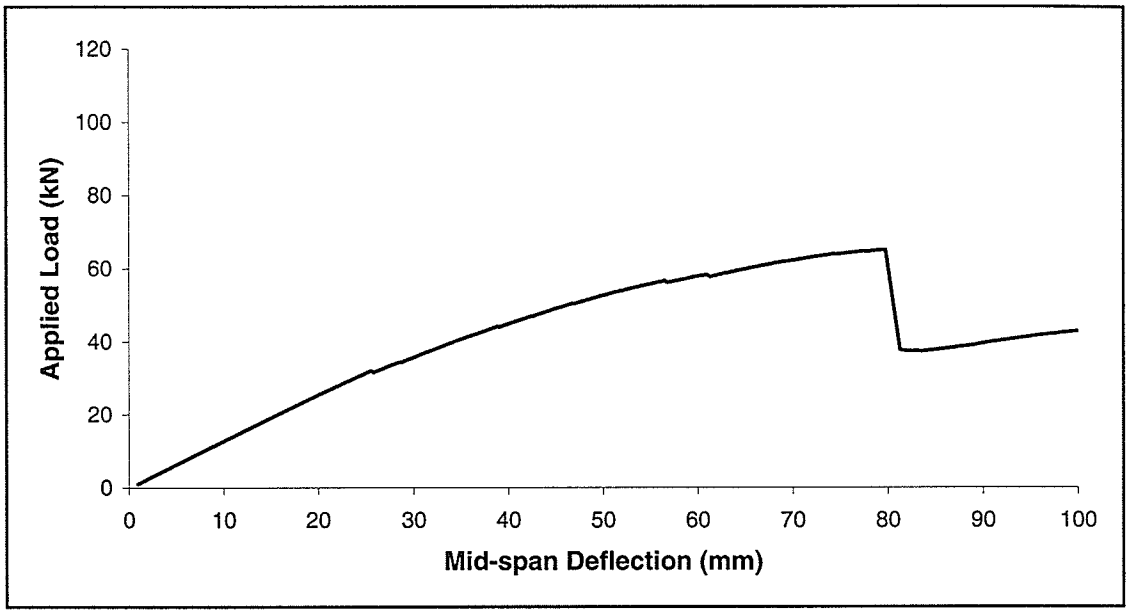

Figure A16(a) – Load-deflection curve for Beam K1 (ρ_{GF} = 0.41%)

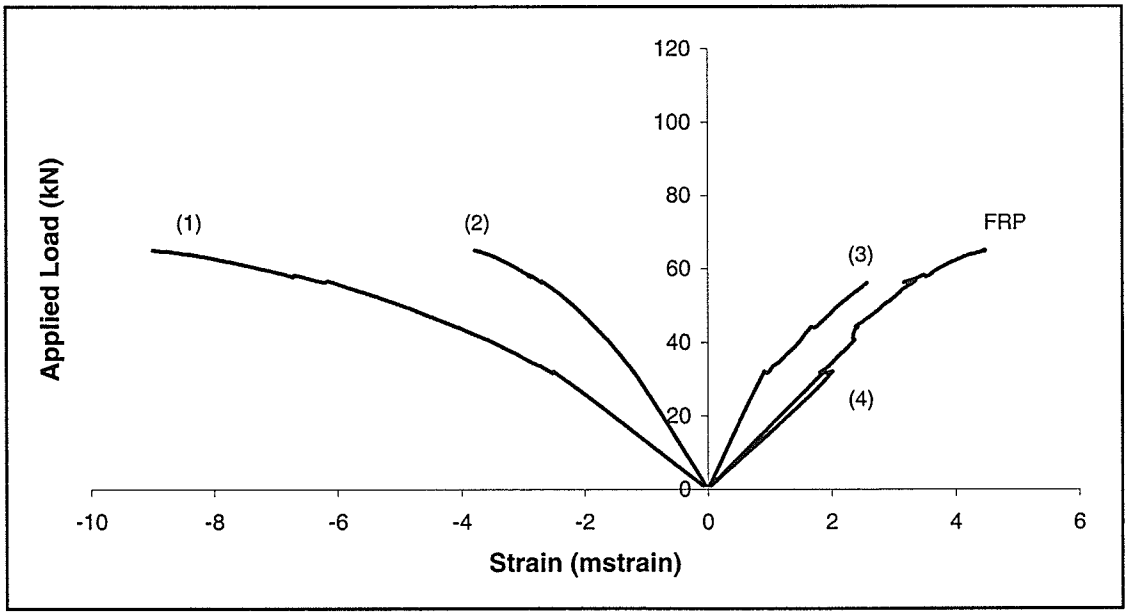

Figure A16(b) – Load-strain curves for Beam K1 (ρ_{GF} = 0.41%)

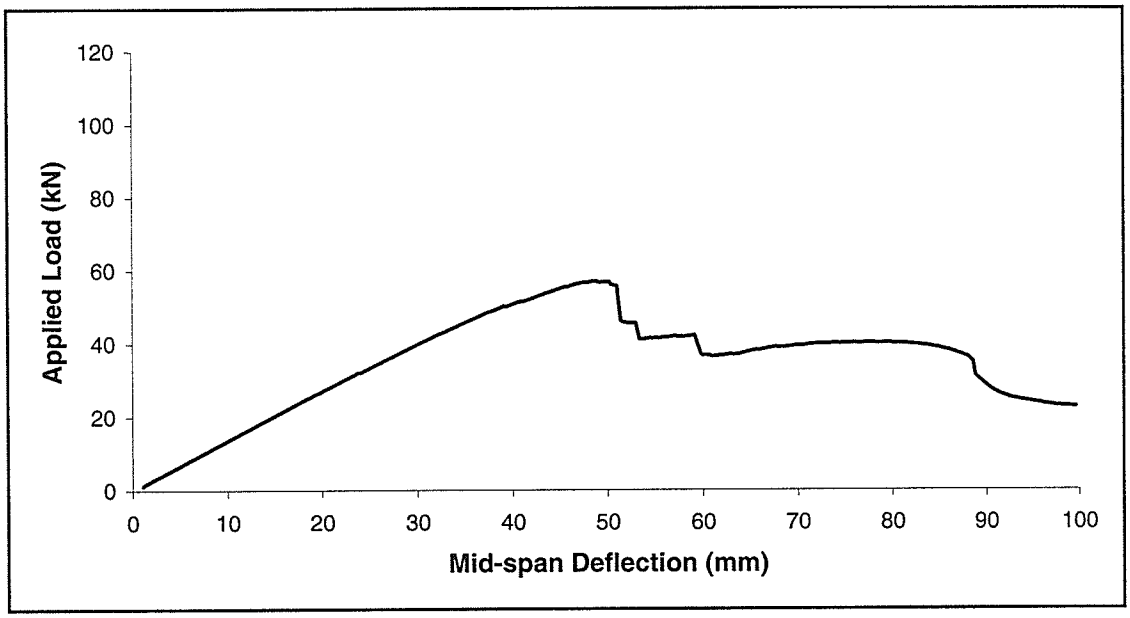

Figure A17(a) – Load-deflection curve for Beam K2 (ρ_{GF} = 0.82%)

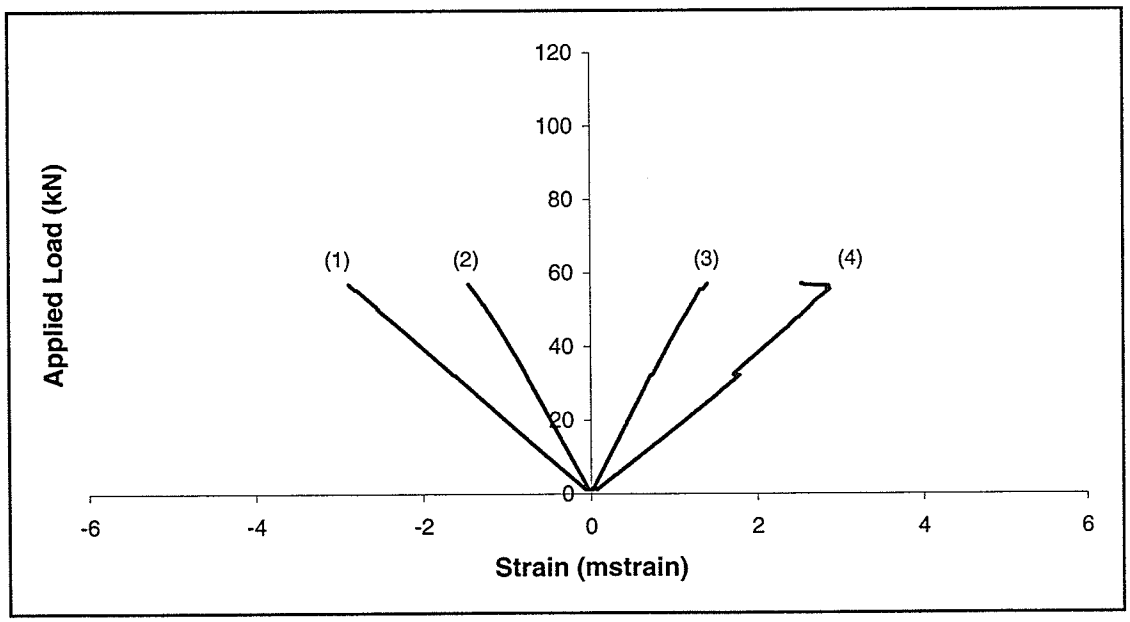

Figure A17(b) – Load-strain curves for Beam K2 (ρ_{GF} = 0.82%)

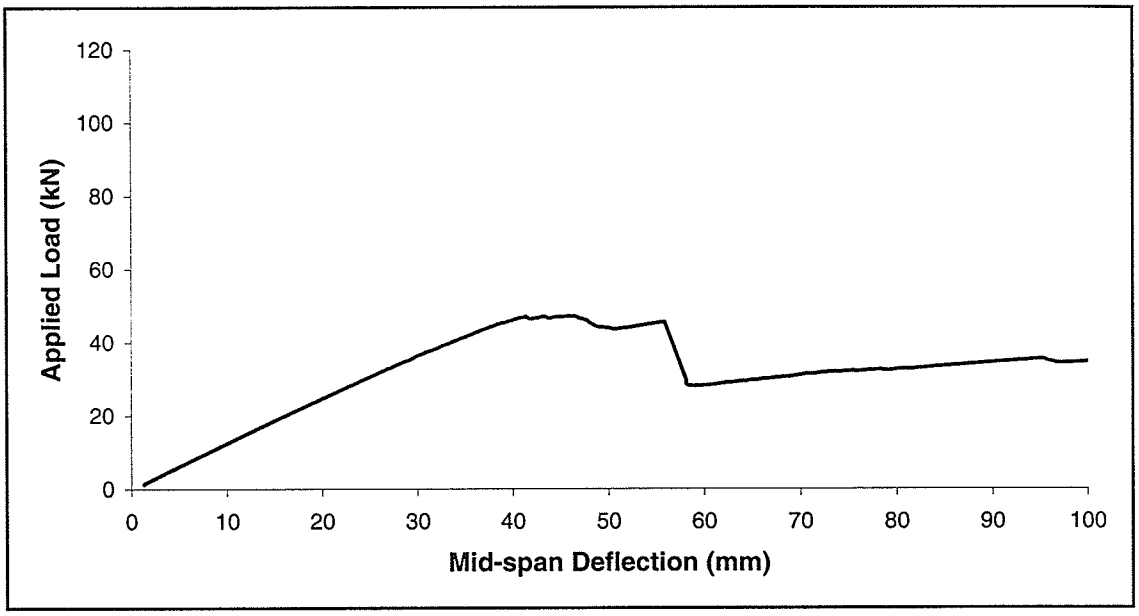

Figure A18(a) – Load-deflection curve for Beam L1 (ρ_{GF} = 0.41%)

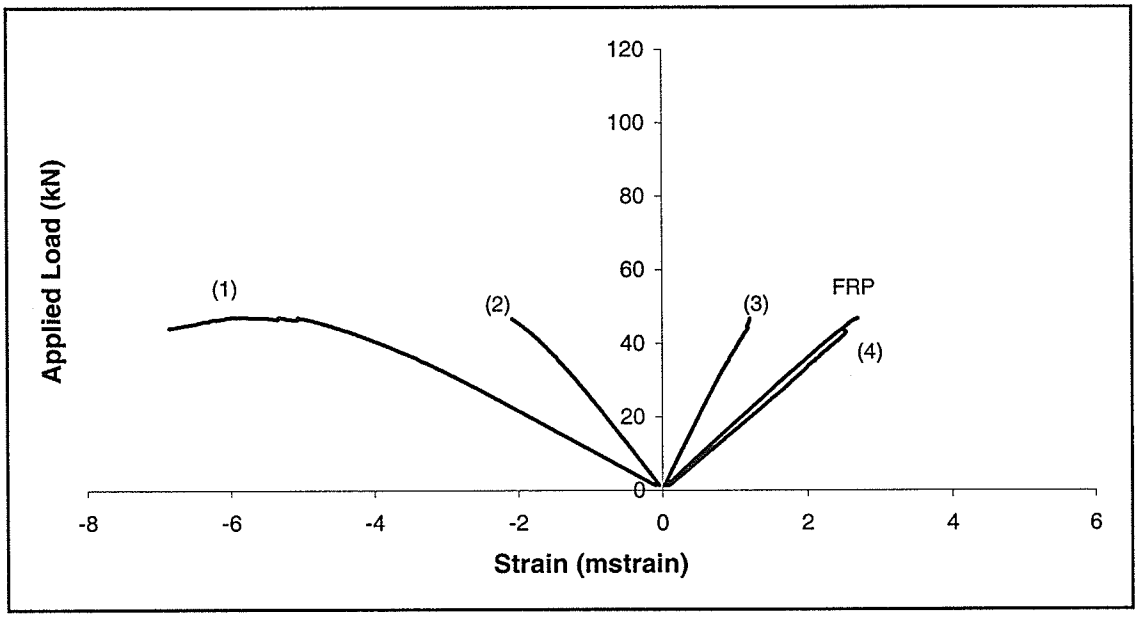

Figure A18(b) – Load-strain curves for Beam L1 (ρ_{GF} = 0.41%)

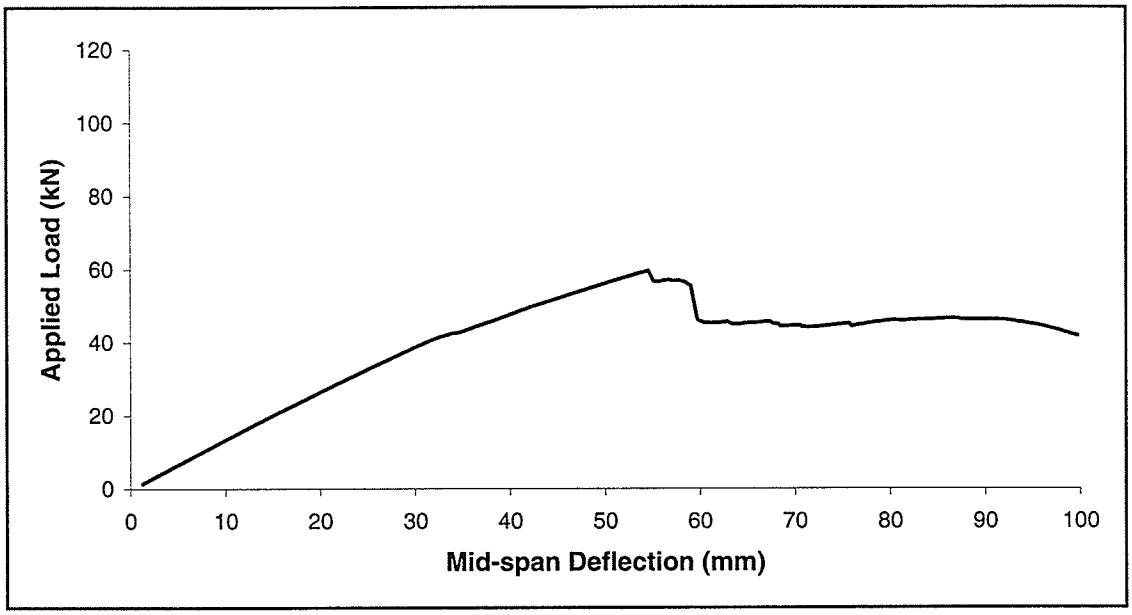

Figure A19(a) – Load-deflection curve for Beam L2 (ρ_{GF} = 0.82%)

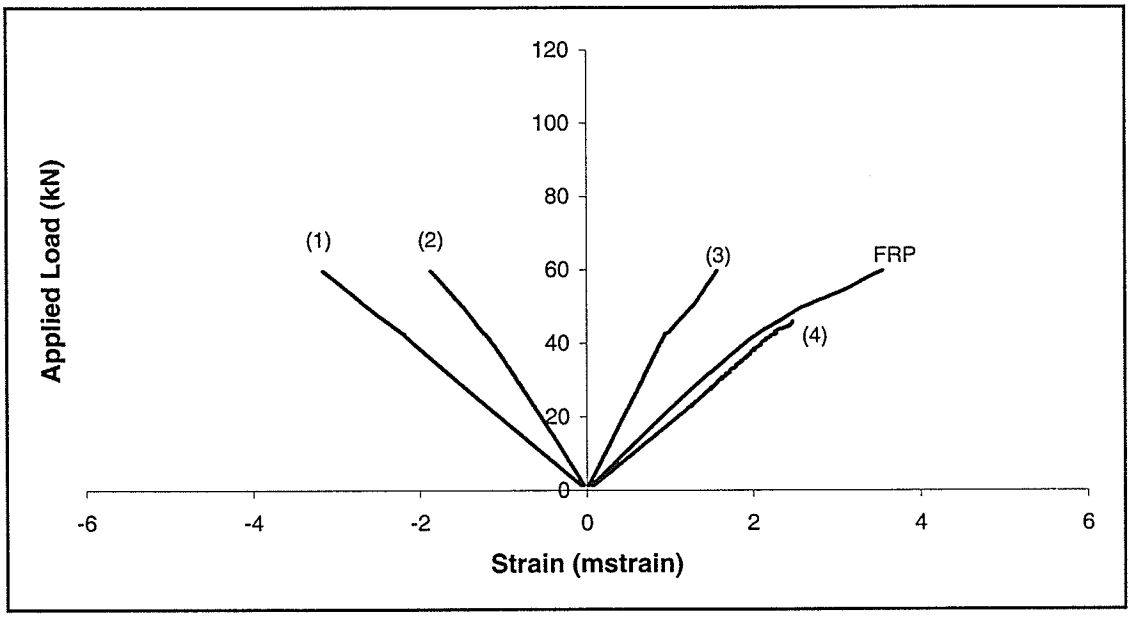

Figure A19(b) – Load-strain curves for Beam L2 (ρ_{GF} = 0.82%)

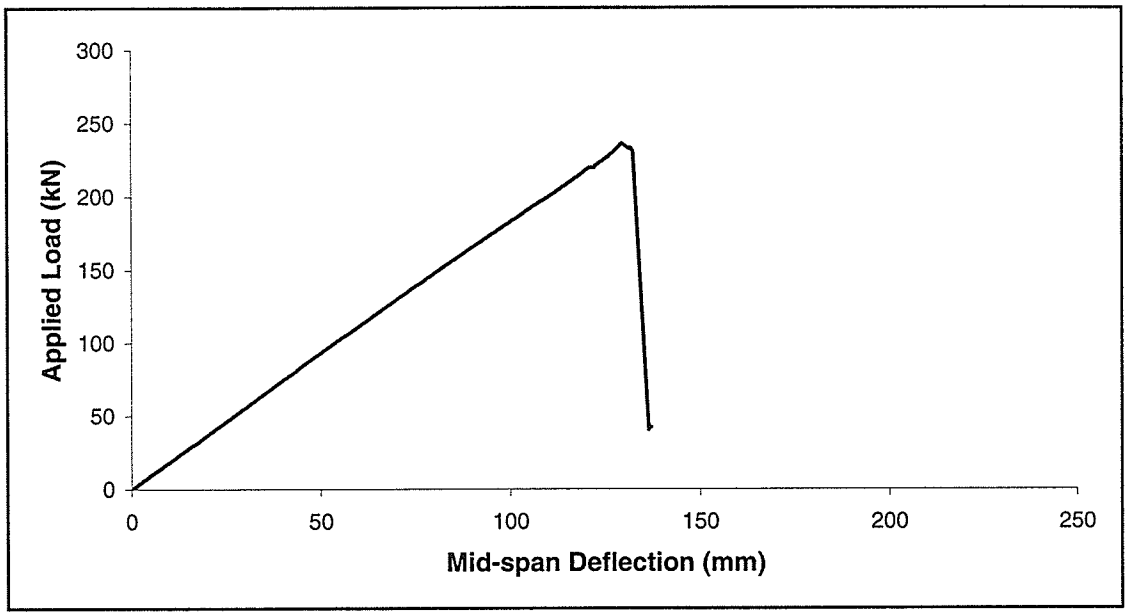

Figure A20(a) – Load-deflection curve for Beam FS-1 (ρ_{GF} = 0.42%)

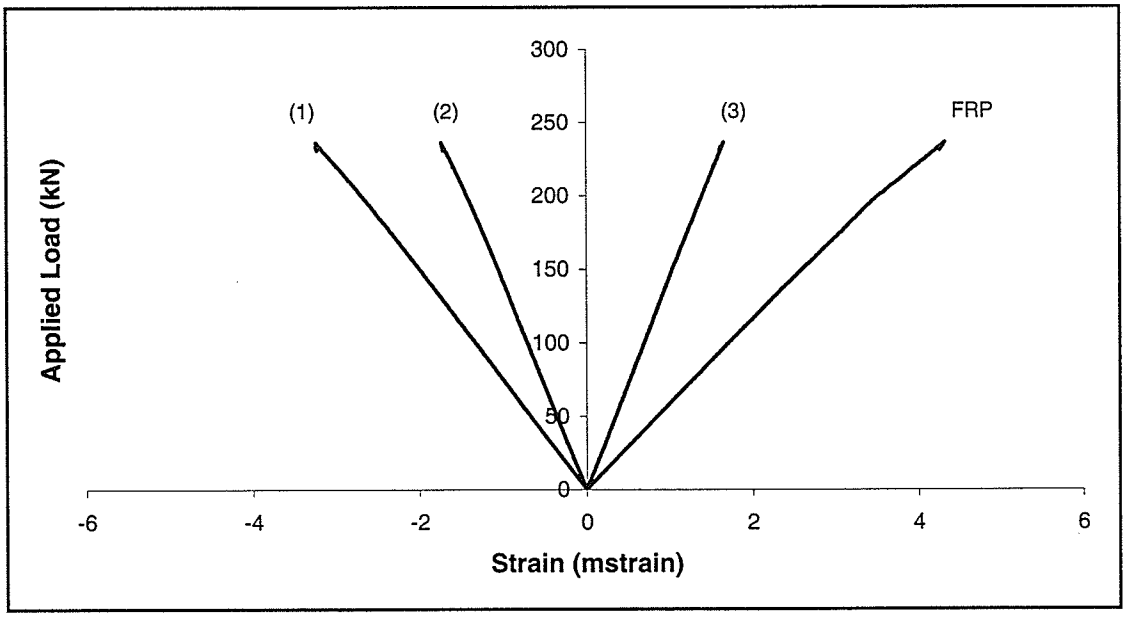

Figure A20(b) – Load-strain curves for Beam FS-1 (ρ_{GF} = 0.42%)

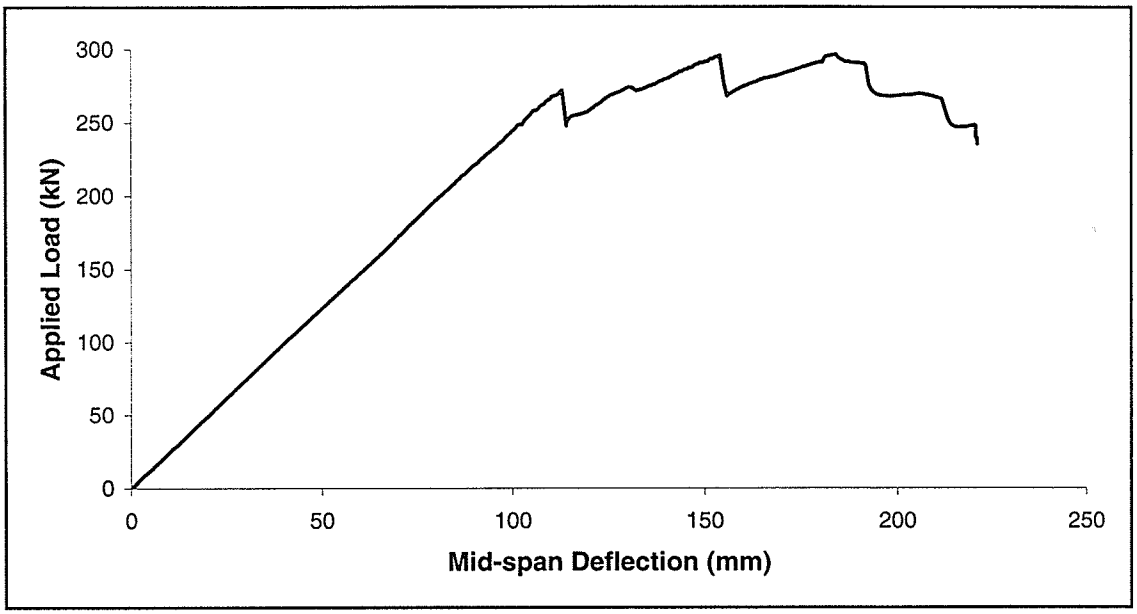

Figure A21(a) – Load-deflection curve for Beam FS-2 (ρ_{GF} = 0.26%)

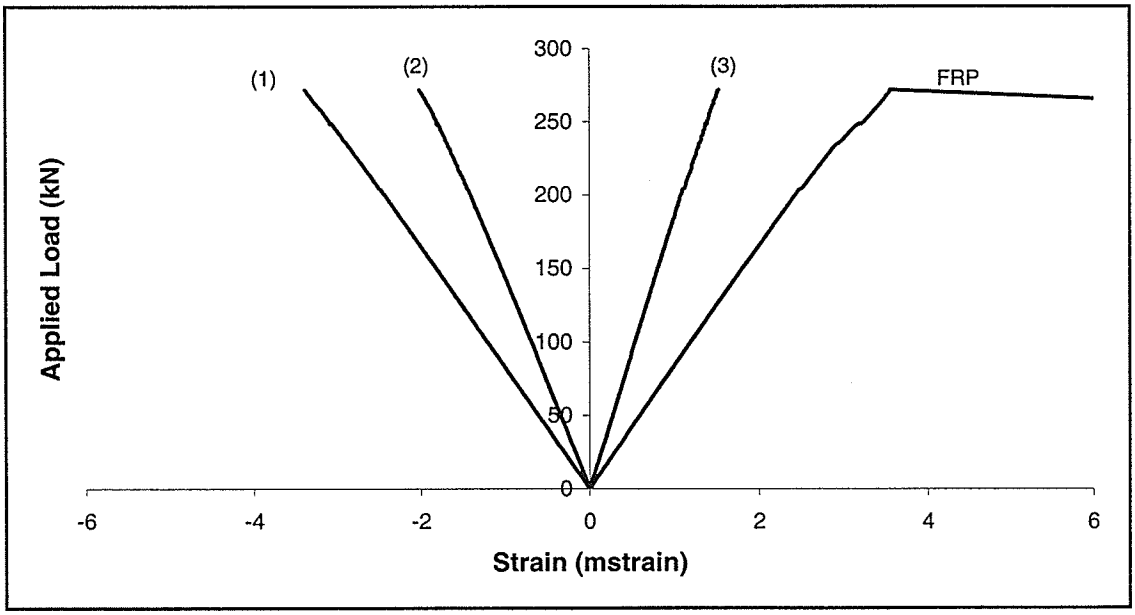

Figure A21(b) – Load-strain curves for Beam FS-2 (ρ_{GF} = 0.26%)

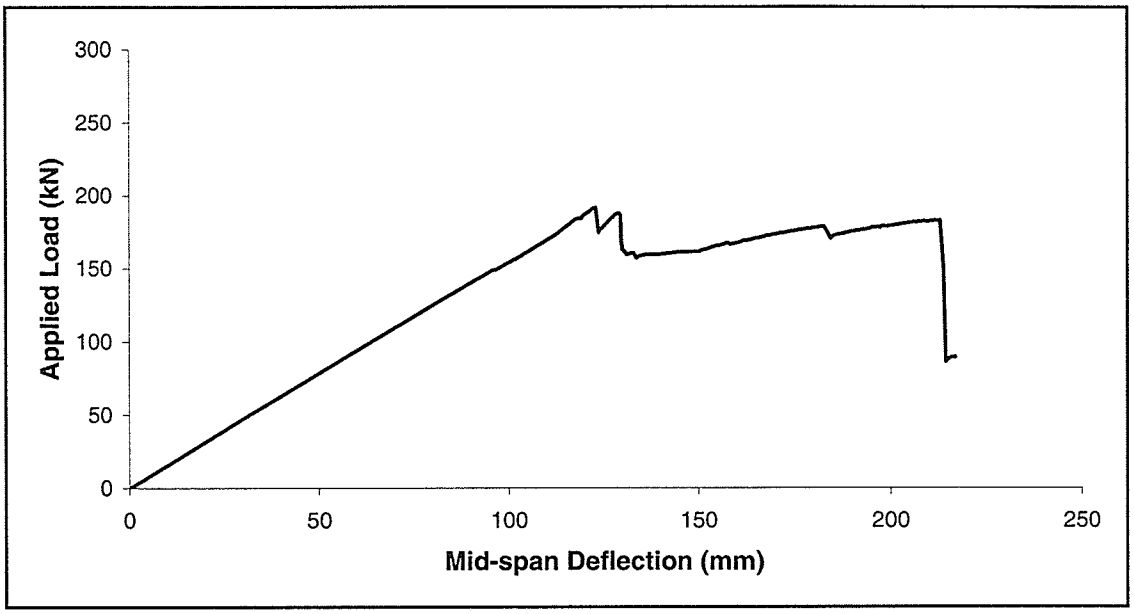

Figure A22(a) – Load-deflection curve for Beam FS-3 (ρ_{GF} = 0.42%)

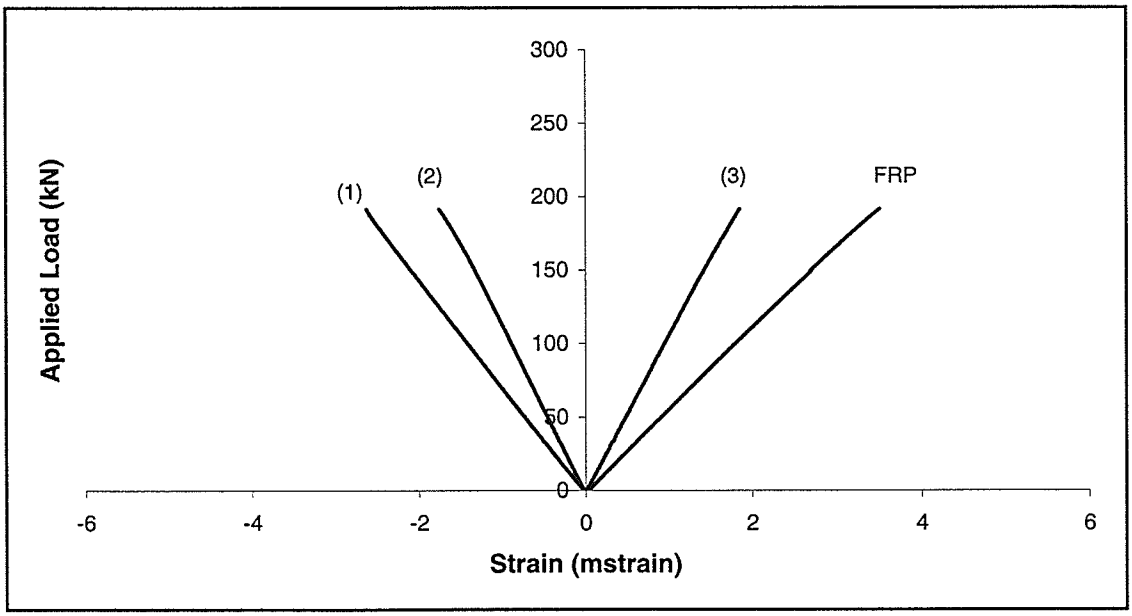

Figure A22(b) – Load-strain curves for Beam FS-3 (ρ_{GF} = 0.42%)

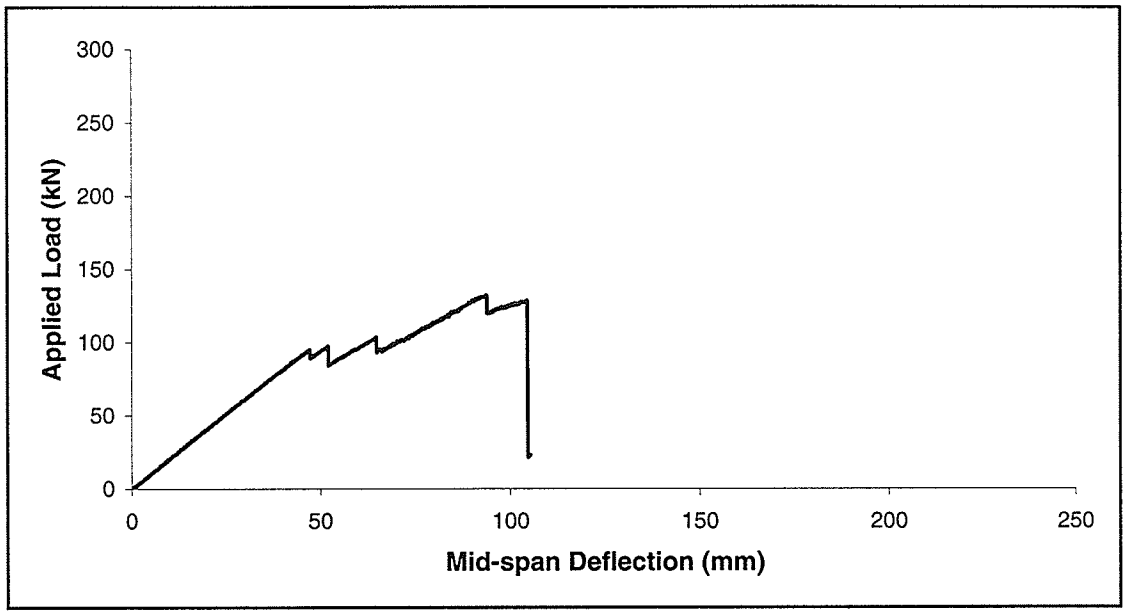

Figure A23(a) – Load-deflection curve for Beam FS-4 (plain timber)

Strains not measured for Beam FS-4.

APPENDIX B

SAMPLE CALCULATION OF BENDING STRENGTH

CALCULATION OF BENDING STRENGTH OF GFRP-REINFORCED BEAM

Beam G2, shown below, was reinforced with 0.82% GFRP (E_{GF} = 56 GPa) and tested to failure. The modulus of elasticity of the timber, E_w, was calculated to be 10,969 MPa. Use the proposed analytical model to predict the bending strength of Beam G2.

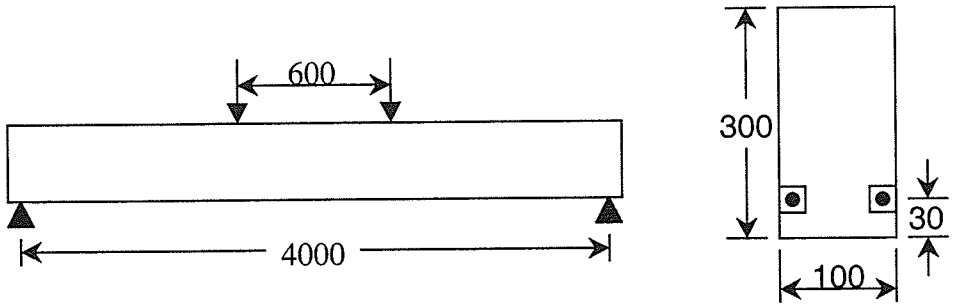

1. Determine percentile rank of E_w.

From Table 3.5.2 in Canadian Lumber Properties (Barrett and Lau, 1994), for MOE of 2x10 select structural Douglas Fir-Larch:

Mean = 12,914 MPa
5^{th} (P_5) = 8,860 MPa

Assuming MOE follows a normal distribution, calculate the standard deviation (SD)

P_5 = Mean-1.645(SD)

8860 = 12914-1.645(SD)

SD = 2464 MPa

Calculate standard normal random variable (z) of E_w

E_w = Mean + z(SD)

10969 = 12914+z(2464)

z = -0.79

From a table of standard normal curve areas

$$F(z) = F(-0.79) = \underline{0.215}$$

2. *Calculate f_{cu} and f_{tu}*

The strengths f_{cu} and f_{tu} are calculated by adjusting for size the ultimate compression strength, UCS, and ultimate tension strength, UTS, from the data published in Canadian Lumber Properties (Barrett and Lau, 1994). The data for UCS and UTS is tabulated as parameter estimates for four different statistical distributions. The 3-P Weibull distribution is used to calculate UCS and UTS.

From Tables I.25 (UCS) and I.13 (UTS) in Canadian Lumber Properties (Barrett and Lau, 1994) for 2x10 select structural Douglas Fir-Larch:

	Table I.25 (UCS)	Table I.13 (UTS)
Shape, k	2.79	1.86
Scale, m_1	24.13	20.62
Location, x_0	14.90	10.00

Use Equation (2.1) to calculate UCS and UTS for F(x) = 0.215

$$F(x) = 1 - \exp\left\{-\left(\frac{x - x_0}{m_1}\right)^k\right\}$$

UCS $$0.215 = 1 - \exp\left\{-\left(\frac{x - 14.90}{24.13}\right)^{2.79}\right\} \quad x = \underline{\text{UCS} = 29.40 \text{ MPa}}$$

UTS $$0.215 = 1 - \exp\left\{-\left(\frac{x - 10.00}{20.62}\right)^{1.86}\right\} \quad x = \underline{\text{UTS} = 19.63 \text{ MPa}}$$

Calculate the equivalent stressed length using Equation (5.3). The parameter k_1 is given in Table 5.1.

$$L_e = \frac{1 + \frac{a_1 k_1}{L}}{k_1 + 1} L$$

$$\text{Compression} \quad L_e = \frac{1+\frac{(600)(10.0)}{(4000)}}{(10.0)+1}(4000) \qquad \underline{L_{ec} = 909 \text{ mm}}$$

$$\text{Tension} \quad L_e = \frac{1+\frac{(600)(5.9)}{(4000)}}{(5.9)+1}(4000) \qquad \underline{L_{et} = 1094 \text{ mm}}$$

Calculate f_{cu} and f_{tu} using Equations (5.6) and (5.7). The parameters k_1 and k_2 are given in Table 5.1. The actual depth for 2x10 lumber is 235 mm. The characteristic lengths for UCS and UTS are given below.

L_{UCS} = 4267 mm (Table 3.5 in Canadian Lumber Properties)
L_{UTS} = 3683 mm (Table 3.7 in Canadian Lumber Properties)

$$f_{cu} = \text{UCS}\left(\frac{L_{\text{UCS}}}{L_{ec}}\right)^{1/k_1}\left(\frac{d_{\text{UCS}}}{d}\right)^{1/k_2}$$

$$f_{cu} = (29.40)\left(\frac{4267}{909}\right)^{1/10.0}\left(\frac{235}{300}\right)^{1/9.1} \qquad \underline{f_{cu} = 33.41 \text{ MPa}}$$

$$f_{tu} = \text{UTS}\left(\frac{L_{\text{UTS}}}{L_{et}}\right)^{1/k_1}\left(\frac{d_{\text{UTS}}}{d}\right)^{1/k_2}$$

$$f_{tu} = (19.63)\left(\frac{3683}{1094}\right)^{1/5.9}\left(\frac{235}{300}\right)^{1/4.4} \qquad \underline{f_{tu} = 22.81 \text{ MPa}}$$

3. *Calculate initial position of the neutral axis*

For the transformed section shown below, the position of the neutral axis can be calculated using simple mechanics. The modular ratio, n, is calculated

$$n = E_{GF}/E_w$$

$$n = 56000/10969 = 5.11$$

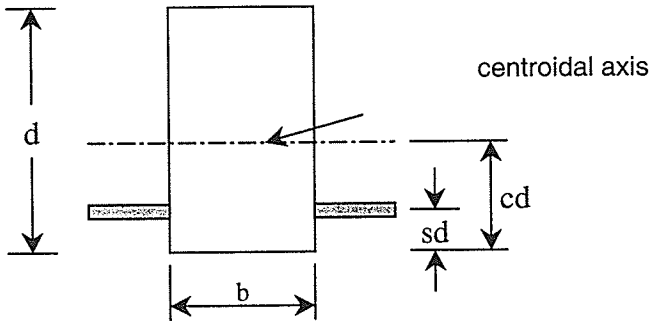

$$cd = \frac{bd\left(\frac{d}{2}\right) + (n-1)\rho_{GF} bd(sd)}{bd + (n-1)\rho_{GF} bd}$$

$$cd = \frac{(100)(300)\left(\frac{300}{2}\right) + (5.11-1)(0.0082)(100)(300)(30)}{(100)(300) + (5.11-1)(0.0082)(100)(300)}$$

$cd = 146.1$ mm

$c = 146.1/300 = \underline{0.4870}$

4. *Calculate f_m and ε_y*

The tensile strength in bending, f_m, is calculated using Equation (5.4).

$$f_m = \left(\frac{k_3 + 1}{c}\right)^{1/k_3} f_{tu}$$

$$f_m = \left(\frac{10.0+1}{0.4870}\right)^{1/10.0} 22.81 \qquad \underline{f_m = 31.15 \text{ MPa}}$$

The yield strain, ε_y, is calculated by

$$\varepsilon_y = f_{cu}/E_w$$

$\varepsilon_y = (33.41/10969)*1000$ $\qquad$ $\underline{\varepsilon_y = 3.05 \text{ mstrain}}$

5. *Perform strain compatibility analysis*

A strain compatibility analysis is performed by incrementing the extreme fibre tensile strain, ε_t. The strain at all levels in the cross-section can be calculated from ε_t and c. Failure occurs when

$$f_t = \alpha_m f_m$$

If the extreme fibre compression strain, ε_c, reaches ε_y before failure, the stress distribution in the section will be as shown below. The neutral axis will shift downwards, c will decrease, and f_m must be recalculated.

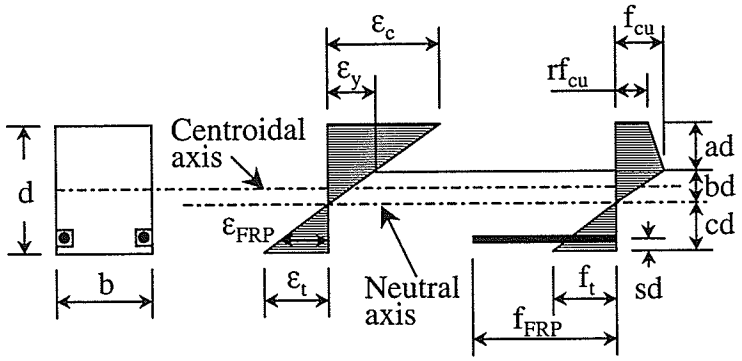

The parameters a, b, r in the stress distribution can be calculated from the strain distribution and the idealized stress-strain relationship shown below.

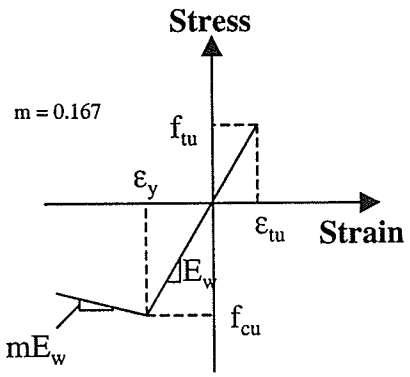

A spreadsheet was used to perform the strain compatibility analysis. A copy of the calculations for Beam G2 is included on the following page. The program calculates bending moment and curvature for each strain increment. The modulus of rupture (MOR) can be calculated

$$MOR = \frac{M_F}{S_g} = \frac{6M_F}{bd^2}$$

$$MOR = \frac{6(64.35(10)^6)}{(100)(300)^2}$$

$\underline{MOR = 42.9 \text{ MPa}}$

Beam G2 - ρ_{QF} = 0.82%

b	100 mm	f_{cu}	33.41 MPa	e_y	3.046
d	300 mm	f_{tu}	22.81 MPa		
s	0.100	E_w	10969 MPa	m	0.166667
ρ_{FRP}	0.0082	E_{FRP}	56000 MPa	k_3	10.0
y_bar	146.09	n	5.105		
c_0	0.48697	α	1.300		

c	f_m	ε_t	f_t	αf_m	ε_c	b	a	r	f_{c_top}	ε_{FRP}	T_w	T_{FRP}	C_{w1}	C_{w2}	C_{w3}	T_{tot}	C_{tot}	M_{wt}	M_{FRP}	M_{wc}	M_{tot}	ϕ
	(MPa)	(mstrain)	(MPa)	(MPa)	(mstrain)				(MPa)	(mstrain)	(kN)	(kN)	(kN)	(kN)	(kN)	(kN)	(kN)	(kN-m)	(kN-m)	(kN-m)	(kN-m)	
0.4870	31.15	0.10	1.10	40.50	0.10535	0.5130	0.0000	1.000	1.16	0.07946	7.80	1.09	8.89	0.00	0.00	8.89	8.89	0.76	0.13	0.91	1.80	6.845E-07
0.4870	31.15	0.50	5.48	40.50	0.52675	0.5130	0.0000	1.000	5.78	0.39732	38.99	5.47	44.46	0.00	0.00	44.46	44.46	3.80	0.64	4.56	9.00	3.423E-06
0.4870	31.15	1.00	10.97	40.50	1.05350	0.5130	0.0000	1.000	11.56	0.79465	77.98	10.95	88.93	0.00	0.00	88.93	88.93	7.59	1.27	9.12	17.99	6.845E-06
0.4870	31.15	1.50	16.45	40.50	1.58025	0.5130	0.0000	1.000	17.33	1.19197	116.97	16.42	133.39	0.00	0.00	133.39	133.39	11.39	1.91	13.69	26.99	1.027E-05
0.4870	31.15	2.00	21.94	40.50	2.10700	0.5130	0.0000	1.000	23.11	1.58930	155.96	21.89	177.85	0.00	0.00	177.85	177.85	15.19	2.54	18.25	35.98	1.369E-05
0.4870	31.15	2.50	27.42	40.50	2.63375	0.5130	0.0000	1.000	28.89	1.98662	194.95	27.37	222.32	0.00	0.00	222.32	222.32	18.99	3.18	22.81	44.98	1.711E-05
0.4870	31.15	2.90	31.81	40.50	3.05515	0.5115	0.0016	0.999	33.39	2.30448	226.14	31.75	256.32	1.56	0.00	257.89	257.89	22.02	3.69	26.46	52.17	1.985E-05
0.4868	31.16	3.000	32.91	40.50	3.16270	0.4942	0.0190	0.994	33.20	2.38373	233.85	32.84	247.69	18.88	0.06	266.69	266.63	22.77	3.81	27.35	53.92	2.054E-05
0.4862	31.16	3.100	34.00	40.51	3.27598	0.4777	0.0361	0.987	32.99	2.46240	241.35	33.92	239.40	35.72	0.23	275.27	275.35	23.47	3.93	28.22	55.62	2.125E-05
0.4854	31.16	3.200	35.10	40.51	3.39250	0.4620	0.0526	0.981	32.78	2.54075	248.71	35.00	231.54	51.70	0.50	283.71	283.74	24.15	4.05	29.04	57.23	2.198E-05
0.4843	31.17	3.300	36.20	40.52	3.51396	0.4470	0.0687	0.974	32.55	2.61860	255.89	36.07	224.02	67.09	0.88	291.97	291.99	24.79	4.16	29.84	58.78	2.271E-05
0.4829	31.18	3.400	37.29	40.53	3.64080	0.4326	0.0845	0.967	32.32	2.69592	262.87	37.14	216.80	81.94	1.38	300.01	300.11	25.39	4.27	30.62	60.27	2.347E-05
0.4814	31.19	3.500	38.39	40.55	3.77046	0.4189	0.0997	0.960	32.09	2.77295	269.74	38.20	209.95	95.93	1.98	307.94	307.86	25.97	4.37	31.35	61.69	2.423E-05
0.4795	31.20	3.600	39.49	40.56	3.90782	0.4057	0.1148	0.953	31.83	2.84922	276.33	39.25	203.31	109.65	2.71	315.58	315.67	26.50	4.47	32.09	63.06	2.503E-05
0.4775	31.22	3.699	40.57	40.58	4.04760	0.3932	0.1293	0.945	31.58	2.92434	282.72	40.29	197.05	122.51	3.55	323.01	323.10	27.00	4.56	32.79	64.35	2.582E-05

APPENDIX C

CALIBRATION OF ANALYTICAL MODELS

Plain Timber

Beam ID	MOE (MPa)	MOR_{meas} (kN-m)	$k_3 = 9$		$k_3 = 10$		$k_3 = 11$	
			MOR_{calc} (kN-m)	meas / calc	MOR_{calc} (kN-m)	meas / calc	MOR_{calc} (kN-m)	meas / calc
F1	6999	18.75	18.71	1.00	18.27	1.03	17.90	1.05
J1	7602	19.83	19.79	1.00	19.33	1.03	18.94	1.05
B1	8568	21.58	22.12	0.98	21.60	1.00	21.17	1.02
H1	9654	24.98	25.78	0.97	25.17	0.99	24.67	1.01
C1	10197	37.00	28.05	1.32	27.39	1.35	26.85	1.38
A1	10257	21.24	28.37	0.75	27.71	0.77	27.15	0.78
G1	14662	43.68	55.93	0.78	54.83	0.80	53.87	0.81
AVG				0.97		0.99		1.01
SD				0.19		0.19		0.20
COV (= SD/AVG)				0.19		0.19		0.19

$\rho = 0.27\%$

Beam ID	MOE (MPa)	MOR_{meas} (kN-m)	$\alpha = 1.25$		$\alpha = 1.23$		$\alpha = 1.20$	
			MOR_{calc} (kN-m)	meas / calc	MOR_{calc} (kN-m)	meas / calc	MOR_{calc} (kN-m)	meas / calc
F2	6039	23.00	22.69	1.01	22.37	1.03	21.86	1.05
D2	11189	36.04	40.81	0.88	40.27	0.89	39.45	0.91
D1	12491	52.81	49.46	1.07	48.87	1.08	47.95	1.10
AVG				0.99		1.00		1.02
SD				0.09		0.10		0.10
COV (= SD/AVG)				0.10		0.10		0.10

$\rho = 0.41\%$

Beam ID	MOE (MPa)	MOR_{meas} (kN-m)	$\alpha = 1.30$		$\alpha = 1.25$		$\alpha = 1.20$	
			MOR_{calc} (kN-m)	meas / calc	MOR_{calc} (kN-m)	meas / calc	MOR_{calc} (kN-m)	meas / calc
L1	7274	27.08	26.02	1.04	25.12	1.08	24.21	1.12
H2	9327	32.01	32.63	0.98	31.55	1.01	30.40	1.05
I1	14724	61.25	68.29	0.90	66.78	0.92	65.13	0.94
AVG				0.97		1.00		1.04
SD				0.07		0.08		0.09
COV (= SD/AVG)				0.07		0.08		0.09

ρ = 0.82%

Beam ID	MOE (MPa)	MOR_{meas} (kN-m)	α = 1.35		α = 1.34		α = 1.25	
			MOR_{calc} (kN-m)	meas / calc	MOR_{calc} (kN-m)	meas / calc	MOR_{calc} (kN-m)	meas / calc
L2	7598	34.11	29.37	1.16	29.19	1.17	27.57	1.24
K2	7770	24.08	29.63	0.81	29.45	0.82	27.81	0.87
A2	10855	43.29	43.37	1.00	43.15	1.00	40.94	1.06
G2	10969	44.19	44.09	1.00	43.85	1.01	41.63	1.06
I2	13140	58.70	59.13	0.99	58.88	1.00	56.37	1.04
AVG				0.99		1.00		1.05
SD				0.12		0.12		0.13
COV (= SD/AVG)				0.12		0.12		0.12

All Reinforced

Beam ID	MOE (MPa)	MOR_{meas} (kN-m)	α = 1.35		α = 1.30		α = 1.25	
			MOR_{calc} (kN-m)	meas / calc	MOR_{calc} (kN-m)	meas / calc	$MOR_{F\ calc}$ (kN-m)	meas / calc
F2	6039	23.00	24.23	0.95	23.49	0.98	22.69	1.01
D2	11189	36.04	43.31	0.83	42.10	0.86	40.81	0.88
D1	12491	52.81	52.19	1.01	50.87	1.04	49.46	1.07
L1	7274	27.08	26.85	1.01	26.02	1.04	25.12	1.08
H2	9327	32.01	33.65	0.95	32.63	0.98	31.55	1.01
I1	14724	61.25	69.65	0.88	68.29	0.90	66.78	0.92
L2	7598	34.11	29.37	1.16	28.49	1.20	27.57	1.24
K2	7770	24.08	29.63	0.81	28.74	0.84	27.81	0.87
A2	10855	43.29	43.37	1.00	42.19	1.03	40.94	1.06
G2	10969	44.19	44.09	1.00	42.90	1.03	41.63	1.06
I2	13140	58.70	59.13	0.99	57.82	1.02	56.37	1.04
AVG				0.96		0.99		1.02
SD				0.10		0.10		0.10
COV (= SD/AVG)				0.10		0.10		0.10